

AUTOMATED GEOLOCATION IMPROVEMENT FOR NANOSATELLITE
MISSIONS BASED ON COASTLINE DETECTION FOR NEAR INFRARED
SPECTROMETERS

GUY BENARI

A DISSERTATION SUBMITTED TO
THE FACULTY OF GRADUATE STUDIES
IN PARTIAL FULFILLMENT OF THE REQUIREMENTS
FOR THE DEGREE OF
DOCTOR OF PHILOSOPHY

GRADUATE PROGRAM IN EARTH AND SPACE SCIENCE

YORK UNIVERSITY,

TORONTO, ONTARIO

JULY 2017

© GUY BENARI, 2017

Abstract

Geolocation, defined as the determination of the location on the ground from which a remote sensing observation is made, is a critical task in delivering accurate and reliable scientific data from an Earth observation (EO) spaceborne measurement system. Geolocation accuracy is a mission requirement, whose validation in EO missions with low resolution spectrometers is a challenging problem. While various techniques are proposed for large space missions, limited techniques are available for CubeSat-class, resource constrained, low resolution spectrometer payloads. In this dissertation, a novel approach for automated geolocation accuracy assessment using coastline detection was developed and implemented for CubeSat-class nanosatellite missions with low-resolution single-pixel spectrometers in nadir viewing configurations. The algorithm was demonstrated using Argus 1000 near-infrared (NIR) spectrometer data aboard the CanX-2 nanosatellite in order to verify the mission requirements of 1° (1σ) pointing knowledge uncertainty. The same algorithm was also applied to airborne data using the Ocean Optics FLAME-NIR spectrometer for validation purposes. Radiometric calibration was also performed on both instruments for use in field campaigns.

From the spaceborne data analysis, 270 spectrometer data sets were analyzed, from which 55 coastlines were detected. The mean angular error in the data sets was 0.44° and the standard deviation was 0.57° , which was consistent with the CanX-2 mission requirements. The airborne data analysis yielded similar results using the same coastline detection algorithm as the spaceborne data analysis. A total of 7 data sets were acquired over two

days at two data collection sites. 36 coastline crossings were detected and a mean angular error of 9.7° was observed, with a standard deviation of 6.8° . Compared to the spaceborne data, higher error was observed due to the lower speed and altitude of the UAV compared to the satellite.

Acknowledgements

I would like to acknowledge all those who have supported me throughout the development of this dissertation. First, I would like to thank my supervisor, Dr. Regina Lee, for all giving me the opportunity to pursue this research and for all her guidance throughout this process. I am grateful to Ms. Catherine Tsouvaltsidis for all her invaluable help and support, including Argus calibration and UAV mission planning and assembly. I would also like to thank the Argus science team for their feedback on the automated geolocation work and Thoth Technology for providing me with an Argus spectrometer, ArduCopter, and calibrated lamp for the validation campaign and instrument calibration, along with all the necessary Argus documentation for completing this work. I would like to thank the CanX-2 operations team at the University of Toronto Space Flight Laboratory for all their help in coordinating and executing Argus mission operations. I would also like to express my gratitude to Dr. Costas Armenakis and his research group, in particular Ms. Sowmya Natesan, for all their help with the FLAME-NIR validation campaign and camera image processing. I would like to thank the Natural Science and Engineering Research Council for their financial support. I would like to thank my friends and lab colleagues, both past and present, for all their support throughout the years. Lastly, this dissertation would not have been possible without the continued support of my family, who encouraged me throughout this entire process.

Table of Contents

Abstract	ii
Acknowledgements	iv
Table of Contents	v
List of Tables	viii
List of Figures	ix
List of Abbreviations and Symbols.....	xv
1 Introduction.....	1
1.1 Nanosatellite-Based Earth Observation Missions	1
1.2 Geolocation in Earth Observation Missions.....	6
1.3 Automated Geolocation.....	7
1.4 Unmanned Aerial Vehicle Based Geolocation Validation.....	8
1.5 Argus 1000 and FLAME-NIR Spectrometers.....	9
1.6 Dissertation Contributions.....	10
1.7 Dissertation Outline.....	10
2 Literature Review.....	13

2.1	Automation of Satellite Operations and Data Analysis	13
2.2	Coastline Detection for Geolocation Accuracy Assessment.....	17
2.3	Airborne Validation Campaigns.....	27
3	Automated Generation and Error Analysis of Spaceborne Spectrometer Data Products	32
3.1	Implementation of the Automated Geolocation Algorithm	34
3.2	Argus Geolocation Error Analysis	39
3.3	Validation of Data Integrity	40
4	Validation of Geolocation Accuracy Using a Coastline Detection Algorithm.....	54
4.1	Implementation of Automated Coastline Detection Algorithm	54
4.1.1	Coastline Crossing Search Algorithm.....	55
4.1.2	Detection of Coastline Crossings in NIR Spectrometer Data.....	66
4.2	Analysis of Coastline Detection Algorithm Results	68
5	Radiometric Calibration of Near Infrared Spectrometers.....	79
5.1	Laboratory Radiometric Calibration Setup	80
5.2	Radiometric Calibration Model.....	83
5.3	Argus 1000 Unit 8 Radiometric Calibration Results	86
5.4	FLAME-NIR Radiometric Calibration Results.....	115
5.5	Radiometric Calibration Conclusion.....	125

6	Validation of the Coastline Detection Algorithm Using a UAV Campaign.....	126
6.1.1	Airborne Validation Campaign Platform.....	126
6.1.2	Airborne Validation Campaign Procedure.....	133
6.1.3	Airborne Validation Campaign Results	137
7	Conclusion and Recommendations for Future Work.....	149
8	References.....	154
Appendix A	Argus Timing Duration Difference Experiment Data Tables	167
Appendix B	Argus Timing Duration Difference Least Squares Fitting Table	175

List of Tables

Table 2-1 Summary of coastline detection methods used for geolocation validation	25
Table 3-1 Comparison of actual duration and requested duration of 26 Argus data sets .	42
Table 4-1 Coastline detection results summary table	70
Table 5-1 Argus 100 and FLAME-NIR specifications [60], [63]	80
Table 5-2 Calibration data settings and total packet numbers	96
Table 6-1 Airborne validation campaign data set properties	137
Table 6-2 Coastline detection results for FLAME-NIR airborne campaign with $1 \times 10^{-5} \text{ Wm}^{-2}$ irradiance detection threshold.....	141
Table 7-1 Summary of coastline detection results for spaceborne and airborne data.....	150
A-1 Size and duration of flight spare Argus data sets at varying exposure time settings for a scan count setting of 1	168
A-2 Comparison of the actual time per packet and the exposure time setting of flight spare Argus data sets for a scan count setting of 1.....	170
A-3 Size and duration of flight spare Argus data sets at varying exposure time settings for a scan count setting of 2.....	172
A-4 Comparison of the actual time per packet and the exposure time setting of flight spare Argus data sets for a scan count setting of 2.....	174
B-1 Least squares fitting of scaling factors to Argus data set exposure time and duration calculations	176

List of Figures

Figure 2-1 Cubic polynomial fit for a series of four consecutive radiance measurements for coastline detection of ERBE instruments [29].....	18
Figure 3-1 Block diagram of semi-automated geolocation algorithm of Argus data sets (adapted from [28]).....	33
Figure 3-2 Levels of processing of automated geolocation.....	35
Figure 3-3 RADARSAT-1 Data Products (adapted from [55]).....	36
Figure 3-4 Block diagram of automated acquisition and processing of Level 0 parameters for spaceborne Argus data sets	37
Figure 3-5 Number of bytes acquired and duration of flight spare Argus data sets at varying exposure time settings for a scan count setting of 1	43
Figure 3-6 Scatter plot of ratio of the average time per packet to exposure time vs exposure time setting for a scan count setting of 1	45
Figure 3-7 Number of bytes acquired and duration of flight spare Argus data sets at varying exposure time settings for a scan count setting of 2	46
Figure 3-8 Scatter plot of measured time per packet vs exposure time setting for a scan count setting of 2.....	47
Figure 3-9 Least squares residuals of scaling factors to Argus data set exposure time and duration calculations: case 1 on top left, case 2 on top right, case 3 on middle left, case 4 on middle right, case 5 on lower left, and case 6 on lower right	49

Figure 3-10 Norm of least squares residuals of scaling factors to Argus data set exposure time and duration calculations for six cases	50
Figure 4-1 Coastline crossing search algorithm flow charts with steps 1-3 (top) connected to step 4 (bottom) by connector 1	57
Figure 4-2 Visualization of the search space reduction concept for automated coastline identification, with several GSHHG polygon segments (blue), Argus boresight locations (red), and rectangular enclosing segments (black)	59
Figure 4-3 Classification concept of coastline crossings based on spectrometer boresight locations (red) and terrain changes, with GSHHG coastlines (blue) shown along with spectral start locations (circles) and spectral end locations (stars)	61
Figure 4-4 Visualization of minor coastline crossing search for Argus data set acquired over Vancouver area. Argus boresight packet locations (red), GSHHG segments (blue), and packet search regions (black) as shown.	63
Figure 4-5 Illustration of the final iterative process for determining coastline locations with GSHHG coastline (blue), Argus boresight points (red), and calculated coastline crossings (green)	65
Figure 4-6 Angular error vs coastline crossing angle for Argus 1000 coastline detection results	72
Figure 4-7 Angular error from expected location to detected location of coastlines over mission time with 1° (1σ) attitude knowledge requirement shown	73

Figure 4-8 Illustrations of data sets containing coastline detections organized under mission defined regions of interest, with sample result shown (top left) for highlighted region (top right).....	75
Figure 4-9 Number of coastline detections found vs cubic polynomial irradiance threshold value.....	77
Figure 5-1 Laboratory setup of spectrometer radiometric calibration	81
Figure 5-2 Argus 1000 radiometric calibration setup, consisting of spectrometer mounted on rotation stage (top), gold plated OAP (middle), and calibrated lamp (bottom).....	82
Figure 5-3 Irradiance vs wavelength of 1000W ORIEL calibrated lamp model SN7-1993 (adapted from [65]).....	88
Figure 5-4 Reflectance vs wavelength of gold plated off-axis parabolic mirror (adapted from [67]).....	89
Figure 5-5 Expected number of photons received by the detector at each wavelength at an exposure time of 256 ms.....	90
Figure 5-6 Diffraction grating efficiency vs wavelength (adapted from [68]).....	91
Figure 5-7 Lens transmittance vs wavelength (adapted from [68]).....	92
Figure 5-8 Detector quantum efficiency vs wavelength (adapted from [69])	93
Figure 5-9 Lamp irradiance received by spectrometer detector vs wavelength	94
Figure 5-10 Background detector counts vs wavelength at four exposure time settings for Argus 1000 radiometric calibration	95
Figure 5-11 Detector counts vs wavelength for $\Delta t = 0.064$ s, $C = 10$ pF, $NS = 1$, and $SPP = 1$ for Argus 1000 with each packet identified by colour	97

Figure 5-12 Detector counts vs wavelength for $\Delta t = 0.002$ s, $C = 0.4$ pF, $NS = 1$, and $SPP = 1$ for Argus 1000 with each packet identified by colour	98
Figure 5-13 Detector counts vs packet number at pixel 125 (1241.2374 nm) for Argus 1000	100
Figure 5-14 Spectral exposure per detector count (JPC) vs wavelength for $\Delta t = 0.064$ s, $C = 10$ pF, $NS = 1$, and $SPP = 1$ for Argus 1000.....	101
Figure 5-15 Spectral exposure per detector count (JPC) vs wavelength for $\Delta t = 0.002$ s, $C = 0.4$ pF, $NS = 1$, and $SPP = 1$ for Argus 1000.....	103
Figure 5-16 Spectral exposure per detector count vs wavelength at $C = 10$ pF for Argus 1000. (Top left: $t = 0.016$ s, Top right: $t = 0.032$ s, Bottom: $t = 0.064$ s).....	104
Figure 5-17 Spectral exposure per detector count vs wavelength at $C = 0.4$ pF for Argus 1000. (Top: $t = 0.001$ s, Bottom: $t = 0.002$ s)	106
Figure 5-18 Spectral exposure per detector count vs wavelength of all data sets at 10 pF for Argus 1000.....	107
Figure 5-19 Spectral exposure per detector count vs wavelength of all data sets at 0.4 pF for Argus 1000	109
Figure 5-20 JPC curve and fitted polynomial function vs wavelength for 1 scan and 1 sample per pixel for Argus 1000. (Top: $t = 0.064$ s and $C = 10$ pF, Bottom: $t = 0.002$ s and $C = 0.4$ pF)	111
Figure 5-21 Fitted polynomial functions vs wavelength for Argus 1000. (Left: $C = 10$ pF, Right: $C = 0.4$ pF).....	112

Figure 5-22 Fractional uncertainty of spectral exposure per detector count vs wavelength for Argus 1000 (Top: C = 10 pF, Bottom: C = 0.4 pF)	113
Figure 5-23 JPC conversion functions for Argus 1000 Unit 8 spectrometer at capacitor settings of 10 pF (top) and 0.4 pF (bottom)	115
Figure 5-24 Laboratory background counts vs wavelength at three exposure time settings for FLAME-NIR radiometric calibration.....	117
Figure 5-25 Detector counts vs measurement number for FLAME-NIR at pixel 125 (1641.592 nm).....	118
Figure 5-26 Spectral exposure per counts (JPC) vs wavelength for FLAME-NIR with $\Delta t = 0.001$ s and P = 250 W	119
Figure 5-27 Spectral exposure per count vs wavelength for FLAME-NIR. (Top left: t = 0.001 s, Top right: t = 0.002 s, Bottom: t = 0.003 s).....	120
Figure 5-28 Spectral exposure per count vs wavelength for FLAME-NIR for P = 250 W	121
Figure 5-29 Spectral exposure per count vs wavelength for FLAME-NIR for all data sets	122
Figure 5-30 Fractional uncertainty of spectral exposure per detector count vs wavelength for FLAME-NIR	123
Figure 5-31 JPC conversion functions for FLAME-NIR spectrometer	124
Figure 6-1 UAV system consisting of DJI Flamewheel F550 with mounted FLAME-NIR spectrometer and Raspberry Pi board and camera module payload	127

Figure 6-2 Side view of FLAME-NIR spectrometer and Raspberry Pi camera payload geometry	129
Figure 6-3 Top view of FLAME-NIR spectrometer (orange) and Raspberry Pi camera payload geometry (not all pixels are shown)	131
Figure 6-4 Airborne validation campaign data collection sites: Chaffeys Locks, ON (Top, [70]) and Little Skunk Lake, ON (bottom, [71])	134
Figure 6-5 Raspberry Pi camera image containing four stadia rods acquired over Chaffeys Locks, ON.....	136
Figure 6-6 Orthomosaic composed of Raspberry Pi images taken over Chaffeys Locks, ON (top) and Little Skunk Lake, ON (bottom)	138
Figure 6-7 Orthomosaic for data sets acquired over Chaffeys Locks, ON, with spectrometer field of view ellipses (red) and corresponding Raspberry Pi image boundaries (blue) overlaid for data set 1	139
Figure 6-8 Angular error vs coastline crossing angle for FLAME-NIR airborne campaign coastline detection results	145
Figure 6-9 Angular error from expected coordinates to detected coordinates of coastlines versus packet number for Chaffeys Locks and Little Skunk Lake campaigns	146
Figure 6-10 Orthomosaics of Chaffeys Locks (top) and Little Skunk Lake (bottom) with coastline polygons (blue), expected coastline locations (stars) and detected coastline locations (crosses) overlaid for each data set.....	147

List of Abbreviations and Symbols

List of

Abbreviations

ACE	Airborne Chemistry Experiment
ADCS	Attitude Determination and Control System
AIRS	Atmospheric Infrared Sounder
ALADIN	Atmospheric Laser Doppler Instrument
AMSR-E	Advanced Microwave Scanning Radiometer for Earth Observing System
APMIR	Airborne Polarimetric Microwave Imaging Radiometer
ARM	Advanced RISC Machine
ASPEN	Automated Scheduling and Planning ENvironment
CALIPSO	Cloud-Aerosol Lidar Infrared Pathfinder Satellite Observations
CanX-2	Canadian Advanced Nanospace eXperiment-2
CCD	Charge-coupled Device
CERES	Clouds and the Earth's Radiant Energy System
COTS	Commercial Off-the-Shelf
DAISEX'99	Digital Airborne Imaging Spectrometer Experiment
EO	Earth Observation
EOP	Earth Orientation Parameter
ERBE	Earth Radiation Budget Experiment

ERBS	Earth Radiation Budget Satellite
ESA	European Space Agency
FOV	Field of View
GCP	Ground Control Point
GNC	Guidance, Navigation, and Control
GNSS	Global Navigation Satellite System
GOES	Geostationary Operational Environmental Satellites
GPS	Global Positioning System
GSHHG	Global Self-consistent, Hierarchical, High-resolution, Geography Database
HQP	Highly Qualified Personnel
IASI	Infrared Atmospheric Sounding Interferometer
IERS	International Earth Orientation and Reference Systems Service
JAIVEx	Joint Airborne IASI Validation Experiment
KML	Key Markup Language
MAE	Mean Absolute Error
MODIS	Moderate Resolution Imaging Spectroradiometer
MWRI	Microwave Radiation Imager
NASA	National Aeronautics and Space Administration
NGA	National Geospatial Intelligence Agency
NIR	Near Infrared
NOAA	National Oceanic and Atmospheric Administration

NORAD	North American Aerospace Defense Command
OAP	Off-axis Parabolic Mirror
ODCS	Orbit Determination and Control System
OMI	Ozone Monitoring Instrument
REST	Representational State Transfer
RF	Radio Frequency
RMSE	Root Mean Square Error
SMAP	Soil Moisture Active and Passive
SPOT	Satellite Pour l'Observation de la Terre
SSM/I	Special Sensor Microwave/Imager
SSMIS	Special Sensor Microwave Imager/Sounder
TLE	Two-Line Element
TRMM	Tropical Rainfall Measuring Mission
UAV	Unmanned Aerial Vehicle
UHF	Ultra High Frequency
URL	Uniform Resource Locator
USNO	U.S. Naval Observatory
VHF	Very High Frequency
VIRS	Visible and Infrared Scanner
VTOL	Vertical Take-off and Landing
WDBII	World Databank II
WVS	World Vector Shoreline

List of Symbols

a	Semi-major axis of FLAME-NIR instantaneous FOV ellipse
a_i	Lamp calibration constants for SN7~1993 ($i = 1, \dots, 8$)
b	Semi-minor axis of FLAME-NIR instantaneous FOV ellipse
C_{col}	Collimation error correction factor
c	Speed of light
D_{PX}	Mean distance per pixel in the cross-flight direction
D_{PY}	Mean distance per pixel in the along-flight direction
E_p	Energy of a photon at wavelength λ
H	Height of Raspberry Pi camera above ground
h	Planck Constant
I	Inflection point of a cubic polynomial fitted to R_i, \dots, R_{i+3}
JPC	Spectral exposure per detector count
l	Distance of calibrated lamp irradiance
L_A	Length on the ground observed by FLAME-NIR in the along-flight direction
L_C	Length on the ground observed by FLAME-NIR in the cross-flight direction
l_S	Line connecting polygon segment points S_i and S_{i+1}
l_B	Line connecting geolocation boresight points P_S and P_E

L_X	Length on the ground imaged by camera in the cross-flight direction
L_Y	Length on the ground imaged by camera in the along-flight direction
M	Irradiance of ORIEL calibrated lamp
N	Total number of Argus data sets analyzed
N_c	Number of detector counts in a NIR spectrometer measurement
n	Number of packets in an Argus data set
n_s	Number of scans setting of an Argus data set
$n_{s,i}$	Number of scans setting of the i^{th} spectral packet
P_E	Geodetic coordinates of boresight of end of Argus spectral packet
P_S	Geodetic coordinates of boresight of start of Argus spectral packet
QF_j	Timing quality factor of the j^{th} data set
R_i	Radiance of the i^{th} spectral packet
RFL	Reflected focal length
S_i	i^{th} element of GSHHG polygon segment S
S_{pp}	Number of samples per pixel setting in an Argus data set
T	Threshold value of inflection point method cubic polynomial fit
X_B	X-coordinate of boresight of FLAME-NIR FOV in image frame

X	Pixel number in cross-flight (horizontal) direction
X_{PC}	Number of pixels in camera image in the cross-flight direction
Y	Pixel number in along-flight (vertical) direction
Y_B	Y-coordinate of boresight of FLAME-NIR FOV in image frame
Y_{PC}	Number of pixels in camera image in the along-flight direction
α	74-DA along-slit field of view angle
α_{OAP}	Reflectance of off-axis parabolic mirror
β	74-DA cross-slit field of view angle
Δt^c	Calculated duration of an Argus data set consisting of n packets
Δt_e	Exposure time setting of a NIR spectrometer data set
$\Delta t_{e,i}$	Exposure time setting of the i^{th} spectral packet
Δt_i	Total duration of the i^{th} spectral packet
Δt_j^c	Calculated duration of the j^{th} data set
$\Delta t_j^{diff\%}$	Percentage difference between Δt_j^c and Δt_j^r
Δt_j^r	Requested duration of the j^{th} data set
Δt_{MAE}	Mean absolute error of $\Delta t_j^{diff\%}$ of all N data sets
Δt_p	Instrument packetization time
Δt_{RMSE}	Root mean square error of $\Delta t_j^{diff\%}$ of all N data sets
Δt_{RMSE}^c	Corrected root mean square error of $\Delta t_j^{diff\%}$ of all N data sets
ΔX	FLAME-NIR offset from image centre in cross-flight direction

ΔY	FLAME-NIR offset from image centre in along-flight direction
ΔZ	FLAME-NIR height offset from image centre
θ	Angle between OAP and spectrometer field of view
θ_X	Raspberry Pi horizontal field of view angle
θ_Y	Raspberry Pi vertical field of view angle
λ	Wavelength
σ_f	Standard deviation of the function $f(x_1, x_2, \dots, x_{k-1}, x_k)$

1 Introduction

Nanosatellites, defined as spacecraft with mass less than 10 kg, offer unique and novel opportunities not only for highly qualified personnel (HQP) training and technology demonstration, but also for space-based research, in particular in the field of Earth observation (EO) [1]. Many nanosatellites used in these missions are based on the CubeSat standard developed by Professors Jordi Puig-Suari at California Polytechnic State University and Professor Bob Twiggs at Stanford University, which defines a standard 1U CubeSat as a 10 cm x 10 cm x 10 cm cube with a maximum mass of 1.33 kg. Larger CubeSat form factors, such as the 2U and 3U, are stacks of the 1U CubeSat in volume and mass. The 2U CubeSat, for example, is a 20 cm x 10 cm x 10 cm prism with a 2.66 kg mass. EO CubeSat missions span a variety of objectives, ranging from spectrometric measurements for atmospheric chemistry, such as those around the 0.76 μm O₂ band and the 1.6 μm and 2.0 μm CO₂ bands, to medium resolution optical imaging of Earth's surface.

In this chapter, contextual information on nanosatellite technologies and Earth observation missions is provided in order to introduce the relevance of geolocation for these applications and the motivation for the current research.

1.1 Nanosatellite-Based Earth Observation Missions

Successful CubeSat missions initially began as technology demonstration and HQP training missions, with a particular focus on testing onboard subsystems in the space environment. An example of an early CubeSat technology mission was DELFI-C3, a

CubeSat developed at the Delft University of Technology and launched on April 28, 2008 [2]. The mission successfully demonstrated thin film solar array technology for the spacecraft power subsystem, autonomous wireless sun sensors for attitude determination and control, and an amateur radio platform for communications.

The success of these technology demonstration missions allowed for CubeSat missions to be developed for communications, EO, and other space-based science missions. For example, the United States Naval Academy's MARScam mission, launched on December 12, 2006, was an early CubeSat mission consisting of two 5 kg CubeSats with experimental communications payloads [3]. The primary objective of the mission was to provide a low cost communication system for training the United States Navy Marine Corps communication personnel [4].

Successful EO missions include the Flock 1 satellite constellation, launched by Planet Labs in early 2014 [5]. The constellation consisted of 28 satellites for imaging Earth using RGB cameras at a resolution of 3 to 5 m and was built only using Commercial Off-the-Shelf (COTS) technology. The satellites each carried a telescope and a charge-coupled device (CCD) camera with a Bayer-mask filter and operated in a 400 km orbit [6]. Data were acquired from the satellites using a radio frequency (RF) link to remotely operated ground stations, which then transmitted the data to Mission Control and storage.

CubeSat science missions include NASA's PharmaSat mission, a 10 pound satellite designed to detect the growth, density, and health of yeast cells for research into microgravity [7]. PharmaSat's subsystems consisted of an optical sensor for monitoring

the health and size of the yeast cells, a microfluidics system consisting of 48 small holes to store four separate small groups of yeast cells and provide sugars to the samples, and an environmental control and power system. The system provided an antifungal agent at different dosages to three of the yeast samples, monitored their health, and transmitted the results to scientists on Earth for analysis.

The demand for CubeSat missions has continually increased over the past seventeen years due to improvements in technology miniaturization. An ongoing survey of CubeSat missions by Michael Swartwout at Saint Louis University has catalogued a total of 614 missions that have been launched from February 6, 2000 up to April 17, 2017 [8]. An analysis of these missions has found a greater proportion of EO and science missions over the last few years, as compared to traditional missions focused on education, with the greatest proportions of CubeSat missions being dedicated to EO as of 2015 [9]. The number of CubeSat launches has grown from a handful per year in the early 2000s to a peak of over 100 launches in 2014, according to [10]. Launch projections made for 2017 by SpaceWorks Enterprises Inc. project a continuing increase in launches of nanosatellites such as CubeSats, and microsattellites by 10% per year [11]. A breakdown of the mission types for the projected launches from 2017 to 2019 shows that EO and remote sensing missions are expected to make up 64% of upcoming missions and other scientific missions making up 15% of upcoming missions. Technology demonstration missions, historically the most common nanosatellite mission type, are expected to make up only 14% of projected nanosatellite and microsattellite missions. CubeSats are expected to make up over 90% of

future nanosatellite and microsatellite missions, with the 30 cm x 10 cm x 10 cm 3U CubeSat as the most common form factor used.

A recent survey by Poghosyan and Golkar catalogued nanosatellite capabilities in terms of enabling technologies, i.e. nanosatellite bus and subsystem technologies, and payload capabilities [12]. Nanosatellite subsystems in the survey are broken down into seven categories, called structure, power, propulsion, guidance, navigation and control (GNC), communications, command and data handling, and thermal control. An analysis of nanosatellite structures found that few science missions are performed with form factors smaller than 2U and that the 3U, 6U, and 12U form factors are becoming more common for science missions. Larger form factors, such as the 12U and 27U, are currently under development as well, but no deployment systems with flight heritage currently exist for these form factors.

Current nanosatellite power subsystems consist of body-mounted or deployable solar panels, with batteries used for storage and power generation in solar eclipse conditions. An analysis of solar cell arrays used on nanosatellites by NASA's Mission Design Division found that nanosatellite solar cell efficiencies typically range from 20% to 30% [13]. When used in a deployable configuration on 3U CubeSats, solar arrays are capable of generating over 20 W of power [14].

Many propulsion systems for nanosatellite missions have been designed and launched over the last five years and can be classified under six categories [12]. These categories are cold gas thrusters, pulsed plasma thrusters, vacuum arc thrusters, electrosprays, resistojets, and

solar sails. Specific impulse values for these systems range from 40 s to 4000 s, with thrust values ranging from Micronewtons to Newtons [13].

GNC subsystems consist of orbit determination and control (ODCS) and attitude determination and control systems (ADCS) [12]. ODCS is typically accomplished in Earth orbit using Global Navigation Satellite Systems (GNSS), such as the Global Positioning System (GPS). ADCS use a combination of three axis magnetometers, Sun sensors, Earth sensors, and star trackers to achieve attitude determination at an accuracy of up to 1 arc second and reaction wheels, magnetic torquers, and thrusters for attitude control [13]. Additionally, a 2015 survey of 426 CubeSat missions, with a focus on ADCS, found that slew rates greater than 10 deg/sec can be achieved on 3U CubeSat platforms using current ADCS technology [10].

Communication subsystems are one CubeSat subsystem that is showing rapid development. Traditionally, CubeSat subsystems consisted of transceivers operating with uplink and downlink frequencies in the ultra high frequency (UHF) and very high frequency (VHF) bands with data rates between 1200 bps and 9600 bps [15]. S-band has also been occasionally used as a secondary downlink, with data rates as high as 256 kbps. More recently, CubeSat missions have begun to develop and launch communication subsystems using X-band, with Ku and Ka band missions also under development [13]. Command and data handling systems, meanwhile, have traditionally used microcontrollers based on the Advanced RISC Machine (ARM) architecture, though open source hardware such as Arduino, Raspberry Pi, and Beaglebone are becoming more popular [13].

Thermal control subsystems on CubeSats have mostly been passive systems, i.e. systems without active power as an input [12]. These systems include the use multi-layer insulation, Sun shields, thermal coatings, thermal straps, louvers, radiators and heat pipes in order to control heat dissipation and ensure that spacecraft subsystems operate within their temperature requirements. Active thermal control systems, such as thermoelectric coolers, are required for missions and payloads, such as photodiodes, that require a high level of thermal control [1].

1.2 Geolocation in Earth Observation Missions

While there has been significant advancement made in the area of scientific missions onboard CubeSats in the last decade (partly due to the technological development in micro-optics research) there still exists a gap in technology that prohibits the acquisition of reliable, accurate, and repeatable scientific measurements aboard nanosatellites. A critical area in delivering accurate and reliable scientific data from an EO spaceborne measurement system is the accuracy in correlating the data with the location on ground from which the measurement is made, i.e. geolocation accuracy. Geolocation accuracy is typically a mission requirement, which depends on spacecraft attitude knowledge, attitude control, orbit determination, and timing accuracies.

In missions that require a high degree of geolocation accuracy, further validation efforts are focused on post-launch, in-situ or airborne campaigns to assist with the effort. On-orbit, post-launch geolocation techniques such as comparison of the payload data with established ground control points (GCPs) or other terrestrial features that are identifiable

in the payload data and simultaneous measurements from airborne platforms and satellites have been applied to examine the geolocation accuracy and subsequently apply corrections. For example, GCPs were used to validate the geolocation accuracy of the QuickBird-2 and WorldView-1 satellite missions [16]. Geolocation accuracies of 14 m to 21 m and 4.0 m to 5.3 m were observed respectively for QuickBird-2 and WorldView-1 imagery by comparing the difference between the locations of the GCPs in the images with their known coordinates. However, GCP validation methods, are typically used in high resolution or large field of view imagers and are therefore not always compatible with CubeSat payloads.

1.3 Automated Geolocation

Conventionally, geolocation is performed by operators at the time of data processing. However, as data sets increase in size and volume, a need for rapid geolocation arises. Consequently, the automation of geolocation processes is required to handle these large data sets in more efficient and timely ways. While there are several methodologies for performing geolocation, there are limited published methods for automated geolocation for validation. In particular, there are no known automated geolocation algorithms for validating CubeSat based EO data sets.

Observations made from CubeSat platforms tend to be more constrained due to the size of the spacecraft and therefore standard geolocation validation techniques cannot be readily applied. For example, power constraints limit the volume of data available to apply techniques such as observing GCPs [5]. Payload resolution constraints also make detection of terrestrial features difficult.

1.4 Unmanned Aerial Vehicle Based Geolocation Validation

Airborne validation campaigns provide a method for calibration and validation of payloads under controlled conditions. Airborne validation campaigns involve testing EO instruments in order to characterize the performance of those instruments outside tightly controlled laboratory conditions. This approach allows the instrument or instrument application to be examined in real world conditions, but still allowing for reducing uncertainties due to unpredictable variables such as weather. This type of experimental control is particularly important for validation of EO payloads designed for space missions that are under test prior to integration of those payloads with satellites. Additionally, airborne campaigns are conducted for calibrating spaceborne payloads post-launch by simultaneously acquiring data using the payload from the air and from space and comparing the results, with the airborne payload data used as a form of ground truth.

Unmanned aerial vehicles (UAV) are relatively new research tools for instrument validation as they provide opportunities for low cost and easy access to remote sensing conditions for spaceborne instruments. UAVs have many similarities to CubeSats in size, mass, and power. While these constraints limit the types of payloads that the platform can accommodate, they provide flight test opportunities for the payloads prior to launch into space. Typically, CubeSat based payloads and analysis methodologies are only tested in laboratory conditions prior to launch without proper field tests for verification or validation. Once launched, it is difficult to verify the performance of spaceborne payloads and data analysis methodologies.

However, there are also a number of limitations of conducting UAV-based validation campaigns. Due to government regulations, meteorological conditions, and technical limitations of the UAV platforms, validation campaigns may not sufficiently resemble onboard conditions to provide appropriate data for validation.

In this research, an automated approach for geolocation of CubeSat-class nanosatellite missions with low-resolution spectrometers is examined. The spectrometers used for the research are single pixel imagers with a broad spectral window and are used in both nanosatellite applications and UAV based airborne validation campaigns.

1.5 Argus 1000 and FLAME-NIR Spectrometers

Two near-infrared spectrometers were used in this research as typical CubeSat class payloads. Argus 1000, made by Thoth Technology, is a space qualified spectrometer that operates in the 950 nm to 1700 nm region in a nadir viewing configuration and was flown aboard the CanX-2 nanosatellite mission in December 2008, detailed in [17]. The Argus 1000 data from CanX-2 was used to develop the automated geolocation algorithm for spaceborne data. Geolocation tools for Argus 1000 spectrometer data were previously developed for individual data sets. 343 Argus data sets were acquired from 2009 through 2015. The geolocation tools developed for analysis of Argus 1000 data involved combining spacecraft position and attitude data in order to determine the geodetic coordinates of the boresight of Argus 1000. Additionally, analysis of the spacecraft position, attitude knowledge, and attitude control uncertainties allowed the geolocation uncertainty of Argus data to be determined.

The FLAME-NIR, by Ocean Optics, is a near-infrared spectrometer that operates in the 927 nm to 1658 nm region and is primarily used in terrestrial applications. FLAME-NIR data was used to validate the automated geolocation algorithm on a custom UAV platform. Eight data sets were collected at two data collection sites in October 2016.

1.6 Dissertation Contributions

In a nanosatellite application (in particular, CubeSat-class platform with degree-level pointing accuracy), geolocation accuracy plays a significant role, yet there have been few attempts to either understand/analyze or correct/improve the accuracy using the scientific data on board the spacecraft. This research is the first attempt of its kind to (1) understand the sources of the geolocation error in a CubeSat-class satellite; (2) provide a novel method to automatically assess the geolocation accuracy from the spaceborne spectroscopy measurements using coastline detection and (3) present techniques to validate the geolocation accuracy assessment algorithm with airborne data.

While the concept of assessing geolocation accuracy using coastline detection is well established in literature, the implementation of applying this technique for CubeSat-class, NIR spectrometers is novel. The proposed method of geolocation algorithm is then examined with a set of spaceborne NIR spectrometer data from the Argus mission aboard the CanX-2 spacecraft and an airborne campaign onboard a UAV using FLAME-NIR data.

1.7 Dissertation Outline

The dissertation details the development of an automated geolocation algorithm for spaceborne NIR spectrometer data, using Argus 1000 on the CanX-2 nanosatellite. An

airborne validation campaign of the proposed geolocation accuracy assessment algorithm is also performed using an Ocean Optics FLAME-NIR spectrometer.

This chapter introduces the concept and capabilities of nanosatellites, along with the need for automated geolocation of spaceborne NIR data and the scope of the dissertation. Additionally, the satellite mission and NIR instruments for which the automated geolocation algorithms have been implemented are described.

Chapter 2 discusses the current state of automation for satellite mission operations and post-processing of EO satellite data. Additionally, the method of assessing geolocation accuracy using coastline detection is described, along with its implementation on a series of satellite missions. Additionally, Chapter 2 discusses the design of airborne validation campaigns for EO payloads, along with results of recent validation campaigns.

In Chapter 3, the automated processing of the Argus spectrometer data is described, along with a description of geolocation error sources. Specifically, Chapter 3 describes the process of combining Argus science and engineering data to generate data products, along with the data quality validation techniques.

Chapter 4 describes the automated coastline detection algorithm that has been implemented for assessing geolocation accuracy of NIR spectrometer data, along with its implementation on Argus data. Results from the analysis are also presented.

Chapter 5 and 6 detail the validation process of the coastline detection algorithm introduced in Chapter 4 using an airborne validation campaign. Specifically, the radiometric

calibration of two NIR spectrometers are described in Chapter 5, while Chapter 6 discusses the corresponding airborne validation platforms used for the validation campaign. The results of the airborne campaign methods are implemented and presented in Chapter 6.

Lastly, Chapter 7 concludes the dissertation by summarizing the results of the implemented automated geolocation algorithm and discussing methods to improve geolocation in the future.

2 Literature Review

In this chapter, a discussion of the recent application of automation of satellite operations, coastline detection for geolocation accuracy assessment, and airborne validation campaigns is discussed.

2.1 Automation of Satellite Operations and Data Analysis

The need for automation of satellite operations and data analysis has been a constant theme of many studies over the last twenty years, particularly with the demand for near real-time access to payload data and with a desire for reduced cost of satellite operations.

For small satellites, a mission concept for autonomy of spacecraft tasks was discussed in [18]. The mission concept called for a 500 mm x 560 mm spacecraft with a mass of 60 kg to be launched into an 800 km orbit with a multi-band imager as an EO payload. The mission concept classified the mission autonomy into three categories, each controlling one aspect of onboard operations. These categories were autonomous spacecraft control, autonomous fault management, and operational autonomy. Autonomy was described to be particularly beneficial in ground communications, rapid anomaly handling, and improvement of the quality of mission products.

Another framework for automation of satellite operations was the National Aeronautics and Space Administration's (NASA) Automated Scheduling and Planning Environment (ASPEN) [19]. ASPEN was a reconfigurable framework that combined both planning and scheduling tasks. It would assemble a near-optimal schedule using search algorithms

applied to activities constrained by time, state, and resource requirements. ASPEN was designed as a ground-based scheduling system that would allow non-operations personnel such as data users to generate schedules for satellite operations.

The European Space Agency (ESA) has also established standards for autonomous mission operations, which define requirements for autonomous operations in terms of observability and commandability [20]. Observability is defined as the visibility of the spacecraft's status, configuration, and performance, which must be provided to the ground segment at required levels of detail with acceptable time delays specified. Commandability refers to the ability of the control function of the spacecraft to achieve the mission objectives under all circumstances. Autonomy itself is defined using a four level system, with the lowest level corresponding to real-time control from the ground segment, with the highest level corresponding to goal-oriented mission planning being executed onboard the spacecraft. Two levels of on-board fault management procedures are also defined.

With regard to satellite data analysis, automation of analysis tasks has been a growing part of research, such as for registration of satellite imagery as discussed in [21]. This approach was designed for registering satellite images from different sensors and therefore used a rule based system to select an image registration method for a particular image set. Image registration was performed based on the method of wavelet transforms.

Another example of automation of satellite image registration was applied to Satellite Pour l'Observation de la Terre (SPOT) imagery in [22]. This method involves two steps for accomplishing image registration. In the first step, control points are automatically

generated using a normalized cross correlation. In the second step, a mapping function is determined using the control points.

Automation of satellite data analysis also extends to feature extraction, such as road extraction as implemented in [23]. This implementation involved applying global thresholds to segment the image. Different thresholds are applied depending on images features near the roads, such as vegetation and buildings. Morphological operations are used to perform the image segmentation.

Automated feature extraction was applied to synthetic aperture radar data to identify oil spills [24]. This approach involved the use of a fuzzy logic to analyze dark regions of radar imagery. Images were acquired, georeferenced, land masked, filtered, and threshold to extract the dark regions. Subsequently, probabilities were assigned to the dark regions based on their likelihood of being oil spills using fuzzy logic. 35 images were acquired over the Aegean Sea to test the algorithm, which resulted in a performance of 88%.

Furthermore, automation was applied to the extraction of 2-D building footprints from multispectral imagery, as described in [25]. The algorithm applied two methods of building detection, one based on detecting the shapes of the buildings in the imagery and one based on detecting the shadows cast by the buildings. Morphological operators were used in each method to extract the footprints of the buildings, with six parameters used to control whether a feature would be classified as a building or building shadow. The method was tested on IKONOS imagery and found to extract buildings accurately, but was also incomplete.

Extraction of cloud motion in satellite imagery was another task to which automation was applied [26]. A pair of images, acquired from the ATS-1 satellite, were mapped onto Mercator projections and searched for cloud motion using cross-correlation analysis. A fast Fourier transform was used to determine the cross-correlation coefficients and was found to improve on manual techniques when applied to images containing a single cloud layer. A comparison of 300 vectors showed that automated methods performed as well as manual methods for the calculation of direction, but outperformed manual methods for the calculations of speed in single layer cloud images.

Detection of volcano hot spot detection in imagery from the Geostationary Operational Environmental Satellites (GOES) was also automated [27]. In this application, temperature differences in GOES imagery in the Channel 2 and Channel 4 bands were used in successive GOES images over Kilauea, Hawaii in order to determine hot spot locations. The automated algorithm would enhance the contrast of GOES images and then search for hot spots using the temperature differences. Additionally, local differences in the temperatures in Channel 2 were also used to search for anomalies in the images, with Channel 1 data used to detect anomalies caused by the presence of clouds by calculating a cloud index. The automated algorithm would produce hot spot images formed using the temperature differences, a cloud image, and a colour image formed from combining three channels of images. Additionally, a hot spot movie was produced using the temperature difference images, acquired in 15 minute intervals and spanning a three to five day period. Graphs of the anomalies detected and cloud index were also generated and uploaded along

with the hot spot movie and images to a server for public use. Lastly, thresholds were applied to the hot spot anomalies and used to automatically send e-mail alerts.

Automation in geolocation is a relatively new area of study under the general approach in automated satellite operations. It can be used to supplement automated satellite operations by analyzing EO data for parameters that can potentially be used in the automated decision making process.

2.2 Coastline Detection for Geolocation Accuracy Assessment

In [28], several techniques are used for validating geolocation accuracy for spacecraft missions. In this study, the focus is on coastline detection as the primary method for geolocation accuracy assessment. Coastline detection is a method for assessing and improving geolocation accuracy that has been implemented for several satellites over the years. Coastline detection itself involves the use of payload data to identify coastlines and link their time of acquisition to onboard attitude errors.

One of the first implementations of a coastline detection algorithm for the assessment of geolocation accuracy occurred on the Earth Radiation Budget Experiment (ERBE), a three satellite system consisting of NOAA-9, NOAA-10, and the Earth Radiation Budget Satellite (ERBS) launched in 1984 [29]. ERBE contained a scanner, consisting of three Earth observing channels with a 40 km field of view at nadir, and a nonscanner consisting of four Earth observing channels. The coastline detection algorithm for the scanner involved imaging a series of four coastal sites, chosen due to four criteria. Thermal temperatures measured by the scanner as the sites were observed were used to identify the

coastlines by fitting a cubic polynomial to each set of four measurements in a scan, as shown in Figure 2-1.

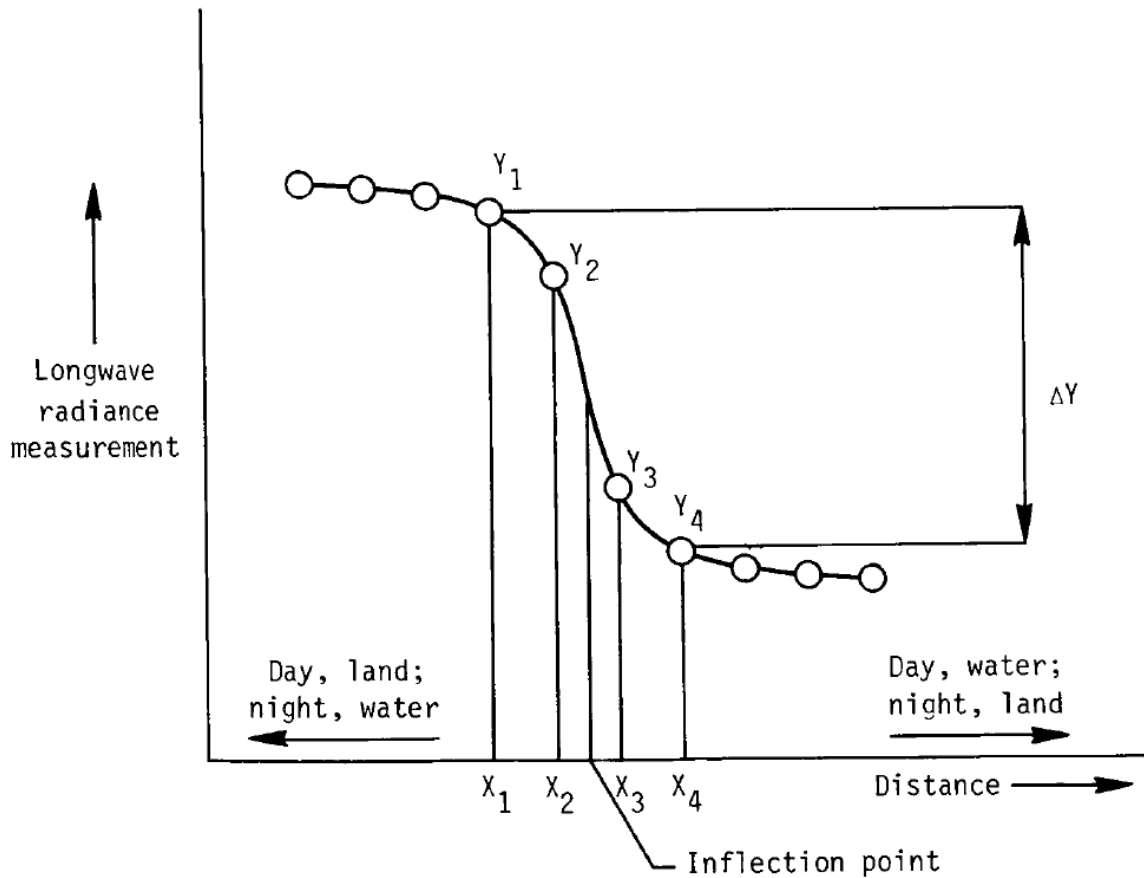


Figure 2-1 Cubic polynomial fit for a series of four consecutive radiance measurements for coastline detection of ERBE instruments [29]

If the difference in radiance between the first and last radiance measurements was greater than a pre-defined threshold value, the inflection point of the polynomial was used to locate the coastline crossings, which were then compared to the geographic locations of the coastline crossings in the scenes. This was done over multiple passes of the sites.

Ultimately, though a bias in the cross-track direction of -0.03° was found, the geolocation errors were much smaller than the scanner field of view.

An improved version of the coastline detection developed for ERBE was implemented for the Clouds and the Earth's Radiant Energy System (CERES) instrument, launched aboard the Tropical Rainfall Measuring Mission (TRMM) satellite in 1997 [30]. The CERES instrument was an improved version of ERBE, consisting of a scanning, three channel radiometer. The improved coastline detection algorithm allowed any coastline site to be used, rather than just the four used for ERBE, and used additional Visible and Infrared Scanner (VIRS) for cloud screening. Mean errors of -0.58 km in the along-track direction and 0.48 km in the cross-track direction were found after processing datasets over multiple passes.

An automated version of the coastline detection algorithm used for CERES on TRMM was implemented for CERES instruments aboard the Terra and Aqua satellites, launched in December 1999 and May 2002 respectively [31]. Each satellite contained two CERES instruments, called FM1 and FM2 for Terra and FM3 and FM4 for Aqua. This version of the coastline detection algorithm employed automated cloud cover identification using additional CERES data products. Additionally, high latitude data, i.e. data at latitudes greater than $\pm 70^\circ$, was excluded from the coastline detection analysis due to effects of non-normal scattering on coastline identification. For Terra, biases of -1 km and 0 km were found in the along-track and cross-track direction, respectively, for FM1 data and biases of -0.5 km and -1.5 km were found in the along-track and cross-track direction respectively

for FM2 data. For Aqua, biases of -0.8 km and 1.4 km were found in the along-track and cross-track direction respectively for FM3 data and biases of 0 km and -0.5 km were found in the along-track and cross-track direction respectively for FM4 data.

Automated coastline detection was also used for correcting geolocation error in the Cloud-Aerosol Lidar Infrared Pathfinder Satellite Observations (CALIPSO) mission, consisting of a wide field camera and a co-aligned imaging infrared radiometer [32]. Coastline detection was applied to the radiometer data using the same approach as for ERBE, with coastline detections then compared to a coastline database. Coastline offset errors were then corrected and subsequently compared to simulated wide field camera, which was generated using an external data source, in order to determine the uncertainty in the coastline detection and correction process.

Another use of coastline detection for assessing geolocation accuracy occurred for data obtained with the Special Sensor Microwave/Imager (SSM/I) [33]. In that analysis, geolocation errors ranging from 20-30 km were found in SSM/I imagery when they were compared to coastline imagery, well above the 7 km requirement of the mission. Six error sources were considered for the cause of the geolocation error. These were errors in the spacecraft orbital elements, spacecraft ephemeris data predictions, the sensor pixel location algorithm, alignment of spin axis, sensor alignment to the spacecraft, and spacecraft attitude. Ultimately, the most significant source of the geolocation error was found to be the spacecraft attitude, to which corrections were applied that reduced the geolocation error to 5-7 km.

A similar approach to the coastline detection method used for SSM/I imagery was applied to WindSat flight data, launched aboard the Coriolis satellite in 2003 [34]. The approach involved two independent sets of analysis and corrections in order to differentiate between pointing and timing errors in the WindSat imagery. Coastline locations in WindSat data were found by determining the local maximum of the gradient of a cubic spline function used to interpolate between data points. The first step in the correction process involved correcting coastline matching errors by inserting timing corrections into the data, while the second involved using a scan bias analysis to find any remaining pointing errors present in the data. This approach successfully improved the geolocation accuracy to less than 5 km.

Furthermore, improvements to the coastline detection were implemented for the Special Sensor Microwave Imager/Sounder (SSMIS) mission, launched aboard F-16 spacecraft [35]. The improved algorithm used the partial derivatives of the SSMIS data to automatically determine coastline locations. This technique was useful in assessing a 20-30 km geolocation error in SSMIS data, which was then corrected using angular and timing offsets. The corrections applied to the data reduced the geolocation error to less than 4-5 km.

Geolocation error correction was also implemented using coastline detection for Advanced Microwave Scanning Radiometer for Earth Observing System (AMSR-E) data [36]. This method involved comparing the brightness temperatures in AMSR-E data over coastlines for ascending and descending passes to assess geolocation error. The resulting differences were used to optimize the nadir and scan angles of the instrument.

Coastline detection was also used for verifying geolocation accuracy of spectrometers in the UV and visible wavelength range, such as in the case of the Ozone Monitoring Instrument (OMI) [37]. False colour RGB OMI data over regions of interest was compared to coastline data from the CIA World Databank II (WDBII) database to determine geolocation offsets. Over a two year period from January 2005 to December 2006, 14 to 19 scenes were analyzed per month, with latitude and longitude offsets determined. Ultimately, OMI imagery was found to have mean geolocation offsets of 0.79 km in latitude and 0.29 km in longitude from the WDBII database.

Verification of the geolocation accuracy of the Atmospheric Infrared Sounder (AIRS) involved the use of coastline detection with simulated data [38]. Simulated AIRS data were generated from Moderate Resolution Imaging Spectroradiometer (MODIS) data and compared to selected coastline scenes as in the methods used for ERBE and CERES data. For AIRS data, only scenes with at least six coastline crossings were used for the geolocation analysis, which determined the latitude and longitude offsets between the coastline crossings observed in the data and actual coastline crossing locations. In total, seven scenes were analyzed, which verified that the AIRS boresight data could be geolocated to within 1.7 km.

More recently, coastline detection was implemented for microwave satellite data aboard five satellites from the National Oceanic and Atmospheric Administration's (NOAA) Polar Operational Environmental Satellite program [39]. This method involved analyzing ascending and descending coastline observations for NOAA-15 to NOAA-19 data and

linking the results to onboard attitude errors. NOAA-15 instruments were found to have mounting errors of 1.2° in the cross-track direction and -0.5° in the along-track direction, while NOAA-16 and NOAA-18 instruments were found to have mounting errors of -0.5° and -1° in the along-track direction, respectively.

Two methods of coastline detection were implemented for microwave data of the Microwave Radiation Imager (MWRI) aboard the FengYun-3C satellite [40]. The first method involved using the inflection point of a cubic polynomial to determine coastline locations in MWRI data and comparing them to a coastline database, as in [29]. Three scenes were selected for the coastline detection analysis of MWRI data due to the high contrast between land and water present in those scenes. Mean geolocation errors of 0.05° and -0.1° were found in the in-track and cross-track direction, respectively, using the inflection point method, with corrections to the spacecraft attitude reducing these errors to less than 0.01° . The second method applied to MWRI data involved a comparison of the observed brightness temperatures in the data at coastal regions for ascending and descending nodes, as in [39]. Ultimately, mean biases of -0.02° , -0.52° , and 0.27° were found in the roll, pitch, and yaw angles, respectively.

Coastline detection was also applied to assess geolocation accuracy of the microwave radiometer (MWR) data for the Aquarius/SAC-D mission [41]. The system consisted of eight beams, which scanned Earth in a push broom orientation at three channels. Changes in brightness temperature for the footprint of each beam occurred as each beam crossed coastlines, the locations of which were compared to coastline maps. Beam locations with

maximum slope changes are used to detect coastline crossings in the radiometer data. Mean errors of less than 15 km were observed for all eight beams.

Lastly, coastline detection was applied for geolocation accuracy analysis of the Soil Moisture Active and Passive (SMAP) instruments, launched in January 2015 [42]. SMAP consists of two instruments, a passive radiometer and an active synthetic aperture radar. Coastline detection was applied to areas not smaller than the radiometer instrument's footprint of 39 km by 47 km. 44 orbits of data over a one year period were selected for the coastline detection analysis and were used to verify that the geolocation accuracy requirement of 4 km.

The coastline detection algorithms described above can be categorized into four general categories based on the coastline detection method, as shown in Table 2-1. These categories are:

1. Inflection point method: Coastline locations are determined by finding the inflection point of a cubic polynomial fitted to four consecutive measurements
2. Local of maximum gradient: Coastline locations are determined by finding the local maximum of the gradient of the instrument as it scans the coastline
3. Node differential method: Differences in brightness temperatures at the coastline locations for ascending and descending passes of an observed site are used to calculate coastline offsets
4. Visual inspection of offsets: Operators manually determine the mismatch between coastline maps generated using imagers and known coastline maps

Table 2-1 Summary of coastline detection methods used for geolocation validation

Instrument Name	Satellite Name	Instrument Type	Coastline Detection Method	Automation Level	False Detection Method	Geolocation Requirements	Geolocation Accuracy Achieved
Advanced Microwave Scanning Radiometer for Earth Observing System (AMSR-E)	Aqua (EOS-PM1)	Passive scanning microwave: 6 – 89 GHz	Node differential method	N/A	None	N/A	3.5 – 7 km
Advanced Microwave Sounding Unit (AMSU)	NOAA-15 to NOAA-19	Microwave: AMSU-A2 Channel 1 23.8 GHz, AMSU-A2 Channel 2 31.4 GHz, AMSU-A1 Channel 3 50.3 GHz, AMSU-A1 Channel 15 and AMSU-B 89.0 GHz	Node differential method	N/A	N/A	N/A	NOAA-15 AMSU-A2: -0.5° along-track and 1.2° cross-track NOAA-16 AMSU-A1 and AMSU-A2: -0.5° along-track NOAA-18 AMSU-A2: -1° along-track
Atmospheric Infrared Sounder (AIRS)	Aqua (EOS-PM1)	Thermal infrared spectrometer: 3.7 – 15.4 μm Visible photometer: 0.4 – 1.0 μm [43]	Inflection point method	Automated detection and analysis for a manually selected scene	External GOES data used for cloud free scene selection	2 km	0.5 km – 1.7 km
Clouds and the Earth's Radiant Energy System (CERES)	Aqua (EOS-PM1)	Three scanning bolometers: (Shortwave) 0.3 – 3.5 μm,	Inflection point method	Automated detection and analysis for a manually	Manual scene inspection for cloud presence	20 km	FM3: 0.8 km along-track and 1.4 km cross-track

		(Window) 8 – 12 μm , (Total) 0.3 - >100 μm		selected scene			FM4: 0.5 km cross-track
	Terra (EOS-AM1)					20 km	FM1: 1 km along-track FM2: 0.5 km along-track and 1.5 km cross-track
	Tropical Rainfall Measuring Mission (TRMM)					N/A	<1 km
Earth Radiation Budget Experiment (ERBE)	Earth Radiation Budget Satellite (ERBS), NOAA 9, NOAA 10	Three scanning bolometers: (Shortwave) 0.2 – 5.0 μm , (Longwave) 0.5 – 50.0 μm , (Total) 0.2 – 50.0 μm [44]	Inflection point method	Manual selection of four scenes for analysis	Manual scene inspection for cloud presence	N/A	0.49 km along-track and 0.09 km cross-track
Infrared Imaging Radiometer and Wide Field Camera	Cloud-Aerosol Lidar Infrared Pathfinder Satellite Observations (CALIPSO)	Imaging Infrared Radiometer: 8.7 – 12.0 μm , Wide Field Camera: (Visible) 0.645 μm	Inflection point method	Automated detection and analysis	Manual scene inspection for cloud presence	N/A	Wide field camera: 100 m
Microwave Humidity Sensors (MHS)	NOAA-18, NOAA-19	Microwave: 89.0 GHz	Node differential method	N/A	N/A	N/A	N/A
Microwave Radiation Imager (MWRI)	FengYun-3C	Microwave: 10.65, 18.7, 23.8, 36.5, 89.0 GHz	Inflection point method and node differential method	N/A	External MERSI data used for cloud free scene selection	Not defined	0.01° in both in-track and cross-track directions

Microwave Radiometer (MWR)	Aquarius/SAC-D	Microwave push-broom: 23.8, 36.5 GHz	Local maximum of gradient	N/A	Detection threshold used	N/A	<15 km
Ozone Monitoring Instrument (OMI)	EOS-Aura (EOS-CH1)	Visible: 484, 420, and 360 nm	Visual inspection of offsets	None	None	N/A	Latitude: 0.79 km Longitude: 0.29 km
Soil Moisture Active and Passive (SMAP)	Soil Moisture Active and Passive (SMAP)	Passive radiometer: 1.41 GHz, Active synthetic aperture radar: 1.2 GHz	Local maximum of gradient	Manual selection of 44 orbits for analysis	Four quality checks applied based on threshold levels	4 km	2.5 km
Special Sensor Microwave Imager/Sounder (SSMIS)	Defense Meteorological Satellite Program (DMSP) F-16, F-17, F-18	Microwave radiometer: 19.35 – 183 GHz	Local maximum of gradient	Automated search for crossings in radiometric data	None	Channels 12 – 18: <7 km Remaining Channels: <12.5 km	4-5 km
Special Sensor Microwave Imager (SSM/I)	Defense Meteorological Satellite Program (DMSP) Block 5D-2	Microwave radiometer: 85.5 GHz	Visual inspection of offsets	N/A	None	7 km	<7 km
WindSat Radiometer	Coriolis	Total power radiometers: 6.8, 10.7, 18.7, 23.8, and 37.0 GHz	Local maximum of gradient	Automated search for crossings in radiometric data	N/A	±1 km	<1 km

2.3 Airborne Validation Campaigns

As described in 1.4, airborne campaigns are often used for validation of spacecraft payload performance under controlled conditions. One airborne campaign that involved simultaneous measurements from aircraft and spacecraft occurred for the Airborne

Polarimetric Microwave Imaging Radiometer (APMIR), which was flown for calibration and validation of WindSat data, launched aboard the Coriolis spacecraft, and SSMIS data [45]. AMPIR was flown over the Atlantic Ocean from Nova Scotia to Florida, underneath WindSat and SSMIS. It was mounted on a gimballed system. Data was taken around the entire azimuth, with calibration targets in the ocean also detected. Brightness temperatures were determined for both the WindSat and AMPIR data as the instruments viewed the same location and were found to be close in magnitude.

Another airborne validation campaign of spacecraft EO data was the Joint Airborne IASI Validation Experiment (JAIVEx), flown during April 2007 and May 2007 [46]. JAIVEx was an airborne validation campaign launched over a 7 day period to validate observations for the Infrared Atmospheric Sounding Interferometer (IASI), launched aboard MetOp-A in October 2006. The JAIVEx campaign consisted of two aircraft flown under MetOp-A for validation of IASI data, with two onboard sensors, an interferometer and a high resolution spectrometer, as payloads. Data from the airborne campaign was used for radiometric and spectral calibration of IASI data, validation of IASI data against Aqua radiance data, validation of forward radiative transfer models, and validation of retrieved geophysical products. Ultimately, the JAIVEx campaign data were used to verify that IASI radiance measurements had an absolute accuracy of within 0.5 K.

Absolute calibration of SSM/I data also employed an airborne campaign [47]. Eighteen flights under the spaceborne SSM/I instrument were undertaken, ten of which were used for instrument calibration. The resolution of the airborne SSM/I radiometers was 1.5 km,

a much smaller area than the spaceborne radiometer resolution of 13 to 70 km and therefore requiring a greater time period for data collection. Clear sky regions without significant brightness changes were selected to limit errors due to these effects. Analysis of the flight SSM/I data with the spaceborne SSM/I data found an absolute calibration accuracy of ± 3 K for the spaceborne data.

One airborne campaign launched to validate instrument performance was the Digital Airborne Imaging Spectrometer Experiment (DAISEX'99) [48]. DAISEX'99 consisted of two hyperspectral spectrometers that were flown in order to demonstrate the retrieval of geophysical and biophysical variables such as the leaf area index, biomass, leaf water content, and canopy height for improving the understanding of the effect of these variables on ecosystems. DAISEX'99 was flown over a test site in Spain and produced images with a spatial resolution of 6 m x 6 m.

Another instrument tested on an airborne platform was a Fabry-Perot interferometer based hyperspectral imager developed by the VTT Technical Research Centre for Finland [49]. The hyperspectral imager was designed to operate in the 400 nm to 1100 nm spectral range with a ground pixel size of 3 cm to 5 cm. The purpose of the instrument was to acquire false colour imagery for generating digital surface models for forest applications and spectral images for crop monitoring applications. The instrument was flown on an airborne system consisting of an UAV with a GPS receiver for position data and a ground system for communications. The airborne validation campaign occurred in August 2011 over boreal areas for testing the false colour image acquisition and in July 2011 over test crop

fields for testing the spectral camera. The preliminary analysis showed that sufficient overlapping images were acquired for generating digital surface models.

As a follow up to this airborne validation campaign, a second validation campaign was flown by the VTT Technical Research Centre for Finland to test an algorithm developed for the Fabry-Perot imager for correcting the effects of illumination variations during flight [50]. The airborne campaign used a ground based irradiance measuring station and an irradiance sensor aboard the UAV to acquire irradiance measurements for correcting the effects of varying illuminations within the imager data. Data were collected under both cloudy and bright conditions, with the irradiance data collected both aboard the UAV and in situ using the ground station used to calculate correction factors for the illumination variations. The irradiance corrections provided improved homogeneity in the imager data, with the corrections performed using the ground based irradiance sensor outperforming the corrections calculated using UAV based irradiance sensor.

Airborne validation was also used for validating carbon monoxide measurements for the ACE-Fourier Transform Spectrometer aboard the Airborne Chemistry Experiment (ACE) [51]. This involved comparing carbon monoxide measurements from the ACE-FTS with measurements made over the same location by five aircraft through the MOZAIC program, which were accurate to ± 5 ppbv. The difference between the measurements made with the ACE-FTS and the airborne measurements was found to be less than 16%.

Post-launch validation of CALIPSO data was also achieved using an airborne validation campaign [52]. This campaign involved acquiring simultaneous observations of CALIPSO

data and airborne ER-2 Cloud Physics Lidar data, which was selected for its ability to fly higher than 20 km, thereby providing observations similar to the satellite. A total of 13 flights were made over different regions. The airborne data were successful in validating the calibration of CALIPSO level 1 data.

Furthermore, airborne validation was also applied to the Atmospheric Laser Doppler Instrument (ALADIN) on the ESA ADM-Aeolus mission [53]. ALADIN consisted of two spectrometers that determines the Doppler shift from aerosols and clouds at a wavelength of 355 nm by measuring Rayleigh and Mie scattering. An airborne prototype of the instrument was developed to validate the instrument concept prior to launch. The airborne campaign was performed in September 2009 over Greenland, Iceland, and the Atlantic Ocean, with wind speeds of -0.7 m/s and 1.9 m/s determined using the Rayleigh scattering measurements and 1.1 m/s and 1.3 m/s determined using the Mie scattering measurements [54].

In summary, airborne validation is becoming a more common approach to payload characterization. These platforms allow for simultaneous measurements with spaceborne payloads, along with standalone campaigns for instrument validation.

3 Automated Generation and Error Analysis of Spaceborne Spectrometer Data Products

In a typical EO mission, a data product refers to a set of EO instrument data collected from space that has been processed from its raw form into a format suitable for end use applications. Geolocation of an EO data product is an algorithm to determine the geodetic coordinates of the field of view of an Earth observing nadir pointing instrument. Geolocation of Argus NIR spectral data, used in this study, involves post-processing satellite position data, satellite attitude data, and Earth orientation parameters to determine the coordinates of the instrument data, as shown in Figure 3-1 and fully described in [28].

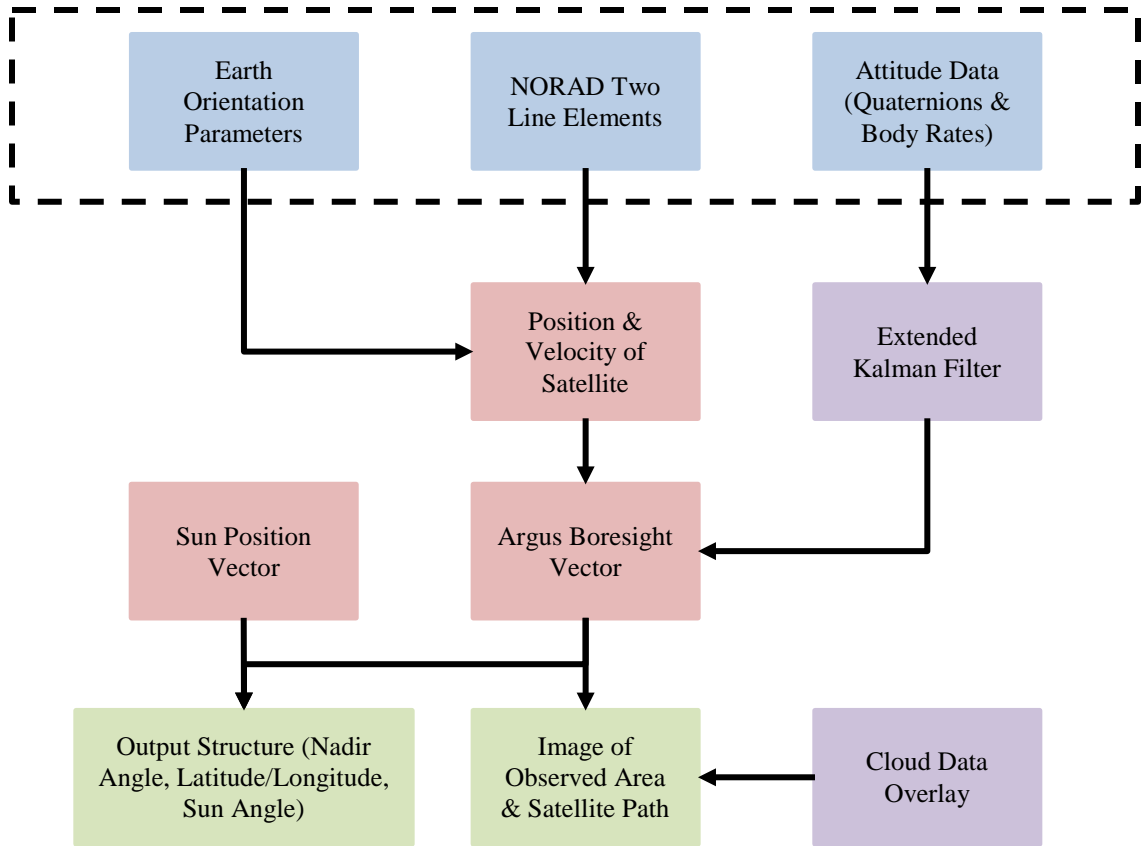


Figure 3-1 Block diagram of semi-automated geolocation algorithm of Argus data sets (adapted from [28])

The geolocation algorithm shown in Figure 3-1 describes how each data set is properly geolocated, with blocks shown in blue corresponding to raw input parameters, consisting of CanX-2 attitude quaternions and body rates, satellite position data acquired from North American Aerospace Defense Command (NORAD) in two-line element (TLE) format, and Earth Orientation Parameters (EOP) acquired from external sources. These inputs are used to generate key internal geolocation processing parameters, in particular the position vector to the Sun, the position and velocity of the spacecraft at data acquisition times, and the Argus boresight vector, as shown in the red blocks shown in Figure 3-1. The blocks shown

in purple correspond to optional processing, including an Extended Kalman Filter that uses the spacecraft dynamics rather than linear interpolation to determine the Argus boresight vector at data acquisition times and daily averages of cloud overlays. Lastly, the green blocks correspond to the geolocation outputs, including the geodetic latitude and longitude of each Argus spectral measurement and its associated field of view, the instrument nadir angle, and the Sun angle. The Argus spectral measurements themselves are measurements of spectral radiance at each pixel on the instrument detector, which correspond to a particular wavelength. Automation of the geolocation process is imperative and is a requirement in order to analyze large quantities of spectral data, but comes with its own sets of challenges.

3.1 Implementation of the Automated Geolocation Algorithm

The need for automated geolocation of Argus spectral data becomes apparent as the lifetime of the mission continues. As the number of data sets acquired increases, it becomes more advantageous to automate the acquisition and conversion of the raw data files into usable data for scientific analysis. Additionally, the desire for near real-time processing of spectral data enhances the need for automated geolocation.

The automated geolocation algorithm is designed to combine the raw CanX-2 attitude data and Argus spectral data into useful geolocation data for further analysis. Since the algorithm is automated, it must be able to process all Argus data sets, regardless of data quality. The different inputs and outputs are classified into a series of levels, representing the degree to which they have been processed as shown in Figure 3-2.

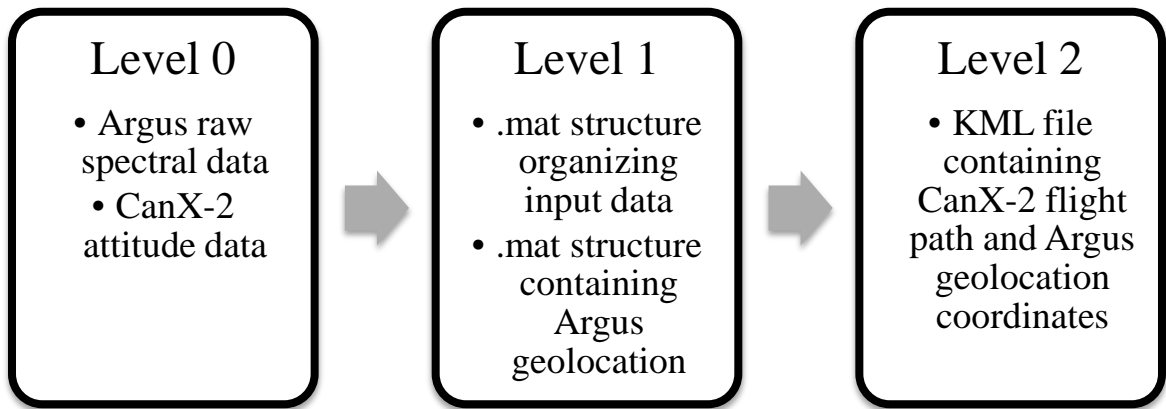


Figure 3-2 Levels of processing of automated geolocation

As shown in Figure 3-2, the data provided by the CanX-2 operations team, i.e. the raw spectral data and CanX-2 attitude data are referred to as Level 0 data. Level 0 represents unprocessed data that must be combined with external sources of data, such as spacecraft position data, to provide the necessary geolocation data. The geolocation data produced by the software is called Level 1 data and is stored as a MATLAB structure for use in subsequent data analysis. Lastly, the subsatellite flight path and instrument boresight geolocation coordinates are also written in Key Markup Language (KML) file format, which allows it to be integrated into external geographic software for display and is therefore called Level 2 data.

This form of classification is standard in EO space missions. For example, RADARSAT-1 data products are also classified based on three processing levels, as shown in Figure 3-3.

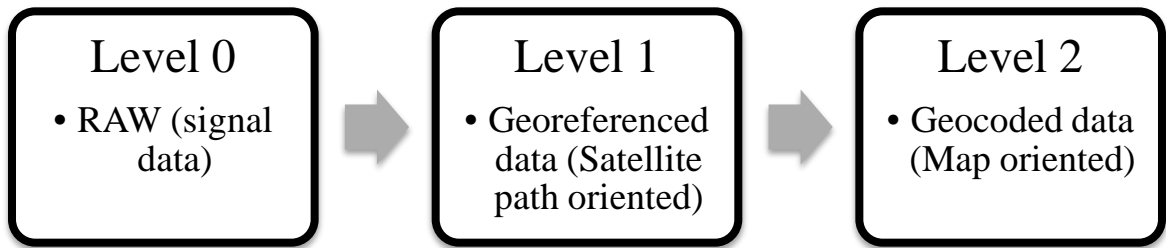


Figure 3-3 RADARSAT-1 Data Products (adapted from [55])

More generally, NASA defines a five level scheme for its EO data products [56]. Levels 0 to 2 are similar in processing to those of RADARSAT-1 and Argus 1000, while level 3 and 4 include outputs from further analysis.

The automation of Argus geolocation relies on several inputs given by the user, related to the storage of Argus spectral data. These inputs are the directory containing Argus data sets, the directory containing Argus mission request files, the directories in which external TLE and EOP files are to be stored, and the file paths of the background and calibration files used for instrument calibration. With these parameters known, the geolocation of Argus data begins with an initial processing of the level 0 data into a MATLAB structure called `inputData`. This structure contains all the level 0 data, organized into matrices for easy use, along with file paths to the original level 0 data files for reference. The `inputData` structure also verifies that all the level 0 data files have the necessary information for geolocation and contains a status variable to be checked before geolocation can continue.

Level 1 data are then generated using the geolocation algorithm shown in Figure 3-1, with the three highlighted input blocks processed automatically as shown in Figure 3-4.

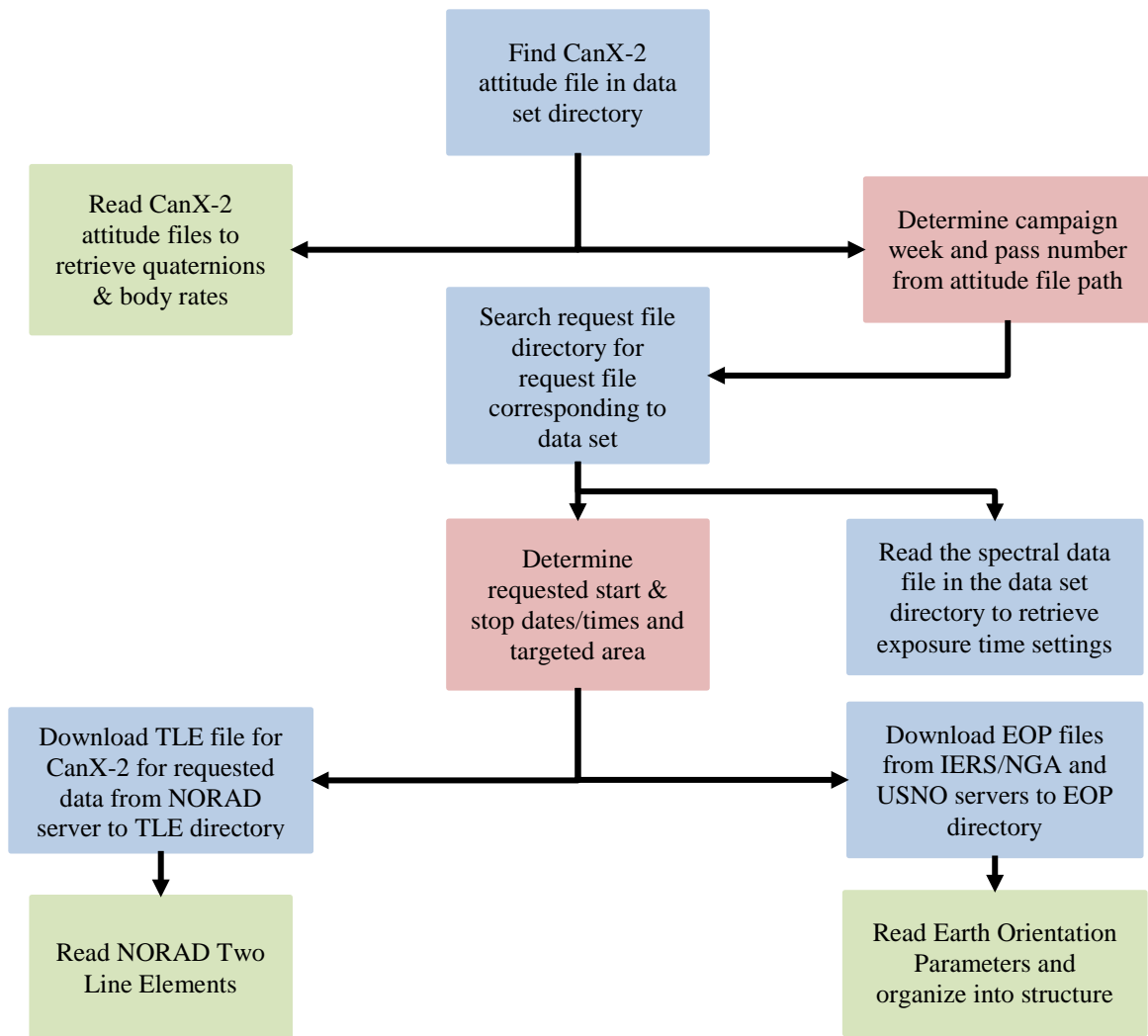


Figure 3-4 Block diagram of automated acquisition and processing of Level 0 parameters for spaceborne Argus data sets

The red and blue blocks in Figure 3-4 are respectively the key parameters and automated processes used to generate the inputData structure and verify that Level 1 geolocation can occur. Determination of the data acquisition times for each data set is a critical component of the geolocation process, as the data acquisition time is required for determining the spacecraft attitude and position for geolocation of each spectral measurement. Ambiguities

in the data acquisition time, either due to overlaps in the data request times or mismatches between the requested times and attitude file time stamps, are the principal source of automated geolocation failure. Another source of failure is a failure to download and acquire NORAD TLE data from the date of data acquisition, as the spacecraft position errors grow significantly (from 1 km at epoch to as high as 30 km) if TLEs older than 24 hours are used to propagate satellite position [57]. Missing or empty attitude files are an additional source of automated geolocation failure that are searched for and when found, do not allow the process to continue. Ultimately, if the data set passes all error checking, successful automation of the acquisition of the input parameters for achieving Level 1 processing results in the green blocks shown in Figure 3-4, containing organized substructures of the TLE, EOP, and spacecraft attitude data.

Acquisition of NORAD TLEs involves automatically downloading TLEs from the NORAD server. This is accomplished by querying the server through Uniform Resource Locators (URLs) constructed using Representational State Transfer (REST) logic. This process involves concatenating a series of strings into a URL that consist of a command to the NORAD server for a request for a particular TLE, i.e. the TLE for the date of acquisition of the data set.

In order to properly compute coordinate transformations of the spacecraft position and attitude data, EOP files are downloaded by the automated geolocation algorithm from the International Earth Orientation and Reference Systems Service (IERS) or from the National Geospatial Intelligence Agency (NGA) if IERS data are unavailable. EOPs from the IERS

are preferred as they include Earth nutation corrections, which are unavailable from NGA. Additionally, the EOP data associated with temporal corrections due to the addition of leap seconds is downloaded from the U.S. Naval Observatory (USNO) server. EOPs are then processed for any required coordinate transformations.

When applied to the Argus data, the automated geolocation algorithm successfully geolocated 270 data sets out of the 343 total data sets acquired from 2009 to 2016, a 79% success rate. The principal failures in geolocating the remaining data sets occurred due to ambiguities in the data acquisition time, a failure that would still occur if using the semi-automated algorithm.

3.2 Argus Geolocation Error Analysis

Geolocation error of spaceborne EO data is a mission requirement of EO space missions that is of great importance to data users as it establishes the level at which the analysis of the data yields useful results. The geolocation error is typically broken up into three general categories, consisting of spacecraft position errors, spacecraft attitude errors, and other errors [58]. Each source of error affects the geolocation error in different directions and is typically broken down into along-track and cross-track components for each EO measurement.

Spacecraft position errors consist of errors in the along-track of the orbit, defined as direction of the spacecraft's velocity vector, the cross-track of the orbit, defined as the direction normal to the orbit plane, and in the radial (or nadir) direction, defined as the direction toward the centre of Earth.

Spacecraft attitude errors are usually the largest sources of geolocation error and arise due to errors in attitude control, attitude determination, and reference frame errors in mounting the instrument on the spacecraft bus. For an EO instrument, they are often broken down into nadir angle errors (or elevation errors), defined as the error in angle between the instrument boresight axis and nadir, and azimuth angle errors, defined as errors in rotation of the instrument about the boresight axis.

Other sources of error include target altitude errors, which arise if the EO instrument is imaging an object on the surface of Earth, and spacecraft clock errors, defined as the uncertainty in the observation time of a measurement and result in errors in the equatorial direction due to Earth's rotation.

An analysis of the geolocation uncertainty for Argus 1000 data aboard CanX-2 is described in detail in [59] and [28]. The 1σ geolocation uncertainty of Argus data sets in the along-track and cross-track direction was determined to be 12.93 km and 10.95 km respectively.

3.3 Validation of Data Integrity

An important factor that requires attention in the automated processing of large quantities of spectral data is data integrity, defined as the completeness of each data set. In order for geolocation of spectral data to be of scientific value, data quality must be analyzed and properly characterized by the automated geolocation algorithm. For nanosatellite payloads such as Argus 1000, onboard timing errors are the largest contributors to geolocation uncertainty, though other sources of errors such as a lack of a TLE on the date of data acquisition and errors in the attitude quaternions or body rates also occur. For this reason,

an analysis of all the Argus data sets acquired in the CanX-2 nanosatellite mission was undertaken to confirm that the total time of the instrument data acquired matched the total requested time allocated by the spacecraft to the instrument. For each Argus data set, the duration of the i^{th} spectral packet is determined according to the equation [60]

$$\Delta t_i = \Delta t_{e,i} n_{s,i} + \Delta t_p \quad (1)$$

Where Δt_i is the total duration of the i^{th} spectral packet, $\Delta t_{e,i}$ is the exposure time setting of the instrument during the acquisition of the i^{th} packet, $n_{s,i}$ is the number of co-added scans during the acquisition of the i^{th} packet, and Δt_p is the instrument packetization time constant of 100ms [60]. The total observation duration for each data set is calculated by

$$\Delta t^c = \sum_{i=1}^n \Delta t_i \quad (2)$$

Where n is the total number of packets in the data set and Δt^c is the calculated total duration of the data set. An analysis of twenty-six data sets was undertaken, in which the observation duration for each data set was compared to the requested duration for each data set. These values were expected to be equal as the satellite operations team had submitted the requested durations as commands to the instrument aboard the spacecraft. The results of the comparison are shown in Table 3-1.

Table 3-1 Comparison of actual duration and requested duration of 26 Argus data sets

Week	Pass	Total Packets	Requested Duration [s]	Actual Packet Duration [s]	Difference in Duration [s]	Percentage Difference [%]
1	56	158	271.00	266.12	4.77	1.76
8	20	1961	329.00	211.78	117.11	35.60
8	46	1961	329.00	211.78	117.11	35.60
8	69	312	334.00	338.48	-4.59	-1.37
9	13	170	172.00	178.87	-6.98	-4.06
9	21	304	327.00	329.48	-2.60	-0.80
9	36	69	153.00	146.06	4.79	3.13
10	24	75	137.00	136.60	0.28	0.21
10	34	1962	327.00	227.48	99.41	30.40
10	40	166	335.00	332.07	2.82	0.84
10	52	166	329.00	332.07	-3.18	-0.97
10	64	161	328.00	323.36	4.52	1.38
10	69	89	139.00	166.67	-27.79	-19.99
11	12	165	331.00	329.92	0.96	0.29
11	40	52	137.00	136.48	0.41	0.30
11	60	90	332.00	328.56	3.32	1.00
13	26	318	337.00	352.39	-15.50	-4.60
13	40	157	134.00	171.42	-37.54	-28.01
13	46	310	330.00	343.40	-13.51	-4.09
13	69	141	145.00	153.44	-8.56	-5.90
14	10	125	130.00	135.46	-5.57	-4.29
14	60	320	328.00	346.57	-18.69	-5.70
14	67	311	326.00	344.52	-18.64	-5.72
15	10	122	123.00	132.08	-9.20	-7.48
15	30	309	329.00	342.27	-13.39	-4.07
15	40	317	335.00	351.26	-16.38	-4.89

As shown in Table 3-1, significant differences are present between the requested duration and the actual duration of each data set, with some data sets being shorter in duration than requested and others longer than requested in duration. Two approaches were undertaken

in order to find the source of these timing errors. In the first approach, the flight spare model of the Argus 1000 spectrometer was set up for data acquisition. At each exposure time setting, three sets of data were acquired, each of them for one minute. The average number of bytes acquired at each integration time setting and the average length of time for each set of measurements for a scan count setting of one are shown in Figure 3-5, with the raw data for each trial of the experiment shown in A-1.

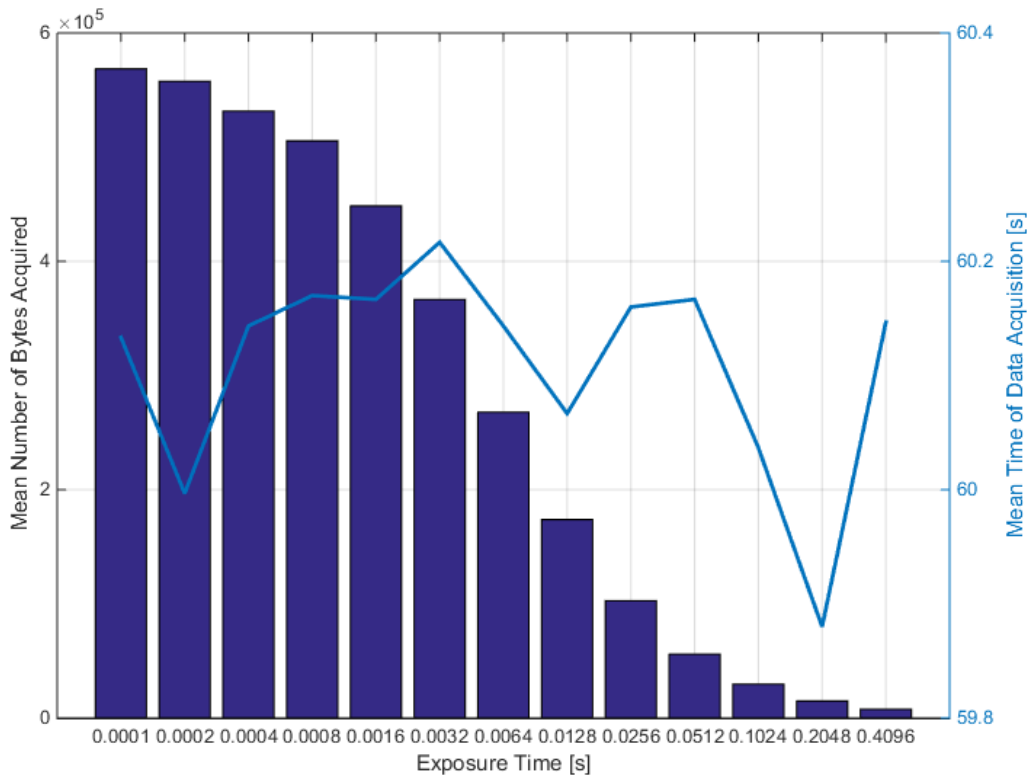


Figure 3-5 Number of bytes acquired and duration of flight spare Argus data sets at varying exposure time settings for a scan count setting of 1

The bars in Figure 3-5 show that the number of bytes acquired at high exposure time settings is much smaller than at lower exposure time settings, while the blue line shows

that there was little variation in the total acquisition time during the data acquisition. Conversion of the number of bytes acquired to number of packets and normalizing for the exposure time is required to compare different settings. In order to do so, for each exposure time setting, the average time per packet was computed and divided by the exposure time setting, as it was expected that doubling of the exposure time setting would double the number of packets acquired by the instrument. The calculated average packet times per exposure times for a scan count setting of one are shown in A-2 and were found to vary for the flight spare, potentially indicating errors in the known exposure time settings of the instrument. The distribution of the ratio of the average time per packet to the exposure time across the various exposure time settings is shown in Figure 3-6.

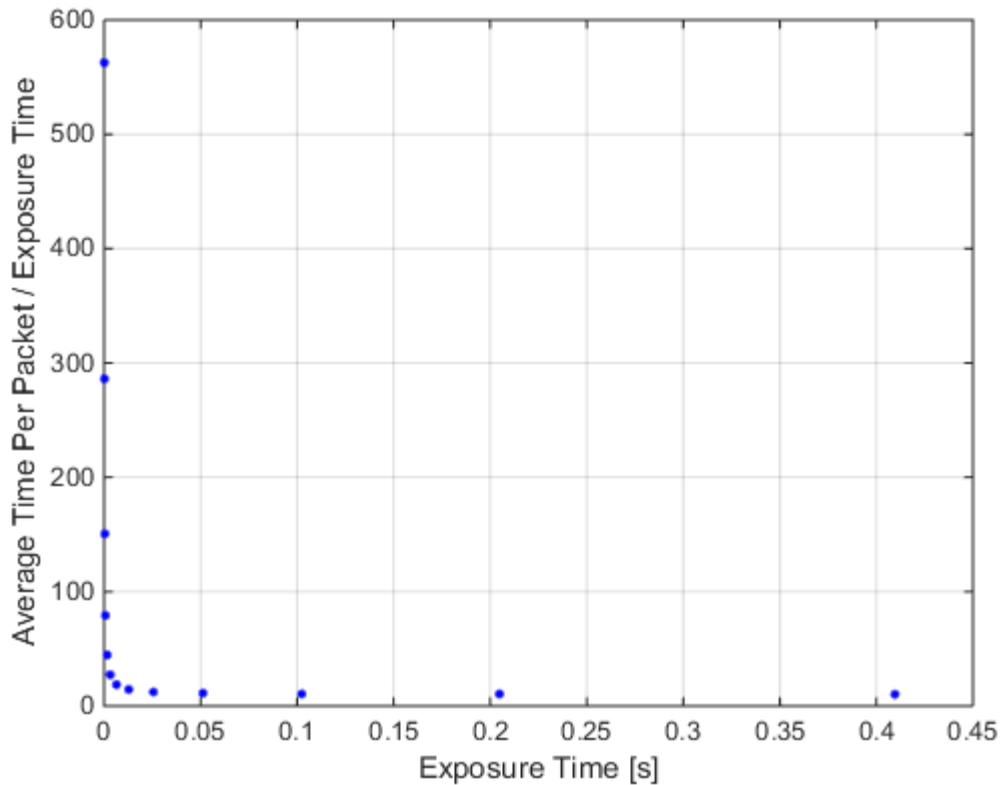


Figure 3-6 Scatter plot of ratio of the average time per packet to exposure time vs exposure time setting for a scan count setting of 1

Figure 3-6 shows that the ratio of the average time per packet to the exposure time setting decreases rapidly until an exposure time setting of 6.40×10^{-3} s is used, after which the rate of change slows considerably. The experiment was repeated for the same exposure time settings, however with a scan count setting of two in order to determine whether the scan count setting also affected the instrument timing as per the user manual algorithm. The average number of bytes acquired at each exposure time setting and the average length of time for each set of measurements for a scan count setting of two is shown in Figure 3-7, with the raw data for each trial shown in A-3.

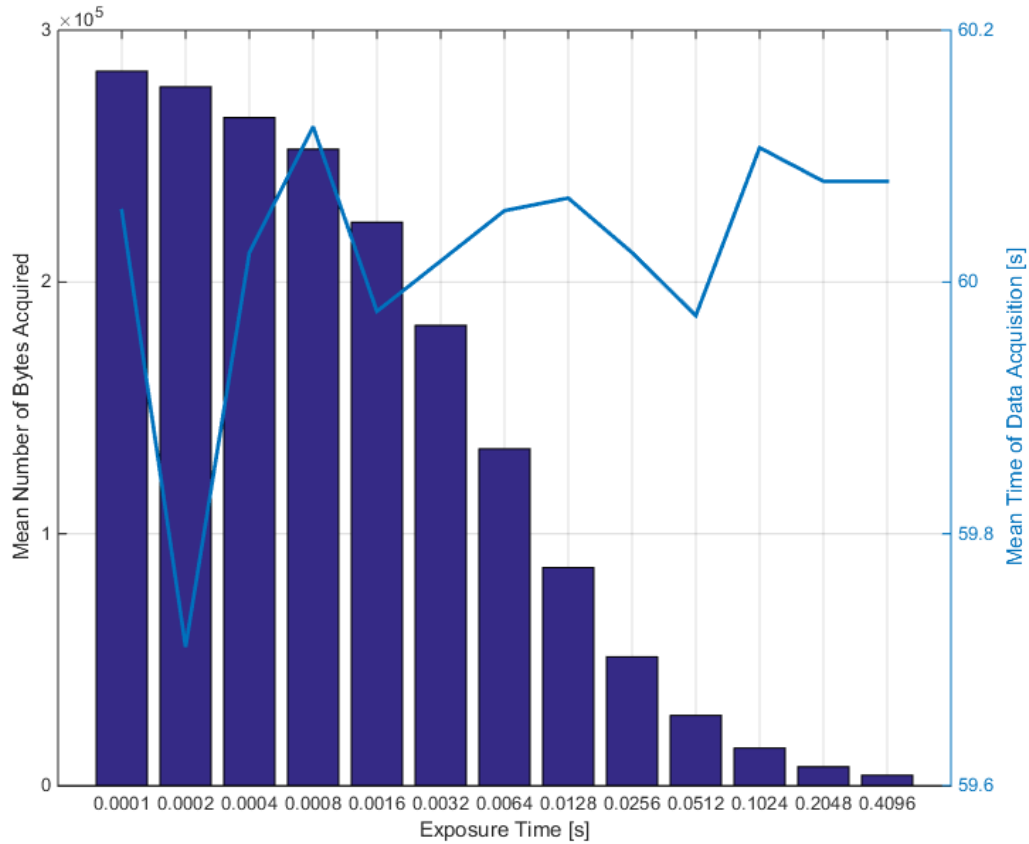


Figure 3-7 Number of bytes acquired and duration of flight spare Argus data sets at varying exposure time settings for a scan count setting of 2

As in Figure 3-5, Figure 3-7 shows a substantial drop in the number of bytes of data acquired as the exposure time setting is increased. The average time per packet was computed and divided by the exposure time setting, with the raw data and results shown in A-4. The distribution of the ratio of the average time per packet to the exposure time over the various exposure time setting for a scan count setting of 2 is shown in Figure 3-8.

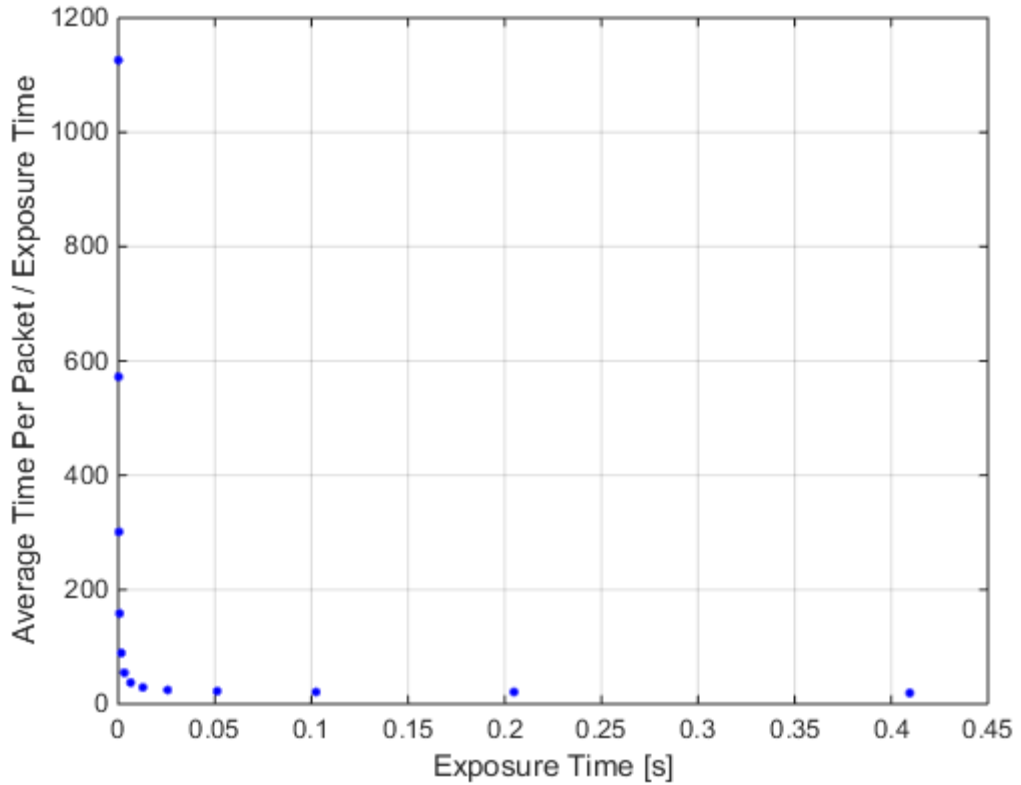
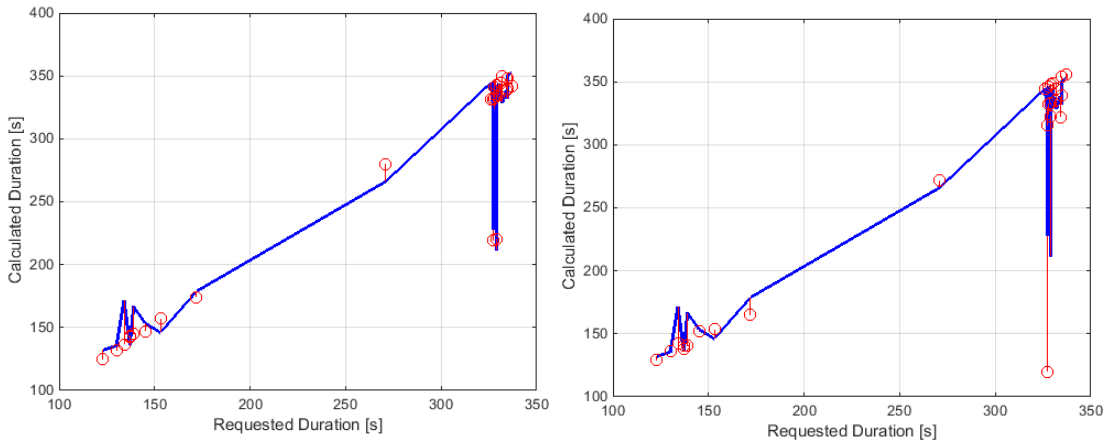


Figure 3-8 Scatter plot of measured time per packet vs exposure time setting for a scan count setting of 2

Figure 3-8 shows a similar drop off as Figure 3-6, though with different times per packet. Since the flight instrument experiment failed to provide a solution to the problem, a second approach was taken to determine whether an error is present in the known values for the exposure time values or the instrument packetization time value. In this approach, a least squares algorithm was applied to the calculation of the exposure time settings, packetization time, and number of scan counts setting under a series of restrictions. The least squares approach as applied to the data using the following cases:

1. $\Delta t_{e,i}$ and Δt_p were calculated as per the user manual algorithm described previously and in [60]
2. Δt_p was set to vary according to $n_{s,i}$
3. Fitting to $\Delta t_{e,i}$ only
4. Fitting to Δt_p only
5. Data set times were calculated as per the user manual algorithm in [60] with large outliers removed
6. Data set times were calculated as per the user manual algorithm in [60] on a subset of the data sets with $\Delta t_{e,i} = 1.024$ s and $n_{s,i} = 1$

These cases were selected in order to determine whether any one of the three settings, in particular, was causing the timing issues in the data sets. The residuals of the least squares fitting to the data sets analyzed for timing accuracy are shown in Figure 3-9, with the full data shown in Appendix B.



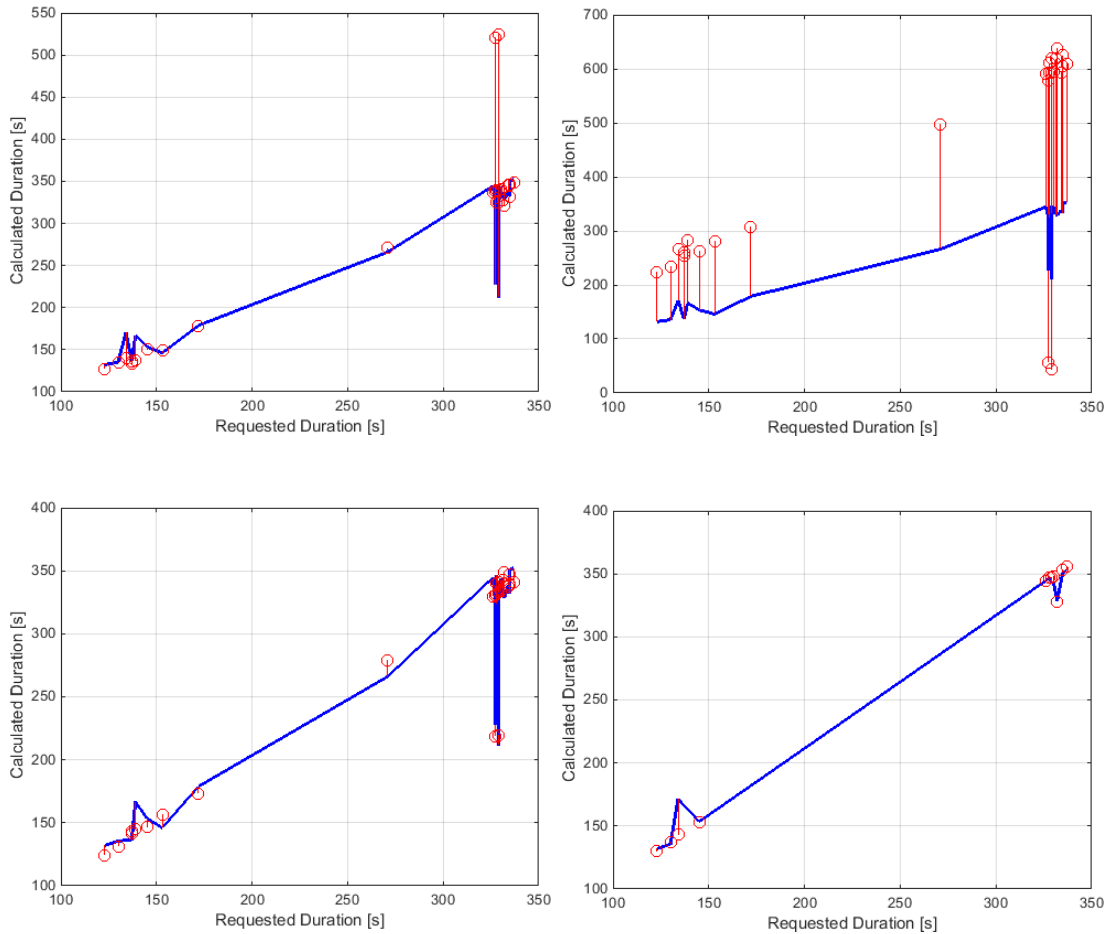


Figure 3-9 Least squares residuals of scaling factors to Argus data set exposure time and duration calculations: case 1 on top left, case 2 on top right, case 3 on middle left, case 4 on middle right, case 5 on lower left, and case 6 on lower right

Figure 3-9 shows that the residuals for fitting only to exposure time (case 3) or packetization time (case 4) result in the largest residuals. Case 2, which adds an effect of the number of scans setting to the packetization time, also contains a large outlier. In order to fully compare the results of all cases, the norm of the residuals for each case were plotted, as shown in Figure 3-10.

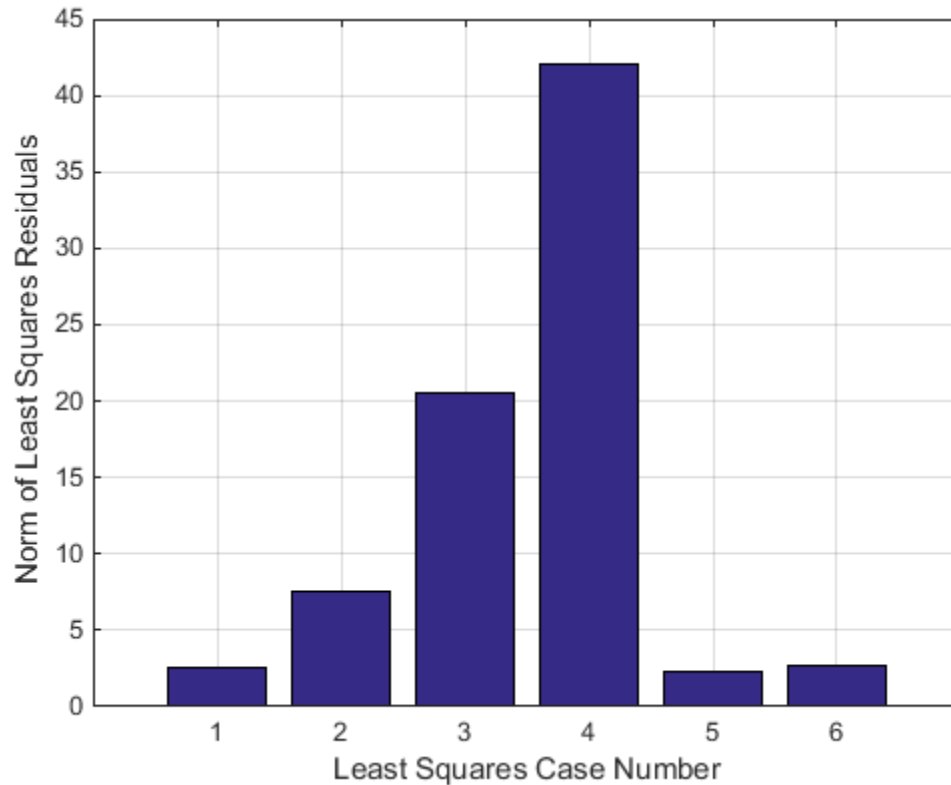


Figure 3-10 Norm of least squares residuals of scaling factors to Argus data set exposure time and duration calculations for six cases

As shown in Figure 3-10, the residuals of the least squares fitting were found to be smallest in the first and fifth cases. In these cases, the Argus user manual algorithm for calculating the duration of a packet was used, but in the fifth case the largest outlier in the data set was removed to see its effect on the least squares fitting. The least squares algorithm calculated scaling factors for the packetization time and the exposure time settings that would best reduce the duration differences. The results still showed a 2.3 s difference in duration remaining in the best of the least squares solutions, a value equivalent to 17.2 km in geolocation error.

A third and final approach was taken in order to resolve the timing issue. In this approach, all the Argus data sets acquired undergo preliminary processing prior to geolocation in order to compute a quality factor for assessing the timing of the data set. In this processing, the requested data set duration and actual duration are calculated for each data set, followed by the difference in duration for each data set. The percentage difference in duration is calculated as a percentage of the requested duration, since the length of the data sets range from 2 s to 5 s in size. For the j^{th} data set in a series of N data sets, the percentage difference in duration is given by

$$\Delta t_j^{diff\%} = \frac{\Delta t_j^c - \Delta t_j^r}{\Delta t_j^r} \quad (3)$$

Where Δt_j^c is the calculated duration of the j^{th} data set, Δt_j^r is the requested duration of the j^{th} data set, and $\Delta t_j^{diff\%}$ is the percentage difference in duration. The percentage difference is a negative value for data sets shorter in duration than the requested duration and positive for those longer in duration than the requested duration. From the percentage difference in duration of all the data sets, the timing quality factor is determined by quantifying the mean error in the percentage difference in duration. This is done using two metrics, the root mean square error (RMSE) and the mean absolute error (MAE). The RMSE of the percentage difference in duration of all N data sets is calculated by

$$\Delta t_{RMSE} = \sqrt{\frac{\sum_{j=1}^N (\Delta t_j^{diff\%})^2}{N}} \quad (4)$$

The MAE of the percentage difference in duration of all N data sets is calculated by

$$\Delta t_{MAE} = \frac{\sum_{j=1}^N |\Delta t_j^{diff\%}|}{N} \quad (5)$$

Each of these metrics is used to assess the quality of the timing for each data set. The RMSE is a larger value than the MAE, since the squaring operation increases the effect of outliers on its value. The final computation of the timing quality factor uses the metric chosen by the user in the input parameters to geolocation. The quality of the timing of each data set is determined by looking at how close the percentage difference in duration of each data set is to the RMSE and MAE. First, outliers are identified and removed from the data for computing the timing quality factor. An outlier is defined as any percentage difference in duration that is at least four times greater than the RMSE or MAE. Next, the corrected RMSE and MAE values are calculated for the non-outlier data sets. The timing quality factor is then defined as a discrete value that depends on the distance of the percentage difference in duration from the corrected values of the RMSE or MAE. For the case of the corrected RMSE, the timing quality factor for the j^{th} data set is defined as

$$QF_j = \begin{cases} 1, & \Delta t_j^{diff\%} \leq \Delta t_{RMSE}^c \\ 0.75, & \Delta t_{RMSE}^c < \Delta t_j^{diff\%} \leq 2\Delta t_{RMSE}^c \\ 0.5, & 2\Delta t_{RMSE}^c < \Delta t_j^{diff\%} \leq 3\Delta t_{RMSE}^c \\ 0.25, & 3\Delta t_{RMSE}^c < \Delta t_j^{diff\%} \leq 4\Delta t_{RMSE}^c \\ 0, & \Delta t_j^{diff\%} \geq 4\Delta t_{RMSE}^c \end{cases} \quad (6)$$

Where Δt_{RMSE}^c is the RMSE for the non-outlier data sets. The timing quality factor functions as a weighting factor that can be applied to data sets being analyzed to account for their timing errors. Five possible values were selected for the timing quality factor as a compromise between the need to remove large outliers and the need to conserve as much

data as possible. An analysis of 270 Argus data sets for data integrity was performed, with the timing quality factor computed for each data set. Δt_{RMSE} and Δt_{MAE} were found to be 16.9% and 8.10%, respectively, and once outliers were removed, Δt_{RMSE}^c and Δt_{MAE}^c were found to be 11.6% and 4.86%, respectively. With data acquisition limited to one data set per day for each data acquisition period, all data sets with timing errors greater than the RMSE or MAE are available for potential use.

In summary, the semi-automated geolocation algorithm for Argus data was converted to an automated system for generating Level 1 and Level 2 data from Level 0 data, with key input parameters such as TLEs and EOPs acquired as needed. Error checking was performed to ensure that the geolocation could be performed for each data set. The sources of geolocation error were analyzed and a timing quality factor was also developed to handle a persistent source of data integrity error. 270 data sets were successfully geolocated, with root mean square error of 11.6% found due to the timing error.

4 Validation of Geolocation Accuracy

Using a Coastline Detection Algorithm

Coastline detection, as described in 2.2, is an established method for validating the geolocation accuracy of spaceborne EO missions. The automated coastline detection algorithm developed for fixed, nadir pointing NIR spectrometers uses Argus 1000 data and an external source of coastline points to assess geolocation accuracy. Geolocation of Argus 1000 spectral data is accomplished using the geolocation algorithm described in [59], which determines the boresight path of Argus 1000 spectral data, consisting of a series of spectral measurements referred to as packets. Each packet is an exposure, which is separated from the previous and subsequent packets by a packetization time, as described in Chapter 3. The geolocation of Argus spectral data provides the geodetic coordinates of the boresight of Argus 1000 at the beginning and end time of the acquisition of each packet.

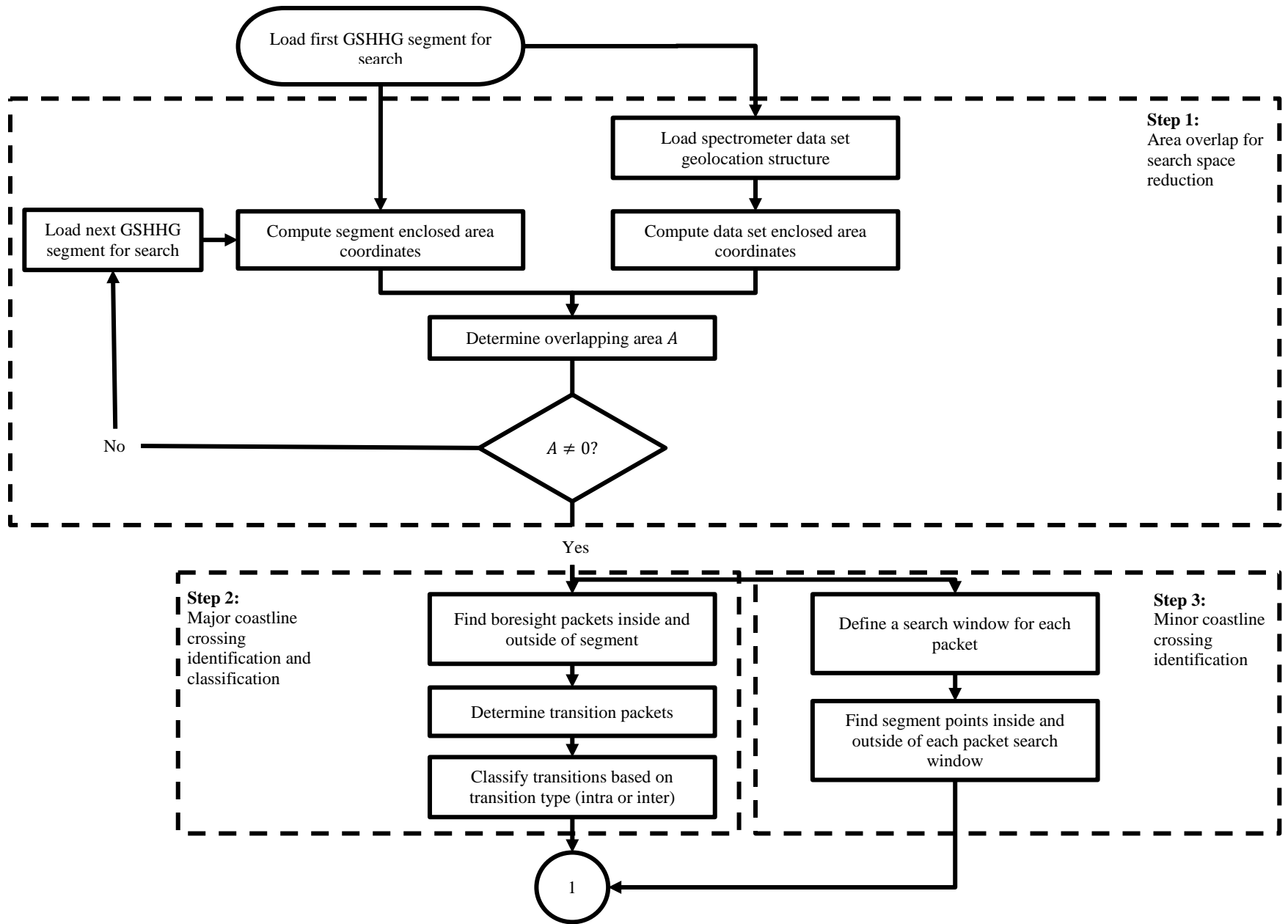
4.1 Implementation of Automated Coastline Detection Algorithm

The coastline detection algorithm consists of three stages, denoted as the search, detection, and analysis stages. The search stage uses the geolocation of the spectrometer data and an external coastline database to determine the coordinates of expected coastline crossings. The detection stage analyzes the spectrometer data itself in order to determine where

coastlines have been detected. The analysis stage then combines the results from the search and detection stages in order to determine geolocation error.

4.1.1 Coastline Crossing Search Algorithm

The automated coastline detection algorithm for Argus 1000 is designed to determine all the coastline crossings for any data set acquired. The automated algorithm uses NOAA's A Global Self-consistent, Hierarchical, High-resolution, Geography Database (GSHHG) of coastline points as the starting point for determining coastline crossings. GSHHG is a data set containing geographic coastline and political border information from two sources, NOAA's World Vector Shoreline (WVS), and the CIA's World Databank II (WDBII) [61]. With an scale of 1:250000, WVS provides geodetic coordinates of coastline points for oceans and lakes throughout the globe in the WGS84 reference frame, while WDBII provides coastline points for rivers and political borders. The coastline coordinates in GSHHG are divided into segments, each of which contains the coastline coordinates of a closed form, i.e. the first coordinate pair and the last coordinate pair of the segment are identical. Segments are also classified into levels, with lower levels indicating major coastlines and higher levels indicating smaller regions. An overview of the coastline crossing search algorithm is shown in Figure 4-1.



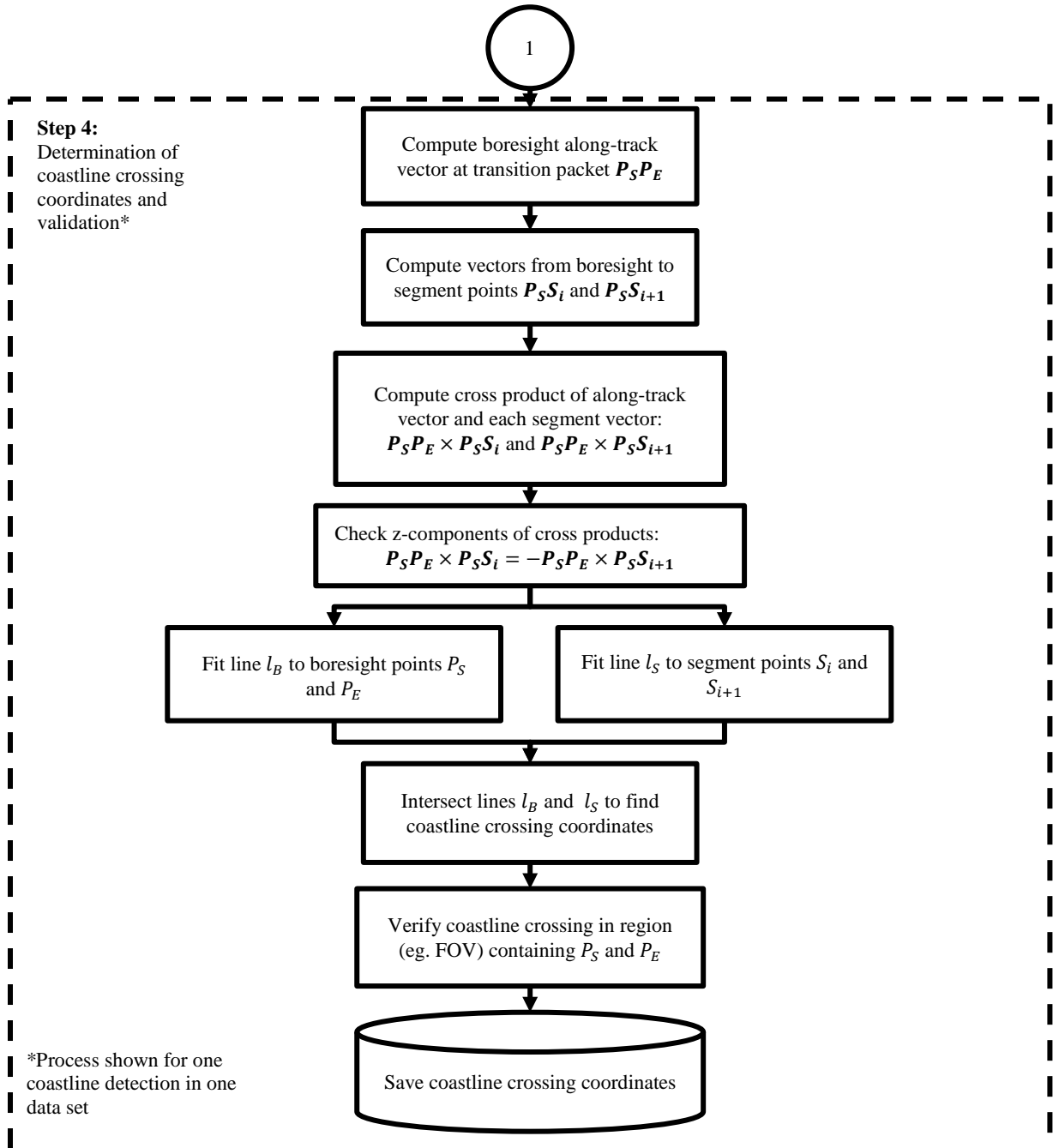


Figure 4-1 Coastline crossing search algorithm flow charts with steps 1-3 (top) connected to step 4 (bottom) by connector 1

The automated coastline search algorithm identifies which segments in GSHHG contain coastline crossings for a particular Argus 1000 dataset. This process, as shown in Figure 4-1, is accomplished in four steps. Step 1 is an initial calculation for search space reduction that serves to eliminate searching for coastlines in GSHHG segments that do not overlap with the geolocation of the data set. Step 2 is a process for finding clear changes between land and water regions, denoted as major coastline crossings, while Step 3 is a process for finding coastline crossings of regions located within the FOV of the instrument, denoted as minor coastline crossings. Step 4 completes the process by using the regions in the instrument geolocation and GSHHG segments from Steps 2 and 3 to determine the expected coastline crossing locations.

4.1.1.1 Search Space Reduction

Search space reduction is a process for improving the efficiency of the automated coastline crossing search algorithm by reducing the number of GSHHG segments that are searched for coastline crossings for each spectrometer data set being analyzed. This process is accomplished by determining the coordinates of a rectangle enclosing the boresight points of each data set. For each GSHHG segment analyzed, the coordinates of a rectangle enclosing the entire segment are also determined. Next, the area of intersection of the rectangles is determined using the MATLAB function `rectint()`, which takes as input the corner, width, and height of each rectangle and returns their area of intersection. If the area is non-zero, then the search algorithm is applied to the GSHHG segment as the regions overlap and may therefore include coastline crossings. If the rectangles have no area of intersection, the algorithm skips that segment and continues to the next one in GSHHG. A

visualization of the initial search is shown in Figure 4-2 for a data set acquired in the Vancouver area.

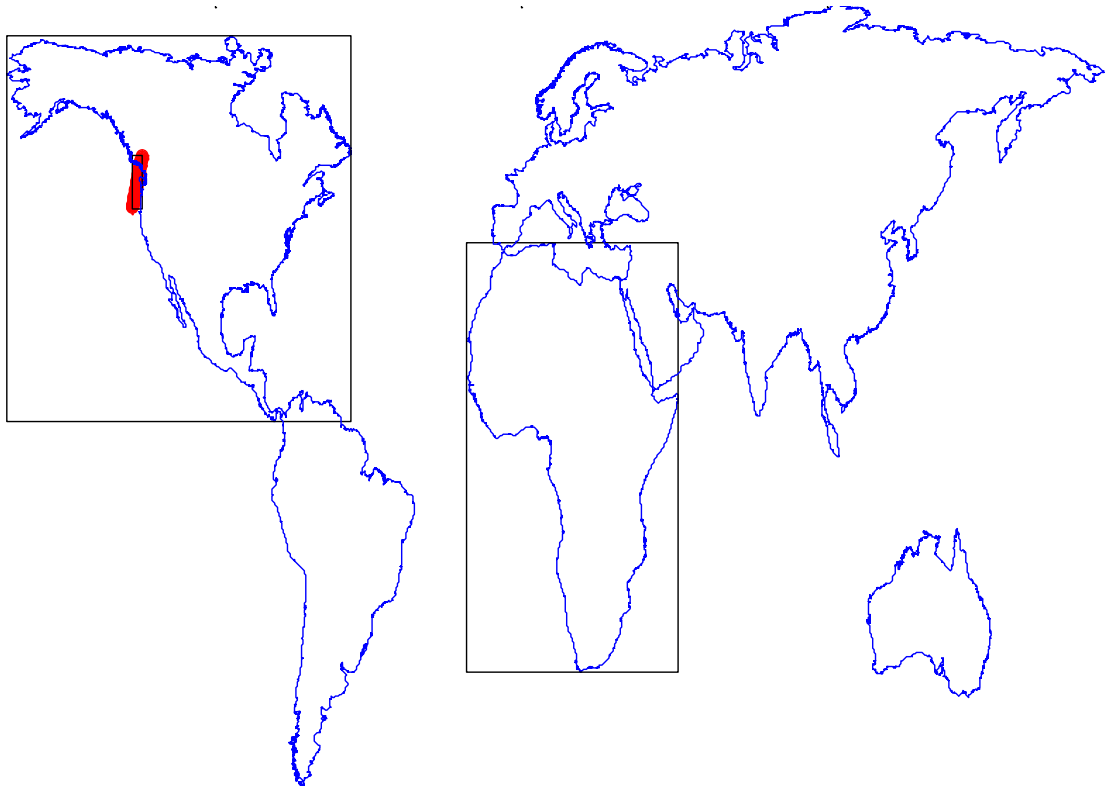


Figure 4-2 Visualization of the search space reduction concept for automated coastline identification, with several GSHHG polygon segments (blue), Argus boresight locations (red), and rectangular enclosing segments (black)

Figure 4-2 shows the geodetic coordinates of Argus boresight points in red for a data set acquired over the Vancouver area with a rectangular polygon enclosing the segment in black, along with two rectangular polygons enclosing the North American and African continental GSHHG segments as examples. These rectangular polygons are used in the initial search to identify which GSHHG polygons to search in further detail. Since there is

an overlapping area between the rectangle enclosing the Argus data set and the North American continental GSHHG polygon segment, that North American segment will be searched in further detail for a coastline crossing. For the African continental GSHHG segment, however, the area of intersection with the rectangular segment enclosing the Argus data set is zero, so further analysis of the African segment is skipped.

4.1.1.2 Major Coastline Crossing Identification

Major coastline crossings are sharp coastline crossings that are suitable for applying the coastline detection algorithm to the spectrometer data. These coastline crossings are defined as crossings that change the terrain observed by the spectrometer from one packet to the subsequent packet, either from land to ocean or vice versa. Minor coastline crossings, on the other hand, are defined as crossings that maintain the terrain observed by the spectrometer from one packet to the subsequent packet, as shown in Figure 4-3.

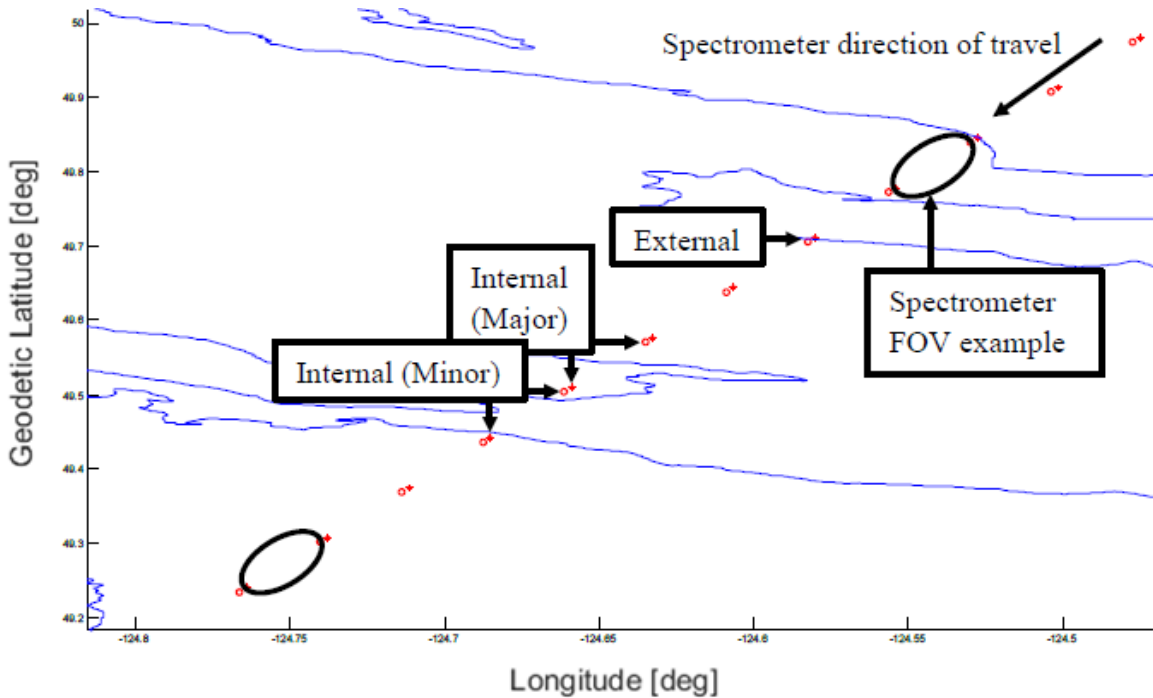


Figure 4-3 Classification concept of coastline crossings based on spectrometer boresight locations (red) and terrain changes, with GSHHG coastlines (blue) shown along with spectral start locations (circles) and spectral end locations (stars)

Figure 4-3 illustrates the classification of coastline crossings using an Argus data set acquired over Vancouver Island, with the instrument boresight locations shown in red and the GSHHG coastline segments shown in blue. The boresight locations themselves are shown for each packet in the data set at the start of data acquisition as circles and at the end of data acquisition as stars. Coastline crossings can be further divided into internal and external crossings. External coastline crossings are defined as crossings that occur between the end of one packet and the start of the subsequent packet and are therefore always major crossings, while internal crossings occur within a spectral packet and can therefore be either major crossings or minor crossings.

Each segment in GSHHG is treated as a polygon, in which the algorithm searches for points from the Argus boresight path, i.e. the start and stop points of each packet are tested to see if they are located in the polygon defined by the segments points in GSHHG. This computation is determined by calculating the winding number, which is defined as the integer number of revolutions made around the point being analyzed while traveling once around the polygon provided the point being analyzed is not done while visiting so [62]. Each pair of points from the boresight path is then checked for a transition across the segment polygon's boundary, i.e. a change from outside the polygon to inside the polygon or vice versa. Each transition that is found is then classified as either being a transition within a packet if the transition occurs between the coordinates of the start of packet and the coordinates of the stop of that packet, or as a transition between packets if the transition occurs between the coordinates of the stop of a packet and the coordinates of the start of the subsequent packet.

4.1.1.3 Minor Coastline Crossing Identification

Minor coastline crossings are typically present due to sections of large coastlines, islands, ponds, or rivers that are within the field of view of the instrument. Due to their size, they often do not provide a detectable signature in the spectral data and therefore cannot be used for coastline detection. Identifying these crossings is therefore important for the analysis stage of the coastline detection process, where coastline crossings are linked to detections in the spectral data. A similar search to the one described for identifying major coastline crossings is performed to find the minor coastline crossings in each packet. In conducting a search for minor coastline crossings, the algorithm defines a search region for each packet

consisting of the field of view of the instrument during the acquisition of the packet and a rectangular region formed by the geodetic coordinates of the end of the packet and the start of the subsequent packet for coastline crossings between packets. Each region is treated as a polygon in which a search is performed for points from each GSHHG segment that are located within the polygon, as shown in Figure 4-4.

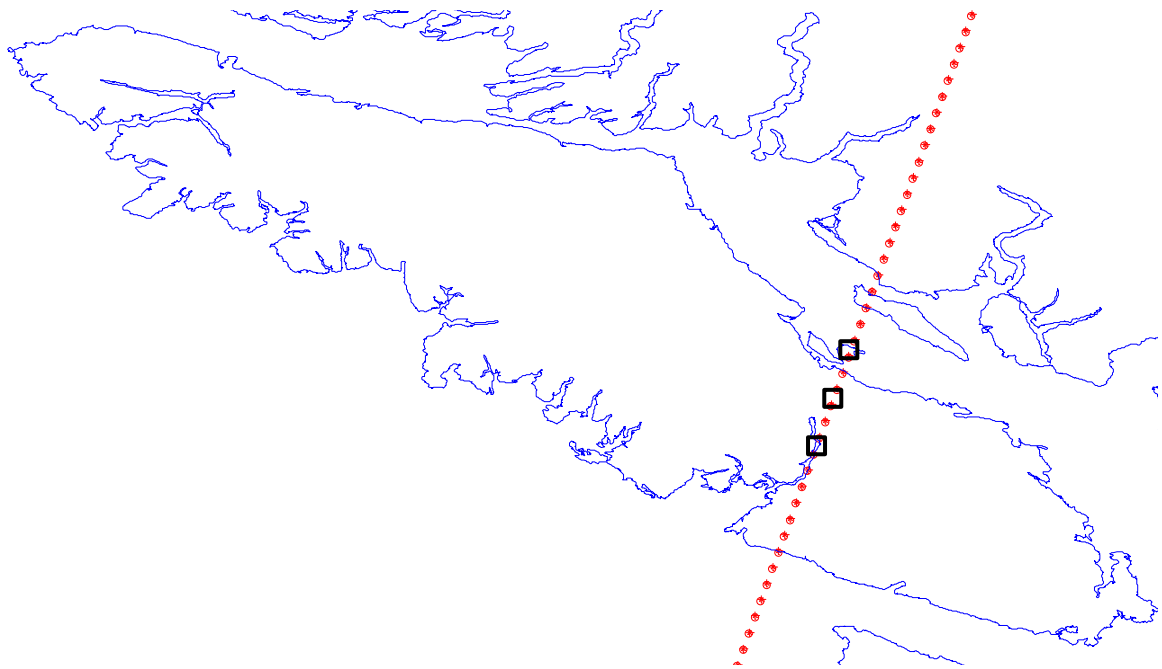


Figure 4-4 Visualization of minor coastline crossing search for Argus data set acquired over Vancouver area. Argus boresight packet locations (red), GSHHG segments (blue), and packet search regions (black) as shown.

Figure 4-4 shows the search for minor coastline crossings using rectangular search regions shown in black for an Argus data set acquired over the Vancouver area. The instrument travels from north to south, with a search window defined for each packet. Each packet search window is treated as a closed form polygon into which each GSHHG segment is

iteratively searched for transitions into and out of the polygon. These changes are used to determine the locations of minor coastline crossings.

4.1.1.4 Determination of Coastline Crossing Results

When computing the coordinates of the crossings themselves, the algorithm begins by computing the along track vector between each pair of points of the Argus boresight path at which polygon transitions have been previously found. The algorithm then iterates through the coordinates of each point in the segment at which the transitions have been found. It computes two vectors, the first from the boresight point at which the transition was found to the point in the segment at the current iteration step and another from the boresight point to the next point in the iteration. The cross products of the along-track vector and each of the position vectors is then determined. If the coastline crossing occurred at a point between the two subsequent points along the segment, the along-track vector will pass between those points and therefore the z-component of the cross product will change sign. Once the pair of points in the segment where the coastline crossing resides are found, the coordinates of the coastline are found by line intersection, i.e. a line joining the point pair in the segment l_S is intersected with a line joining the point pair in the boresight path l_B where the transition was detected. An illustration of this process is shown in Figure 4-5.

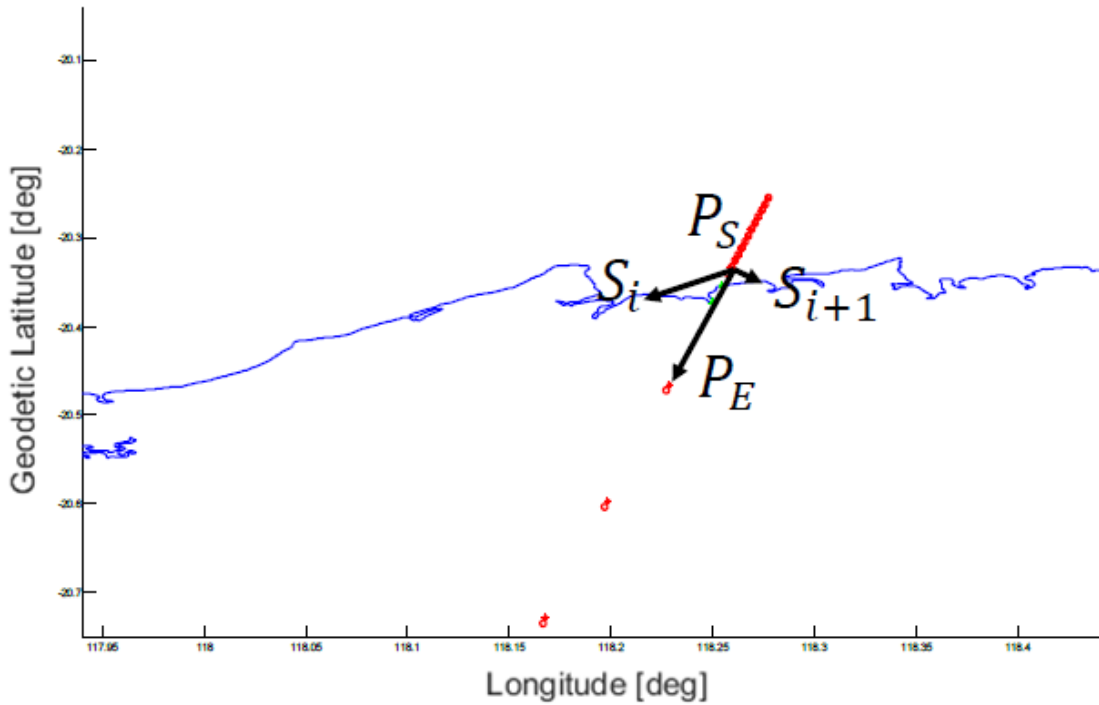


Figure 4-5 Illustration of the final iterative process for determining coastline locations with GSHHG coastline (blue), Argus boresight points (red), and calculated coastline crossings (green)

Figure 4-5 illustrates a snapshot of Step 4 in the coordinates of coastline crossing search algorithm for Argus data using GSHHG. Points P_S and P_E are the consecutive Argus boresight points, between which a coastline crossing is found to be present by the first steps of the algorithm, i.e. by determining that one of the points is located in the closed polygon segment and the other is not. The along-track vector $P_S P_E$ is determined, along with the vectors $P_S S_i$ and $P_S S_{i+1}$ to points in the GSHHG segment being analyzed at the current (i^{th}) and subsequent iterative steps. The cross-products $P_S P_E \times P_S S_i$ and $P_S P_E \times P_S S_{i+1}$ are determined, with a change in the sign of the z-component of the cross products used to indicate a coastline crossing across the along-track vector of the boresight path. Line l_B is

fitted to the points P_S and P_E and line l_S is fitted to the points S_i and S_{i+1} , after which they are intersected to determine the coastline crossing coordinates. These coordinates are then tested using the point in polygon algorithm to see if they are within a rectangular area consisting of P_S and P_E as its edges in order to ensure a real intersection.

4.1.2 Detection of Coastline Crossings in NIR Spectrometer Data

Detection of coastline crossings for spaceborne RO data is accomplished using one or more of the four methods described in 2.2. For the coastline detection algorithm developed for fixed nadir pointing, single-pixel NIR spectrometers, two detection methods are described.

4.1.2.1 Inflection Point Coastline Detection Method

The inflection point coastline detection method is an established method for identifying coastlines in radiometer data, in particular for push broom style scanning instruments such as ERBE and CALIPSO [29] [32]. This method involves iteratively searching radiometric measurements for coastlines by fitting a cubic polynomial to a set of four consecutive measurements, defined for Argus 1000 spectral packets as R_i , R_{i+1} , R_{i+2} , and R_{i+3} , where i ranges from 1 to $n - 3$. The value of i changes with each iteration of the detection algorithm, in effect sliding the cubic polynomial fit along each set of four successive measurements in the data set. Since each Argus data packet is a spectral radiance curve that is defined at each point on the instrument detector array corresponding to a particular wavelength, each value of R_i is obtained by numerically integrating the spectral radiance over the instrument wavelength range. The fitted polynomial maps the geolocation data of the measurements, such as geodetic latitude or longitude, to the radiance of the

measurement. A significant change in radiance is expected to occur as an instrument operating in the near infrared, such as Argus 1000, scans over coastal areas due to the extremely low albedo of water in this wavelength range compared to land. The inflection point I of the cubic polynomial is taken to be the location of the coastline in the spectrometer data, provided a series of conditions are met. First, the inflection point must be located between the second and third measurements in the set, i.e. $R_{i+1} < I < R_{i+2}$. Second, the absolute value of the difference in radiance between the first and fourth measurements in the set must be greater than a pre-defined threshold T , i.e. $|R_{i+3} - R_i| > T$. For Argus 1000 data, a threshold of $1 \text{ Wm}^{-2}\text{sr}^{-1}$ is used, as in the coastline detection algorithm implemented for ERBE [29].

4.1.2.2 Albedo Change Coastline Detection Method

An alternate technique developed for coastline detection analysis of NIR spectrometer data, such as Argus 1000, is the albedo change coastline method. This method involves using an external radiative transfer model to estimate the albedo of each packet in a data set since typical albedo values are known for both water and land. This process involves using a standard atmosphere and a radiative transfer model to generate synthetic spectra at a range of albedo values for each packet in the data set, i.e. the geolocation parameters of each packet are used to generate the synthetic spectra. The difference between the radiance spectrum of each packet and the synthetic radiance is calculated for each albedo value. The albedo value at each packet is taken as the one corresponding to the smallest mean difference between the synthetic and actual spectra. Successive pairs of radiance spectra are then searched for sharp albedo drops or increases using their determined albedo values,

which are used as coastline indicators. A minimum threshold value is used for accepting sufficient albedo changes as potential coastlines. In order to screen for false detections, a fitted albedo value below 10% must also occur for one of the packets where a sharp change in albedo is found. The detected coastline location is determined using a similar approach to the inflection point coastline detection method. A cubic polynomial is fitted to four successive albedo values, with the two middle values corresponding to the albedos at which a sharp change was detected.

The albedo change coastline detection algorithm was applied to all 270 Argus data sets using a radiative transfer model called GENSPECT to generate the synthetic spectra. Additionally, an albedo change threshold of 1% between successive packets was used in the algorithm. Unfortunately, coastlines were only detected in two data sets using this method, making it unsuitable for coastline detection analysis.

4.2 Analysis of Coastline Detection Algorithm Results

Regardless of the method used for detecting coastlines in the spectral data, the inflection point of a cubic polynomial is used to determine the relative location of the coastline along the Argus boresight path and linear interpolation is used to determine the detected coastline crossing coordinates from the geolocation data of the instrument. Next, the distance between the geographic location of the inflection point and the nearest coastline crossing along the instrument path is determined. The inflection point with minimum distance to the expected coastline crossing along the instrument path is used to select the location of the coastline in the spectral data to use for analysis, when multiple candidates are detected.

The angular change required to point the spacecraft from the geodetic coordinates of the inflection point to the location of the coastline crossing is determined. This angular change is a potential attitude error for the coastline crossing in the data set. This analysis is repeated for all the coastline crossings in the data set and subsequently for all the coastline crossings found in all the data sets. Additionally, an angular error range is calculated for each coastline crossing, based on the presence of a ± 1 s timing error in the data.

The automated coastline detection algorithm was applied to 270 Argus data sets, for which the geolocation process was successful. The data sets spanned five years of data acquisition campaigns conducted four times per year. Each campaign was one month long and consists of one data set per day over a region of interest, which may or may not contain coastline crossings. Applying the coastline detection algorithm using the inflection point method described in 4.1.2.1 for the spectral data analysis, resulted in 128 coastline crossing detections over 26 data sets, prior to any outlier detection, such as restrictions on the maximum accepted distance to a coastline.

Three restrictions were subsequently applied to the results of the coastline detection in order to remove outliers. First, only coastline detection results with angular errors less than an angle of 65.6° were accepted, as this angle represents the maximum angle from nadir to the Earth's horizon at the spacecraft height. Second, only data sets with a timing quality factor of 1 were used as these are of the highest data quality. Third, only coastline detections where the distance between the inflection point and the actual coastline crossing

was less than 40 km was accepted, as this distance is the 3σ geolocation uncertainty of the Argus boresight in the along-track direction at a nadir angle of 10° .

After applying the outlier detection restrictions, 55 coastline crossing detections remained, located over seven regions of interest, centred on Australia, Mumbai, the Pacific Ocean, Patagonia, Toronto, Vancouver, and Whitehorse as shown in Table 4-1.

Table 4-1 Coastline detection results summary table

Data Set ID	Crossing ID	Expected Crossing Coordinates [°]	Detected Crossing Coordinates [°]	Angular Error [°]	Crossing Angle [°]
W11P40	1A	(57.99, -134.03)	(58.03, -133.99)	0.02	59.14
W14P10	2A	(54.99, -131.72)	(55.2, -131.59)	0.45	84.88
	2B	(55.18, -131.6)	(55.33, -131.51)	0.30	31.52
	2C	(55.85, -131.2)	(55.95, -131.13)	0.17	85.77
W14P52	3B	(43.82, -77.84)	(44.03, -77.73)	1.24	39.68
	3E	(46.99, -76.39)	(47.12, -76.39)	0.73	52.14
	3F	(47.23, -76.39)	(47.44, -76.38)	1.51	61.89
	3G	(47.37, -76.39)	(47.44, -76.38)	0.08	61.89
	3H	(47.75, -76.38)	(47.84, -76.38)	0.30	74.27
W14P54	4C	(49.5, -124.49)	(49.63, -124.43)	0.52	23.12
	4D	(49.61, -124.44)	(49.72, -124.39)	0.45	66.67
	4E	(49.72, -124.4)	(49.77, -124.37)	0.01	67.35
W15P69	5B	(55.84, -134.31)	(55.91, -134.27)	0.05	33.05
	5C	(55.98, -134.23)	(56.06, -134.18)	0.09	58.76
	5D	(56.3, -134.03)	(56.52, -133.9)	0.56	84.93
	5E	(56.58, -133.87)	(56.59, -133.86)	0.14	59.35
	5F	(56.71, -133.79)	(56.85, -133.7)	0.33	30.67
	5G	(57.04, -133.57)	(57.16, -133.48)	0.29	80.88
	5H	(57.14, -133.49)	(57.29, -133.39)	0.38	53.80
W19P38	6E	(45.89, -80.33)	(46.23, -80.2)	2.97	62.77
	6F	(46.33, -80.16)	(46.26, -80.19)	1.32	62.53
W19P70	7B	(55.84, -133.65)	(55.97, -133.57)	0.35	56.95
	7C	(56.06, -133.52)	(56.16, -133.45)	0.23	58.11

Data Set ID	Crossing ID	Expected Crossing Coordinates [°]	Detected Crossing Coordinates [°]	Angular Error [°]	Crossing Angle [°]
	7D	(56.17, -133.44)	(56.33, -133.33)	0.49	81.91
	7E	(56.41, -133.28)	(56.46, -133.25)	0.01	79.45
	7F	(56.45, -133.25)	(56.63, -133.13)	0.58	81.65
	7G	(56.57, -133.17)	(56.66, -133.1)	0.20	81.73
	7H	(56.75, -133.04)	(56.87, -132.95)	0.35	39.80
	7I	(56.86, -132.97)	(56.96, -132.9)	0.25	54.97
	7J	(56.99, -132.87)	(57.08, -132.81)	0.19	56.92
W20P27	8B	(-10.78, 165.85)	(-10.67, 165.88)	0.01	56.59
W20P61	9A	(49.74, -119.67)	(49.65, -119.64)	0.38	15.11
W36P29	10A	(-33.88, 121.52)	(-33.83, 121.53)	0.00	76.66
W36P44	11A	(-35.12, 116.46)	(-35.01, 116.49)	0.05	61.00
W37P44	12A	(-29.07, 114.7)	(-28.97, 114.72)	0.23	59.51
W38P14	13A	(-33.58, 115.01)	(-33.58, 115.01)	0.08	56.50
W40P47	14A	(-28.78, 153.61)	(-28.72, 153.62)	0.06	79.09
W41P27	15B	(-49.53, -73.94)	(-49.52, -73.94)	0.06	74.00
	15D	(-48.24, -73.57)	(-48.14, -73.54)	0.06	15.87
	15G	(-40.95, -71.61)	(-40.87, -71.59)	0.15	85.29
	15H	(-40.73, -71.56)	(-40.61, -71.53)	0.38	89.87
W41P34	16B	(-17.53, 123.54)	(-17.38, 123.57)	0.73	54.76
	16D	(-16.24, 123.76)	(-16.12, 123.78)	0.58	54.76
W50P34	17A	(-34.46, 118.88)	(-34.46, 118.88)	0.02	74.93
W74P29	18B	(-17.24, 123.46)	(-17.35, 123.44)	1.75	78.80
W75P14	19B	(-18.65, 121.95)	(-18.4, 121.99)	1.97	79.50
W75P29	20A	(-31.3, 115.51)	(-31.35, 115.5)	0.22	78.86
W75P58	21A	(-31.62, 131.25)	(-31.5, 131.27)	0.02	78.84
W89P53	22A	(20.42, 58.72)	(20.26, 58.76)	0.02	58.81
W104P44	23A	(42.32, -80.02)	(42.19, -79.98)	0.70	87.23
	23B	(42.65, -80.15)	(42.54, -80.11)	0.46	76.38
	23C	(42.75, -80.18)	(42.57, -80.12)	1.09	49.89
	23F	(46.09, -81.56)	(46.01, -81.53)	0.15	80.11
	23G	(46.11, -81.57)	(46.03, -81.54)	0.11	81.55

The coastline detection results shown in Table 4-1 are organized by data set, with each data set identified by its observation week and pass number. The mean angular error from the

expected coastline crossing coordinates to the detected coastline crossing coordinates in the data sets was 0.44° , less than the CanX-2 attitude knowledge requirements of 1° . Additionally, the standard deviation of the angular errors was 0.57° , with the minimum angular error determined to be $3.0 \times 10^{-3}^\circ$ and the maximum angular error determined to be 2.97° . The final column in Table 4-1 is a calculation of the angle at which the spectrometer crossed the coastline. Coastline crossing angles near 90° were identified in order to determine whether the angular error to those coastlines was smaller than the remaining the data sets, possibly allowing along-track and cross-track components of the angular error to be determined, as shown in Figure 4-6.

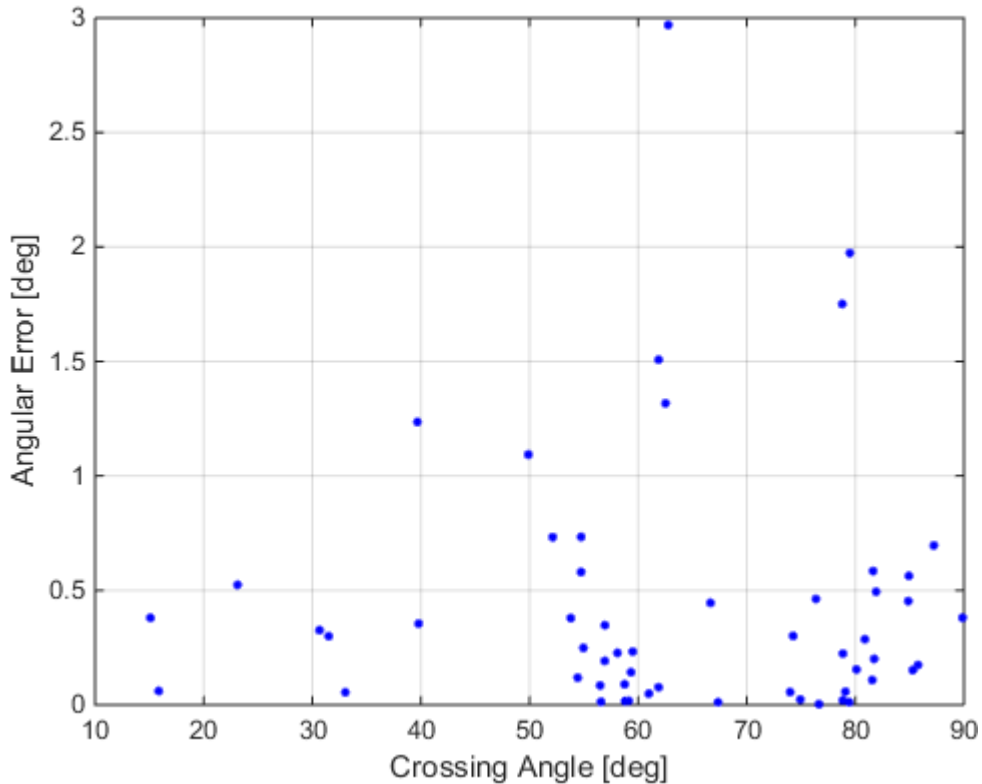


Figure 4-6 Angular error vs coastline crossing angle for Argus 1000 coastline detection results

The distribution of points in Figure 4-6 demonstrates a greater number of coastline detection at higher coastline crossing angles. However, no trend is observed in the data for angular error that would allow along-track and cross-track components to be identified from the coastline crossing angles.

The results span a range of six years, starting from November 18, 2009 and ending on April 9, 2015. Since some data sets have multiple coastline crossings, the 55 coastline detections are spread across 22 data sets. Calculating the angular error of each coastline detection and plotting the results over time produces the distribution shown in Figure 4-7.

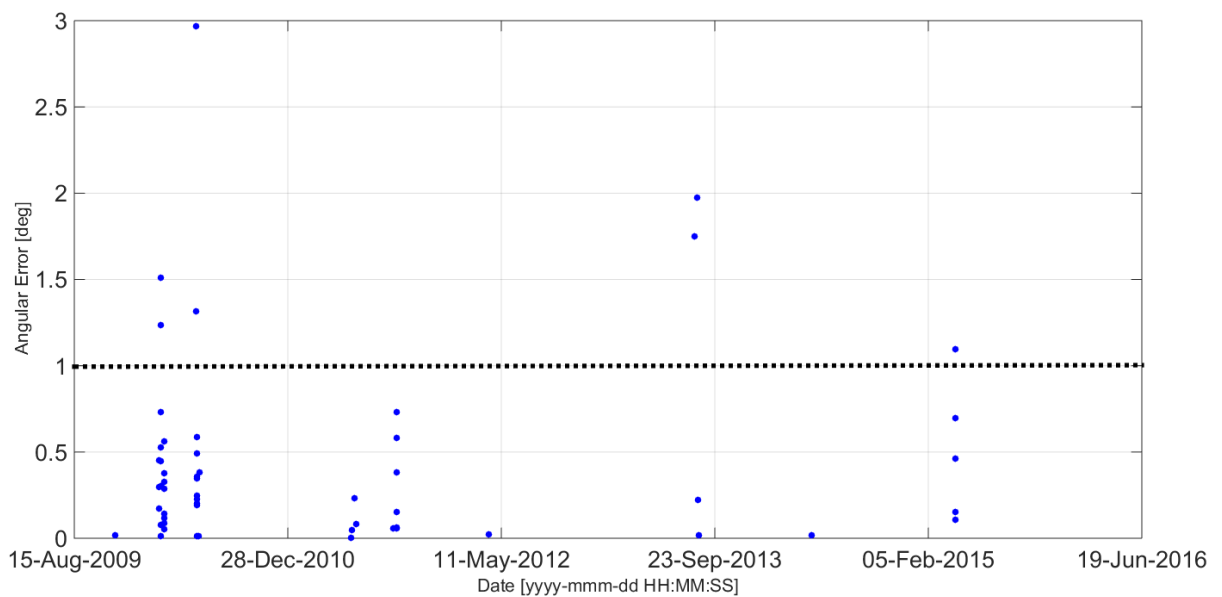
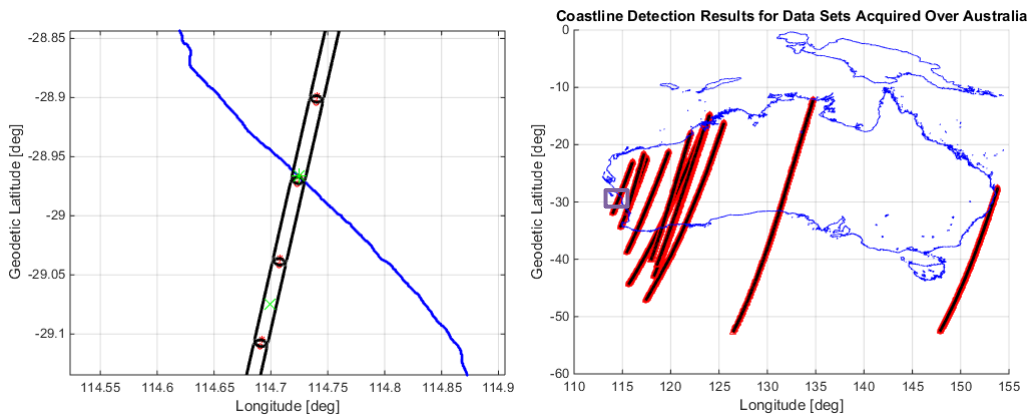


Figure 4-7 Angular error from expected location to detected location of coastlines over mission time with 1° (1σ) attitude knowledge requirement shown

Most of the coastline detections occurred for data sets acquired in 2010 and 2011, as can be seen in Figure 4-7. The presence of multiple coastline detections in some data sets is the cause of the apparent clustering of angular errors in the y-axis, along with the presence of

coastline detection results in several data sets acquired in the same observation campaign. Since the x-axis spans over six years, detections that occurred close to one another appear clustered together. There is no distribution to the coastline detection results with time, possibly indicating that the system is performing as expected throughout the lifetime of the mission. Additionally, only seven of the fifty-five angular error values are above the 1° (1σ) attitude knowledge uncertainty.

Furthermore, mapping the data sets containing the coastline detection results along with the GSHHG segments crossed in those data sets provides a method for analyzing the effectiveness of the algorithm. Figure 4-8 shows the data sets for which coastlines were detected and the GSHHG segments, each organized under the region of interest over which the data set was requested. The coordinates of the boresight of the instrument are shown in red and GSHHG coastline coordinates are in blue in all figures. In addition to the regions of interest, Figure 4-8 shows a visualization of a sample result, with the instrument field of view regions are outlined in black, the expected coastline crossing as a green star, and the detected coastline crossing coordinate as a green cross.



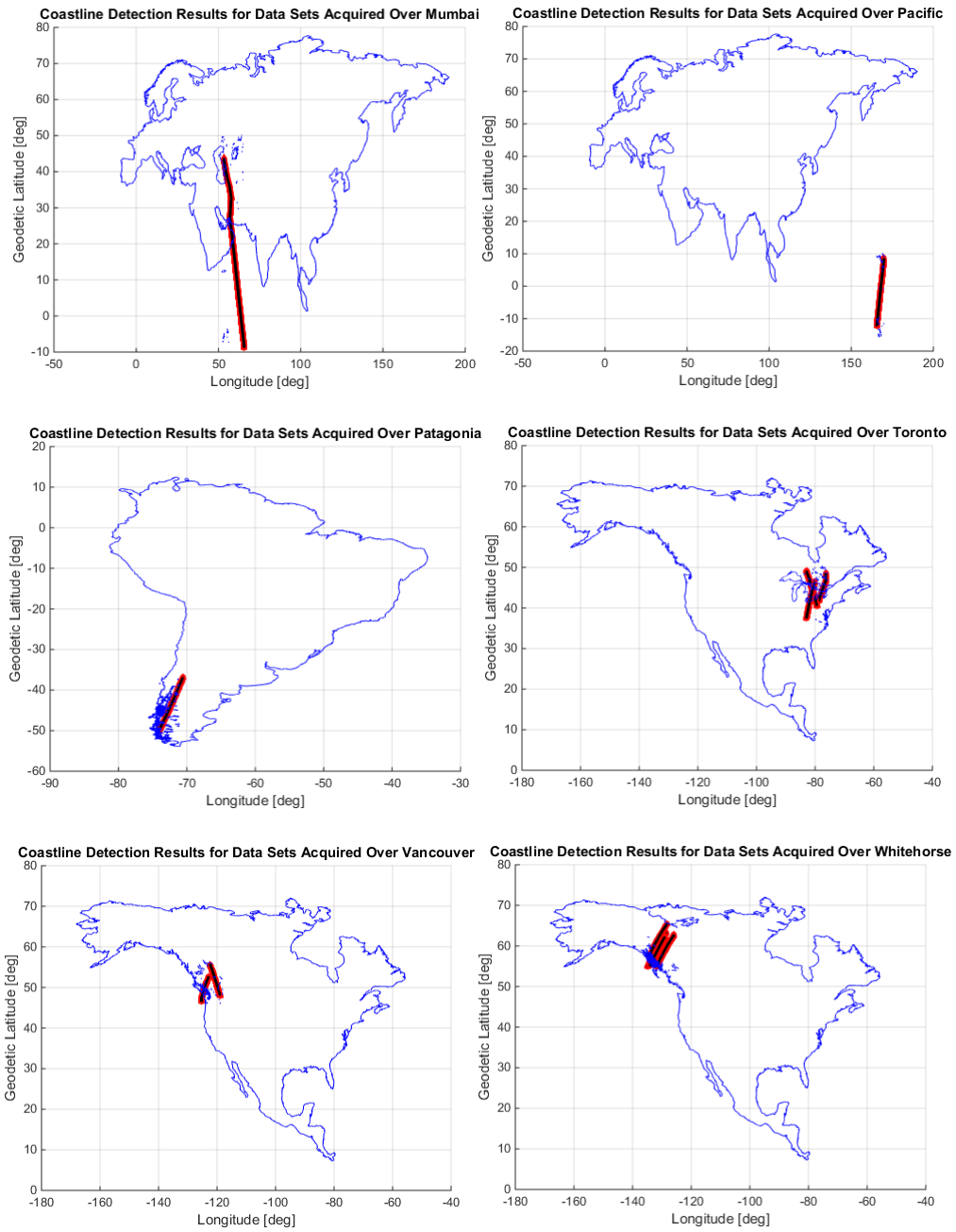


Figure 4-8 Illustrations of data sets containing coastline detections organized under mission defined regions of interest, with sample result shown (top left) for highlighted region (top right)

The geographic distribution of the results shows that the region of interest centered over Australia produced the most data sets with successful coastline detections and the Pacific Ocean and Mumbai regions resulted in the fewest. This result is consistent with the data sets used in [29], where the contrast between desert and ocean offered the best choice of location for coastline detection analysis.

The effect of the choice of the irradiance threshold T for the cubic polynomial edge points used in the coastline detection algorithm was also determined by applying the coastline detection algorithm to the data sets iteratively, with the minimum threshold for the change in irradiance between the first and fourth elements of the cubic polynomial increased at each iteration. The total number of coastline detections was determined at each threshold value after applying all outlier detection criteria, resulting in the trend shown in Figure 4-9.

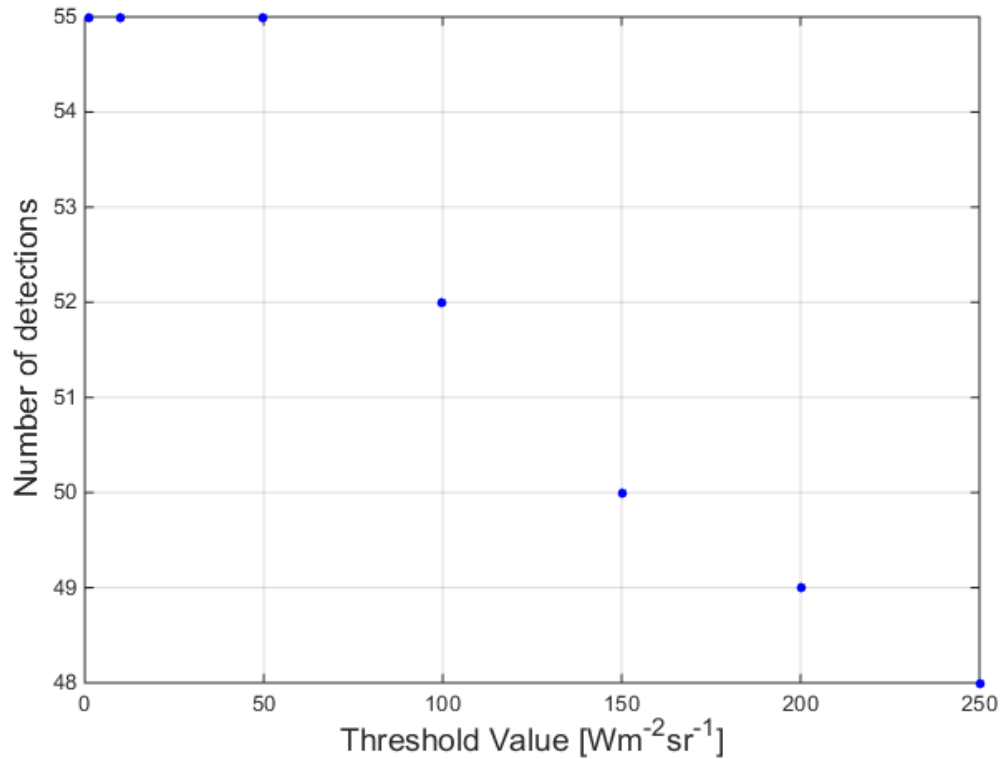


Figure 4-9 Number of coastline detections found vs cubic polynomial irradiance threshold value

Figure 4-9 shows a pair of trends present in the number of detections made as the irradiance difference threshold was increased. 55 coastline detections were found in the data consistently as the threshold value was increased from $1 \text{ Wm}^{-2}\text{sr}^{-1}$ to $50 \text{ Wm}^{-2}\text{sr}^{-1}$. Further increases in the threshold value resulted in fewer detections made. However, even at a threshold value of $250 \text{ Wm}^{-2}\text{sr}^{-1}$, 48 detections were made, a drop of 12.7% from the lowest threshold value of $1 \text{ Wm}^{-2}\text{sr}^{-1}$.

In summary, of the 270 NIR spectral data sets analyzed from Argus 1000, 55 coastline crossings were identified using the automated geolocation algorithm using the inflection point method. Further analysis showed that no conclusive relationship between angular

error and coastline crossing angle is observed. No significant observation was made for the degradation of angular error over the mission time. Lastly, the 1° (1σ) attitude knowledge mission requirement appears to be consistently met.

5 Radiometric Calibration of Near Infrared Spectrometers

Calibration of NIR spectrometers is a critical step, performed in a laboratory environment, in preparing the instruments for field use in any type of environment. Two calibrations are required for NIR spectrometers, such as Argus 1000, prior to field use. The first calibration, called wavelength calibration, is performed by the manufacturer to determine which wavelengths of light are captured on the pixels of the detector array of the spectrometer. Radiometric calibration, on the other hand, is typically performed by the instrument owner, and consists of relating the energy or power received by the instrument to the measurement scale of the detector array of the instrument. In most field applications, physical units such as power, energy, radiance, or irradiance are required for making spectral measurements, thereby requiring radiometric calibration results. These applications include EO remote sensing, such as the Argus 1000 measurement campaigns aboard CanX-2 or airborne validation campaigns, such as the validation of the coastline detection algorithm described in Chapter 6. The spectrometer flown in that campaign was the Ocean Optics' FLAME-NIR spectrometer, which was selected as its specifications are similar to that of Argus 1000, as shown in Table 5-1.

Table 5-1 Argus 100 and FLAME-NIR specifications [60], [63]

Specification	Argus 1000	FLAME-NIR
Mass	228 g	265 g
Dimensions	45 mm x 50 mm x 80 mm	89.1 mm x 63.3 mm x 31.9 mm
Spectral Range	950 nm – 1700 nm	927 nm – 1658 nm
Spectral Resolution	6 nm	<10 nm
Space Qualified	Yes	No

Radiometric calibration was performed for both Argus 1000 to understand the space flown unit, and subsequently for the FLAME-NIR, an equivalent NIR spectrometer, for use in UAV validation.

5.1 Laboratory Radiometric Calibration Setup

The radiometric calibration of NIR spectrometers involves relating the energy received by the instrument to the number of detector counts measured by the detector electronics of the instrument. In order to properly relate these quantities, a laboratory experiment was performed using a spectrometer (Argus 1000 Unit 8 and the FLAME-NIR), a calibrated light source, and an off-axis parabolic mirror (OAP) as shown in Figure 5-1.

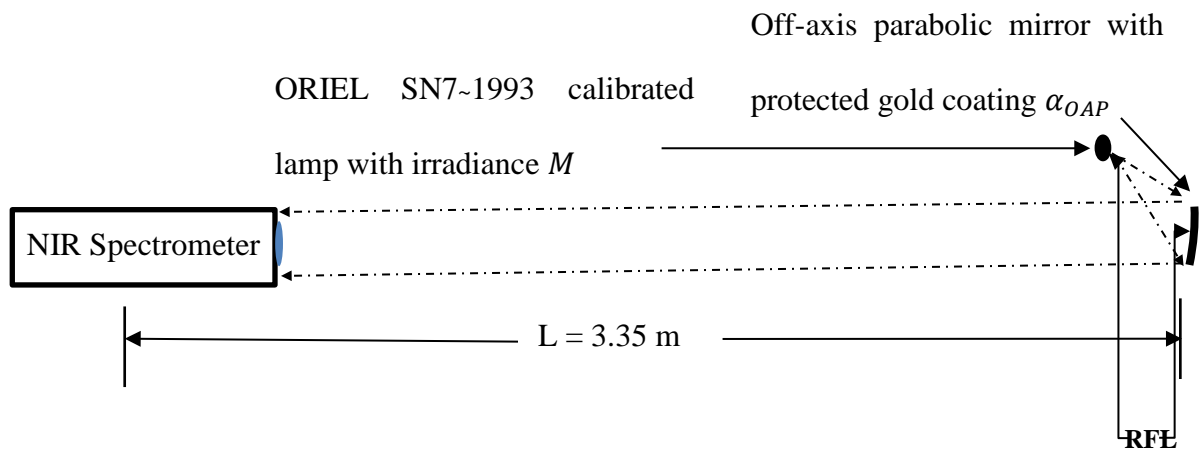


Figure 5-1 Laboratory setup of spectrometer radiometric calibration

The OAP is used to collimate the light from the lamp in the direction of the spectrometer. The spectrometer is placed on a rotation stage that is located in the path of the collimated light. The rotation stage is used to rotate the spectrometer so that its optics are perpendicular to the collimated light. An example of the radiometric calibration setup, including the spectrometer (in this case, Argus 1000) mounted on the rotation stage, is shown in Figure 5-2.

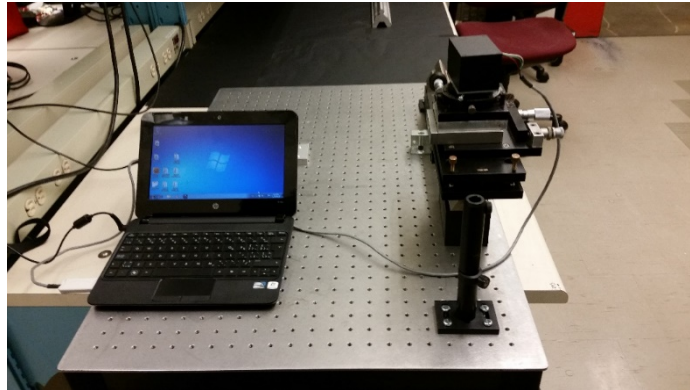


Figure 5-2 Argus 1000 radiometric calibration setup, consisting of spectrometer mounted on rotation stage (top), gold plated OAP (middle), and calibrated lamp (bottom)

The top image in Figure 5-2 shows the spectrometer mounted on the rotation stage and facing the OAP, with a computer used for instrument control. The data from the

spectrometer is monitored as the instrument is rotated using the rotation stage to ensure that all the pixels of the detector reach maximum saturation. The middle and bottom images in Figure 5-2 show the OAP and the calibrated lamp from the spectrometer's perspective and side perspective respectively. Non-reflective black foil is used to surround the lamp and mirror in order to reduce the effect of stray on the calibration. The use of a calibrated lamp and off-axis parabolic mirror for collimation is a common technique for the calibration of infrared detectors, as described in [64].

Once the spectrometer was in the correct orientation, data were collected using the spectrometer at a series of instrument settings at which two criteria were met:

1. the instrument was not saturated at all pixels
2. the number of counts on the detector was distinguishable from background noise signal at all pixels

5.2 Radiometric Calibration Model

The calibration equations used are based on the assumption that the irradiance M of the ORIEL SN7~1993 calibrated lamp can be treated as a point source. The irradiance of the lamp is provided by Newport at a distance l equal to 50 cm, which is then adjusted using the inverse square law to the reflected focal length RFL of the OAP mirror, as this the distance between the lamp and the centre of the mirror in the experimental setup. The irradiance of the lamp at l equal to 50 cm is a function of wavelength and is given by [65]

$$M = \lambda^{-5} * e^{a_1 + \frac{a_2}{\lambda}} * \left(a_3 + \frac{a_4}{\lambda} + \frac{a_5}{\lambda^2} + \frac{a_6}{\lambda^3} + \frac{a_7}{\lambda^4} + \frac{a_8}{\lambda^5} \right) \quad (7)$$

where $a_i = a_1, \dots, a_8$ are lamp specific calibration constants provided by Newport.

Further scaling of the irradiance is then performed to take into account the reflectance α_{OAP} of the OAP mirror, which is a function of wavelength, and the angle θ between the OAP mirror and the spectrometer field of view (FOV). The irradiance is then converted to energy by multiplying it by the exposure time setting of the instrument. Lastly, comparison of different instrument capacitor, number of scans, and samples per pixel settings is carried out by converting to the equivalent energy per count at a setting of 1 scan and 1 sample per pixel. The final equation used to determine the spectral exposure per detector count is shown below.

$$JPC = \frac{M \left(\frac{l^2}{RFL^2} \right) \cos(\theta) (\alpha_{OAP}) (\Delta t_e) C_{col}}{\left(\frac{N_c}{n_s S_{pp}} \right)} \quad (8)$$

where JPC is the spectral exposure per detector count [$\text{Jm}^{-2}\text{nm}^{-1}\text{count}^{-1}$]

M is the irradiance of the ORIEL SN7-1993 calibrated lamp converted to [$\text{Wm}^{-2}\text{nm}^{-1}$]

l is the distance at which M is provided for [$l = 50\text{cm}$]

RFL is the reflected focal length of the OAP mirror, i.e. the distance from the lamp to the mirror [$RFL = 27.223 \text{ cm}$]

θ is the angle between the mirror and the spectrometer FOV [$\theta = 0$]

α_{OAP} is the reflectance of the OAP mirror [%]

C_{col} is a correction factor for collimation error based on the ratio of the measured area of the collimated beam to the expected area of the collimated beam [$C_{col} = 0.0352$]

Δt_e is the exposure time setting [s]

n_s is the number of scan counts setting

N_c is the number of detector counts in the data

S_{pp} is the number of samples per pixel

For Argus 1000, n_s and S_{pp} are instrument settings that are varied during calibration, while for the FLAME-NIR, n_s and S_{pp} are not instrument settings and are therefore always equal to 1.

The uncertainty of the calculated JPC value is determined using the law of error propagation [66]

$$\sigma_f = \sqrt{\left(\frac{\partial f}{\partial x_1}\right)^2 \sigma_{x_1}^2 + \left(\frac{\partial f}{\partial x_2}\right)^2 \sigma_{x_2}^2 + \dots + \left(\frac{\partial f}{\partial x_{k-1}}\right)^2 \sigma_{x_{k-1}}^2 + \left(\frac{\partial f}{\partial x_k}\right)^2 \sigma_{x_k}^2} \quad (9)$$

where σ_f is the standard deviation of the function $f(x_1, x_2, \dots, x_{k-1}, x_k)$ of k independent variables with respective variances $\sigma_{x_1}^2, \dots, \sigma_{x_k}^2$. Uncertainties in the irradiance, reflected focal length, angle between mirror and spectrometer, mirror reflectance, and exposure time setting are used to calculate uncertainties for JPC for each data set. The partial derivatives of the JPC function are

$$\begin{aligned}
\frac{\partial f}{\partial M} &= \frac{\left(\frac{l^2}{RFL^2}\right) \cos(\theta) (\alpha_{OAP})(\Delta t_e) C_{col}}{\left(\frac{N_c}{n_s S_{pp}}\right)} \\
\frac{\partial f}{\partial RFL} &= \frac{-2M \left(\frac{l^2}{RFL^3}\right) \cos(\theta) (\alpha_{OAP})(\Delta t_e) C_{col}}{\left(\frac{N_c}{n_s S_{pp}}\right)} \\
\frac{\partial f}{\partial \theta} &= \frac{-M \left(\frac{l^2}{RFL^2}\right) \sin(\theta) (\alpha_{OAP})(\Delta t_e) C_{col}}{\left(\frac{N_c}{n_s S_{pp}}\right)} \\
\frac{\partial f}{\partial \alpha_{OAP}} &= \frac{M \left(\frac{l^2}{RFL^2}\right) \cos(\theta) (\Delta t_e) C_{col}}{\left(\frac{N_c}{n_s S_{pp}}\right)} \\
\frac{\partial f}{\partial t_e} &= \frac{M \left(\frac{l^2}{RFL^2}\right) \cos(\theta) (\alpha_{OAP}) C_{col}}{\left(\frac{N_c}{n_s S_{pp}}\right)}
\end{aligned} \tag{10}$$

The variances of each of the above quantities was determined either from the data sheet provided for that quantity or from uncertainties in the experimental setup. The uncertainties in the irradiance and off-axis parabolic mirror reflectance were provided by Newport and Edmund optics respectively, while the uncertainty in the exposure time was taken to be the frequency of the clock in the InGaAs detector, which was listed in the detector data sheet provided by Sensors Unlimited in the case of Argus 1000 and by Hamamatsu in the case of the FLAME-NIR. The uncertainties in the reflected focal length and angle were determined through the experimental setup.

5.3 Argus 1000 Unit 8 Radiometric Calibration Results

Data was collected using the spectrometer at a series of instrument settings, and is organized under the two possible sensitivity settings, i.e. the 0.4 pF high sensitivity and 10 pF low sensitivity capacitor settings. At each exposure time setting, three data sets were collected, with the number of scans and samples per pixel settings varied to allow the effects of those settings to be determined. In addition to the three data sets, measurements of the background noise signal were taken with the ORIEL lamp turned off at four of the exposure time settings. In total, 19 data sets were taken, broken down into the following categories.

1. 8 data sets at the 0.4 pF capacitor setting, consisting of 2 background data sets, 3 data sets at a 1 ms exposure time setting, and 3 data sets at a 2 ms exposure time setting.
2. 11 data sets at the 10 pF capacitor setting, consisting of 2 background data sets, 3 data sets at a 16 ms exposure time setting, 3 data sets at a 32 ms exposure time setting, and 3 data sets at a 64 ms exposure time setting.

Since the radiometric calibration of Argus 8 is based on relating the power received by the spectrometer from a calibrated source to the number of detector counts recorded by the instrument, it is important to understand the wavelength dependence of the irradiance of the calibrated lamp. Figure 5-3 shows the irradiance of the calibrated lamp as a function of wavelength at the given distance of l equal to 50 cm from the lamp, generated using the parameters provided by Newport [65].

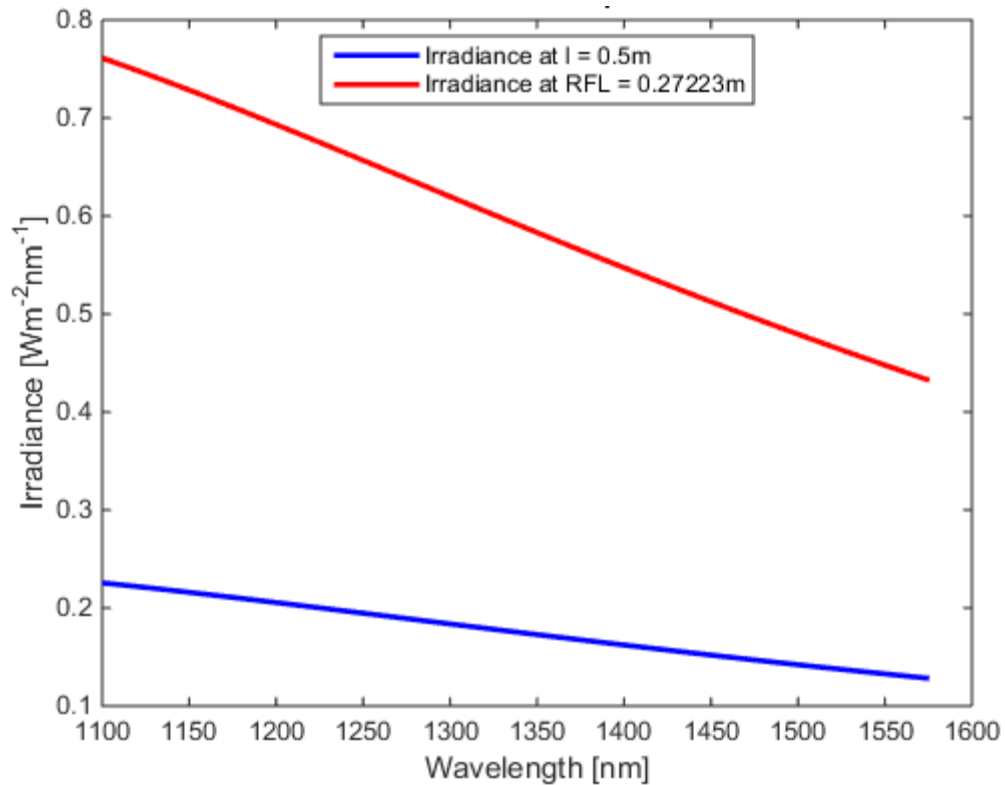
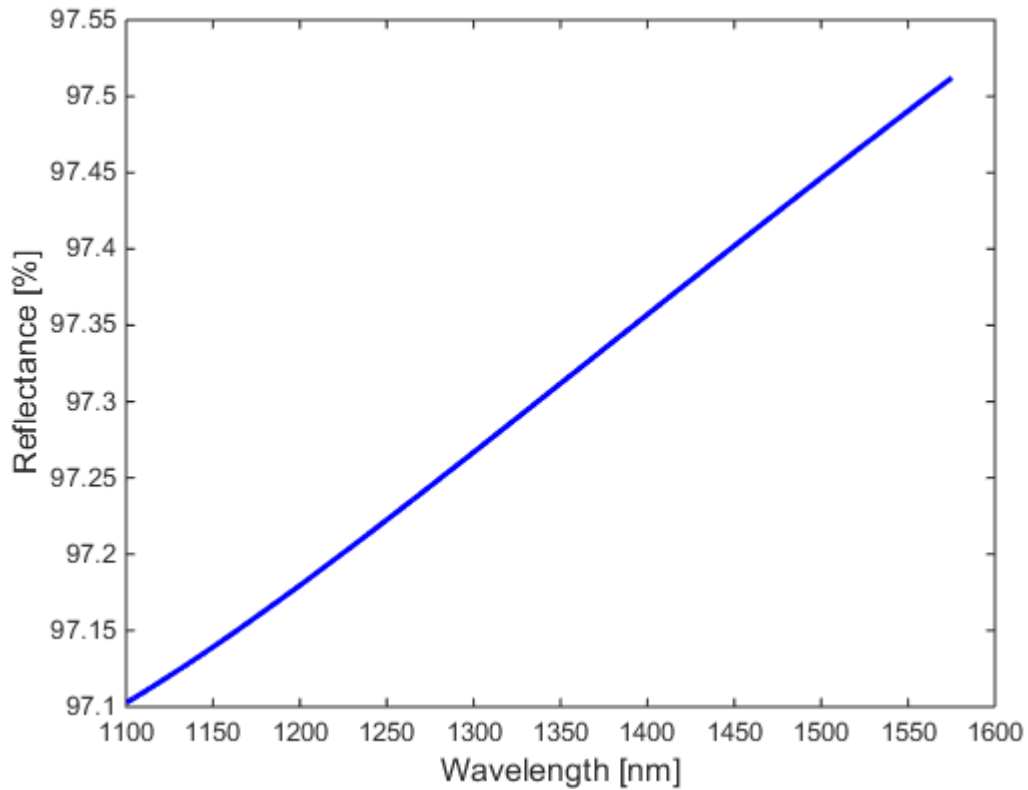


Figure 5-3 Irradiance vs wavelength of 1000W ORIEL calibrated lamp model SN7-1993 (adapted from [65])

As shown in Figure 5-3, the irradiance vs wavelength curve produced by the ORIEL SN7-1993 is in the shape of blackbody curve in the spectrometer's wavelength range of 1100 nm to 1574 nm. At lower wavelengths, the irradiance is greater than at higher wavelengths. Adjusting for the placement of the mirror at the reflected focal length distance $RFL = 27.223\text{ cm}$ using the inverse square law produces the red curve shown in Figure 5-3, which is the irradiance value received by the OAP mirror from the calibrated lamp. Since the surface of the OAP mirror is protected gold, over 97% of this irradiance is reflected by the mirror, as shown in Figure 5-4.



**Figure 5-4 Reflectance vs wavelength of gold plated off-axis parabolic mirror
(adapted from [67])**

The reflectance curve of the OAP mirror shown in Figure 5-4 is only 0.4% over the wavelength range from 1100 nm to 1600 nm, thereby maintaining the overall shape of the irradiance as received by the spectrometer at its lens. The spectral exposure per detector count (JPC) function from the calibration process is determined for the product of the irradiance shown in Figure 5-3 and the reflectance curve shown in Figure 5-4 divided by the number of counts measured by the detector of the instrument at each wavelength, as this represents the irradiance received by the spectrometer lens. The energy of each photon that is detected by the instrument is dependent on its wavelength according to the equation

$$E_p = \frac{hc}{\lambda} \quad (11)$$

This means that the number of detector counts measured by the instrument will differ at each wavelength, even if the energy received at each wavelength is the same. For the irradiance received by the instrument at the lens, the product of the irradiance, exposure time, lens area, and pixel wavelength range provides the total energy received by the instrument at each wavelength. When this is divided by the energy of each photon, the expected number of photons detected as a function of wavelength can be determined, as shown in Figure 5-5.

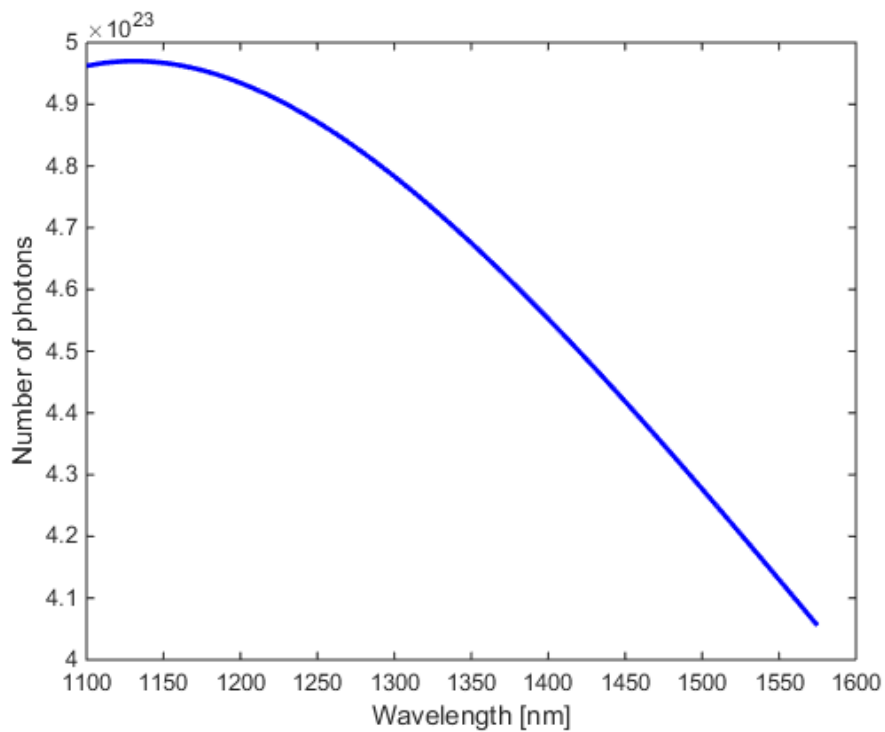


Figure 5-5 Expected number of photons received by the detector at each wavelength at an exposure time of 256 ms

Figure 5-5 shows that the number of photons detected by the instrument is expected to decrease as the wavelength increases, implying that the number of detector counts recorded by the instrument should also decrease as the wavelength increases. However, several internal components in the spectrometer itself may cause the irradiance received by the detector itself to differ from the irradiance curve at the lens. The JPC curve calculated is therefore a function which relates this instrument irradiance at the lens to the actual number of detector counts, i.e. it is an instrument specific function that does not include correction factors to the irradiance received by the instrument due to these internal components.

The first of the internal components that may affect the irradiance received by the instrument is the efficiency of the diffraction grating, shown in Figure 5-6.

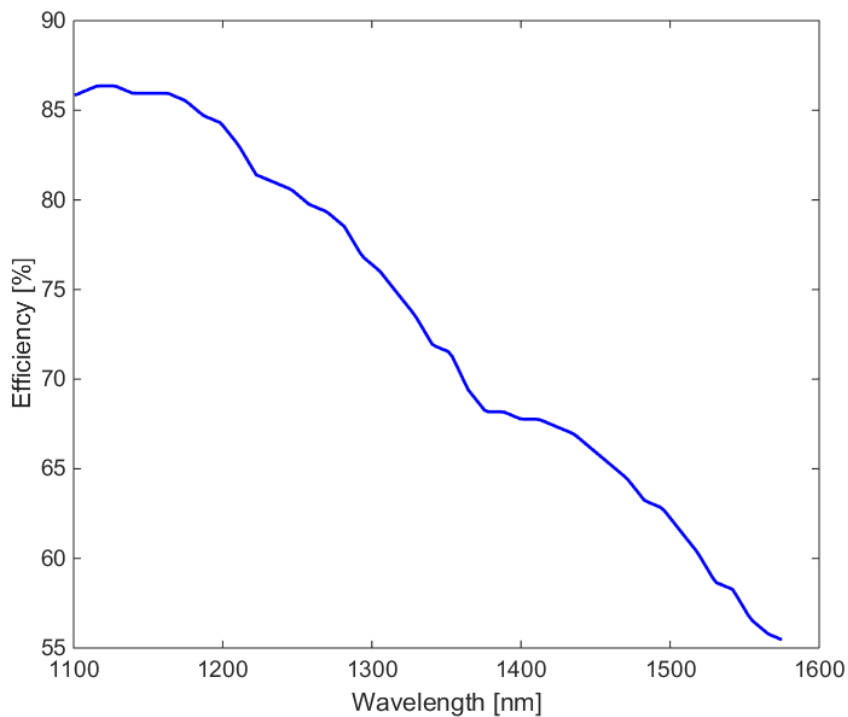


Figure 5-6 Diffraction grating efficiency vs wavelength (adapted from [68])

As shown in Figure 5-6, the efficiency of the diffraction grating drops over the wavelength range, thereby lowering the expected number of detector counts at higher wavelengths. The transmittance of the spectrometer lens is also a function of wavelength, as shown in Figure 5-7.

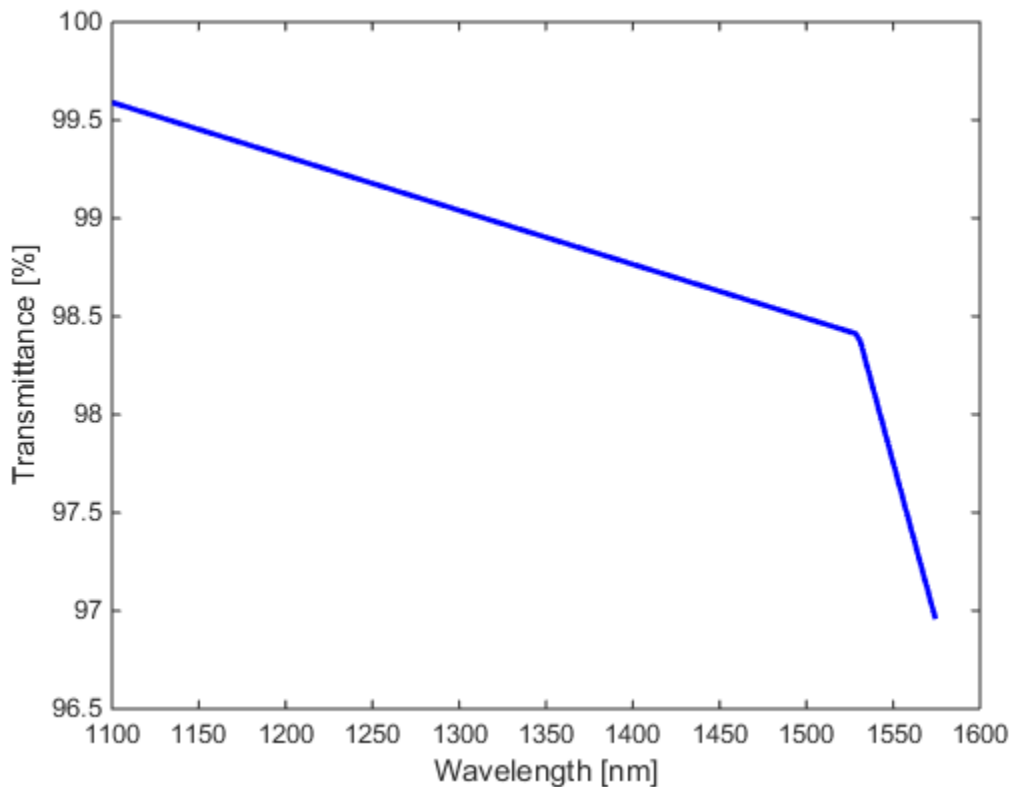


Figure 5-7 Lens transmittance vs wavelength (adapted from [68])

Figure 5-7 shows that the transmittance of the lens has a significant drop from about 1525 nm toward the end of the wavelength range. Combined with the drops in the grating efficiency and irradiance at those wavelengths, a large drop at higher wavelengths is expected to occur in the spectrometer. Lastly, the quantum efficiency of the detector itself

is wavelength dependent and therefore affects the irradiance as well, as shown in Figure 5-8.

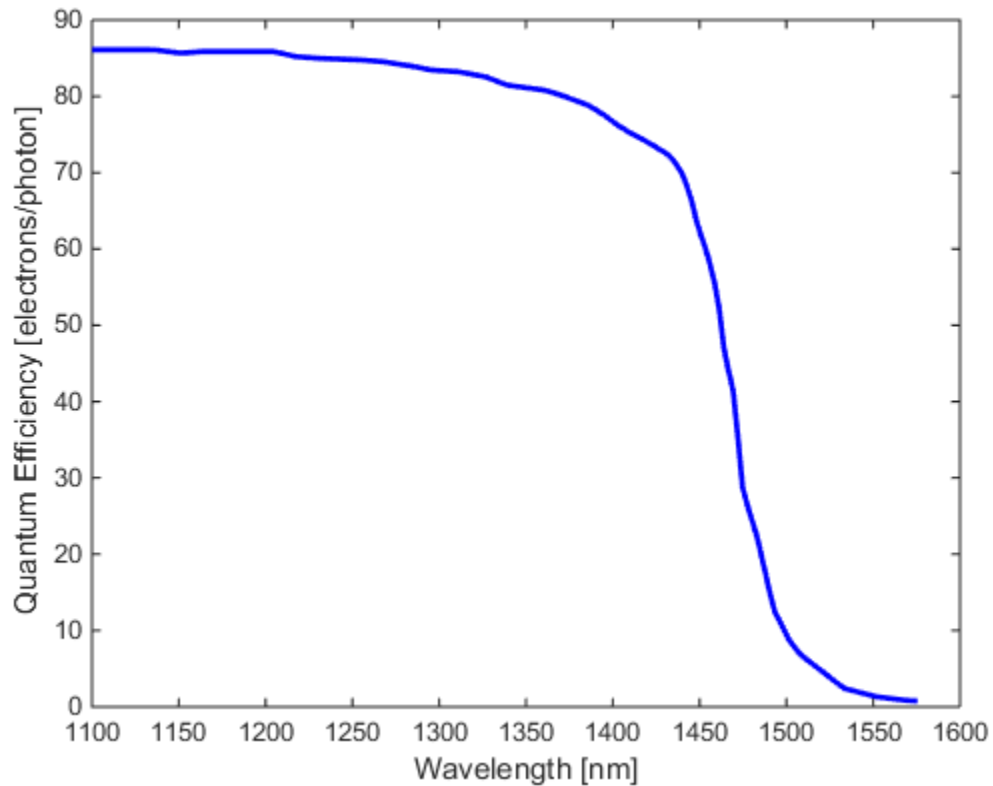


Figure 5-8 Detector quantum efficiency vs wavelength (adapted from [69])

The quantum efficiency of the detector, shown in Figure 5-8, begins to drop off near 1450 nm and falls almost to zero at the end of the spectrometer wavelength range. Combining the quantum efficiency of the detector with the transmittance of the lens, the reflectance of the off-axis parabolic mirror, the efficiency of the diffraction grating, and the irradiance of the lamp provides the irradiance received by the spectrometer, as shown in Figure 5-9.

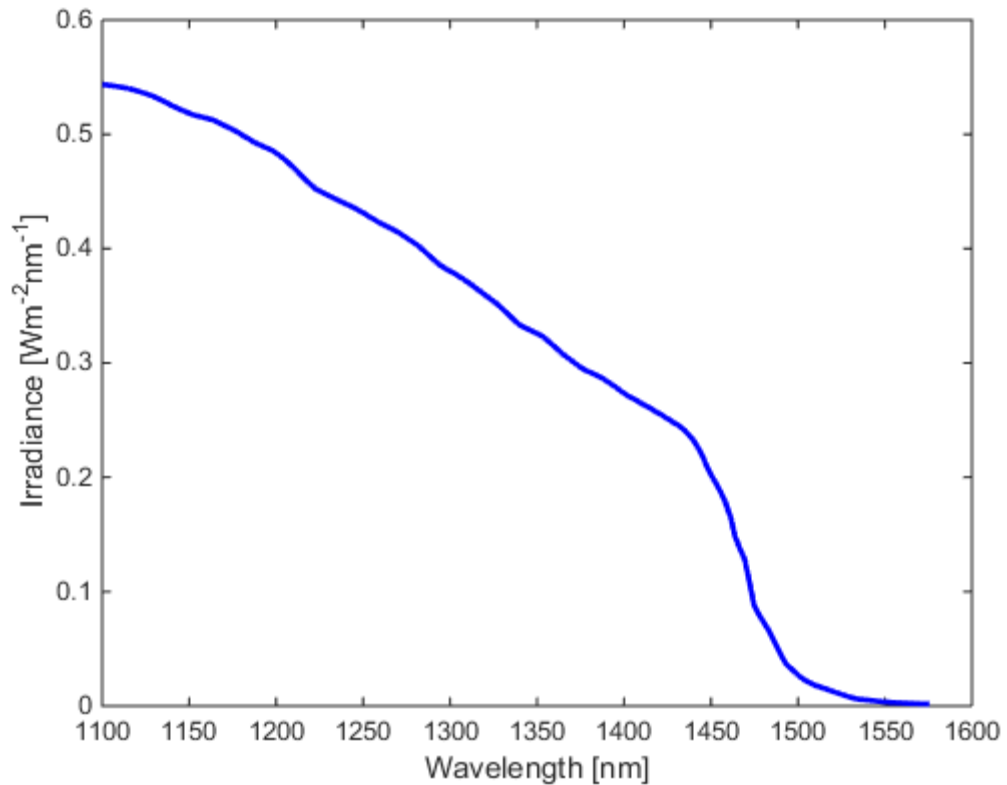


Figure 5-9 Lamp irradiance received by spectrometer detector vs wavelength

As shown in Figure 5-9, the irradiance received by the spectrometer drops as wavelength increases and deviates from the theoretical blackbody curve due to the effects of the diffraction grating, spectrometer lens, off-axis parabolic mirror, and detector quantum efficiency, as described previously. At wavelengths greater than about 1440 nm, the irradiance drops rapidly due to these effects. The number of detector counts recorded by the instrument electronics is expected to deviate from the theoretical shape due to these effects.

In addition to the data sets collected using the calibrated lamp, four data sets, each at a different exposure time, were taken of the number of detector counts measured by Argus

1000 with the calibrated lamp turned off. These data sets are the background signal present and are shown in Figure 5-10.

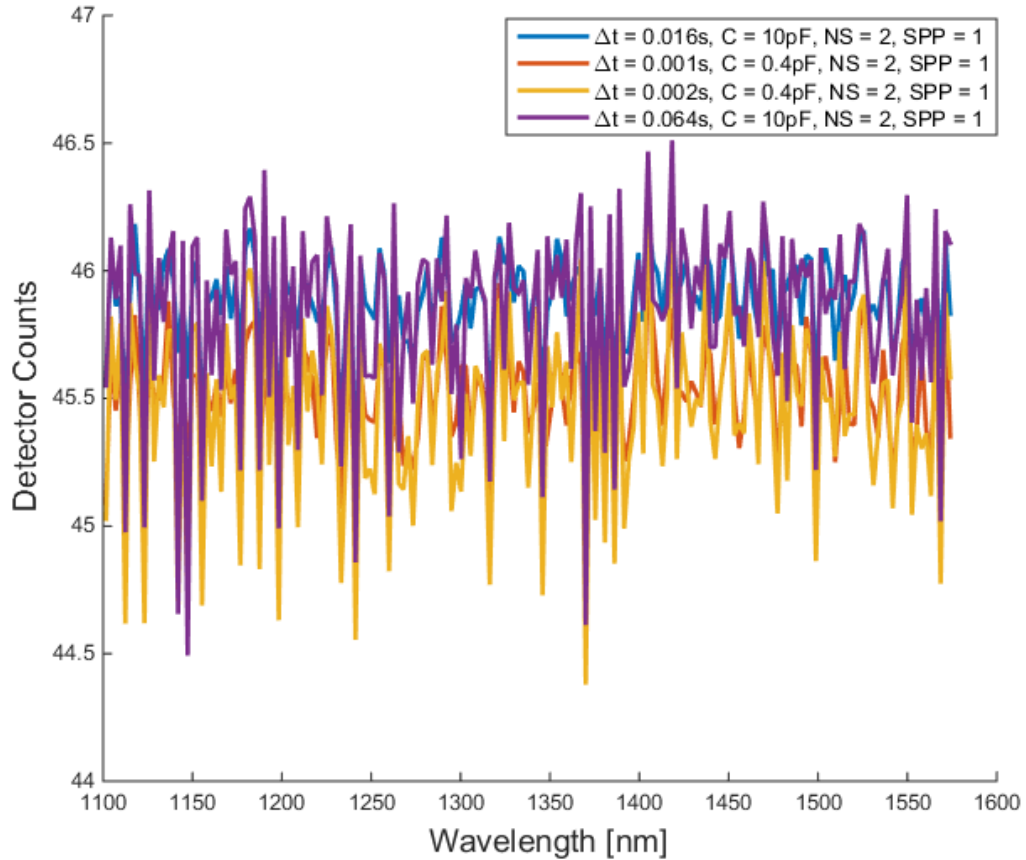


Figure 5-10 Background detector counts vs wavelength at four exposure time settings for Argus 1000 radiometric calibration

As shown in Figure 5-10, the background counts have very little variation with exposure time, an unexpected result. The total number of background counts varies from a low of 45 to a high of 46. Additionally, the wavelength variation of the background counts is small, changing by at most 2 counts over the 1100 nm to 1600 nm wavelength range. Since the

detector is a CMOS device, its electronics may already contain background subtraction, thereby eliminating the variation of noise with increased exposure time.

The data sets were taken using the instrument over a period of at least 2 minutes at each setting, thereby providing sufficient packets for analysis. At the highest exposure time setting of 64 ms with the number of scans set to 2 and a packetization time of 100 ms, 2 minutes of data acquisition corresponds to 526 packets of calibration data at that setting. Lower numbers of co-added scans and exposure time settings increase the number of packets acquired substantially, as shown in Table 5-2.

Table 5-2 Calibration data settings and total packet numbers

Capacitor Setting	Exposure Time Setting	Number of Co-added Scans	Samples Per Pixel	Total Number of Packets
0.4 pF	1 ms	1	1	2734
		2	1	1915
			4	1682
	2 ms	1	1	2818
		2	1	1460
			4	1322
10 pF	16 ms	1	1	2192
		2	1	1232
			4	866
	32 ms	1	1	2128
		2	1	673
			4	898
	64 ms	1	1	1543
		2	1	742
			4	634

As shown in Table 5-2, the total number of packets in each data set decreases as the number of co-added scans increases and the lower the exposure time setting, the more packets in each data set. The lowest number of packets acquired for a data set was 634 at the highest exposure time and number of scans setting.

At a fixed capacitor setting, the raw data, in the form of detector counts, changes proportionally with the exposure time, number of scans, and samples per pixel. The variation of the number of detector counts with wavelength can therefore be seen at one series of settings, as shown in Figure 5-11.

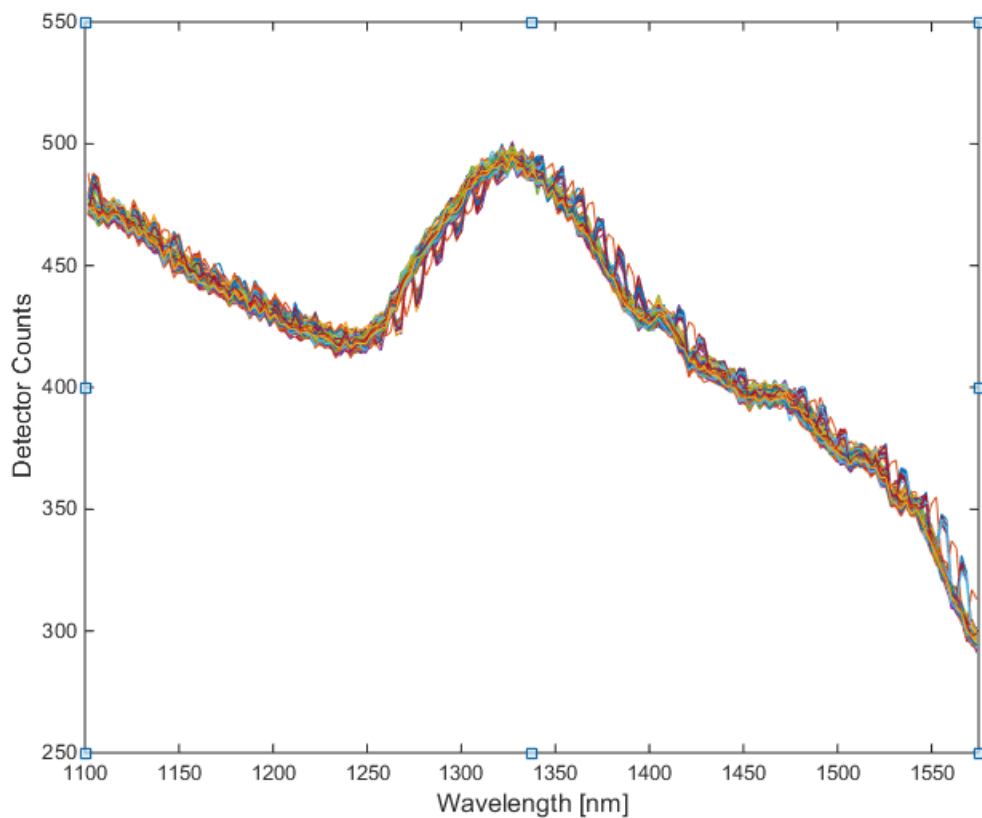


Figure 5-11 Detector counts vs wavelength for $\Delta t = 0.064$ s, $C = 10$ pF, $NS = 1$, and $SPP = 1$ for Argus 1000 with each packet identified by colour

As shown in Figure 5-11, the number of detector counts drops as the wavelength increases, with the exception of an increase that occurs from about 1250 nm to about 1325 nm at all packets. In addition to this feature, some packets show a periodic variation of detector counts vs wavelength. The setting of 0.064 s is the highest exposure time setting at which the instrument did not saturate with the capacitor set to 10 pF. A similar trend in the detector counts can be seen with the capacitor set to 0.4 pF at an exposure time setting of 0.002 s, as shown in Figure 5-12. This exposure time setting is the highest at which saturation of the instrument did not occur with the capacitor set to 0.4 pF.

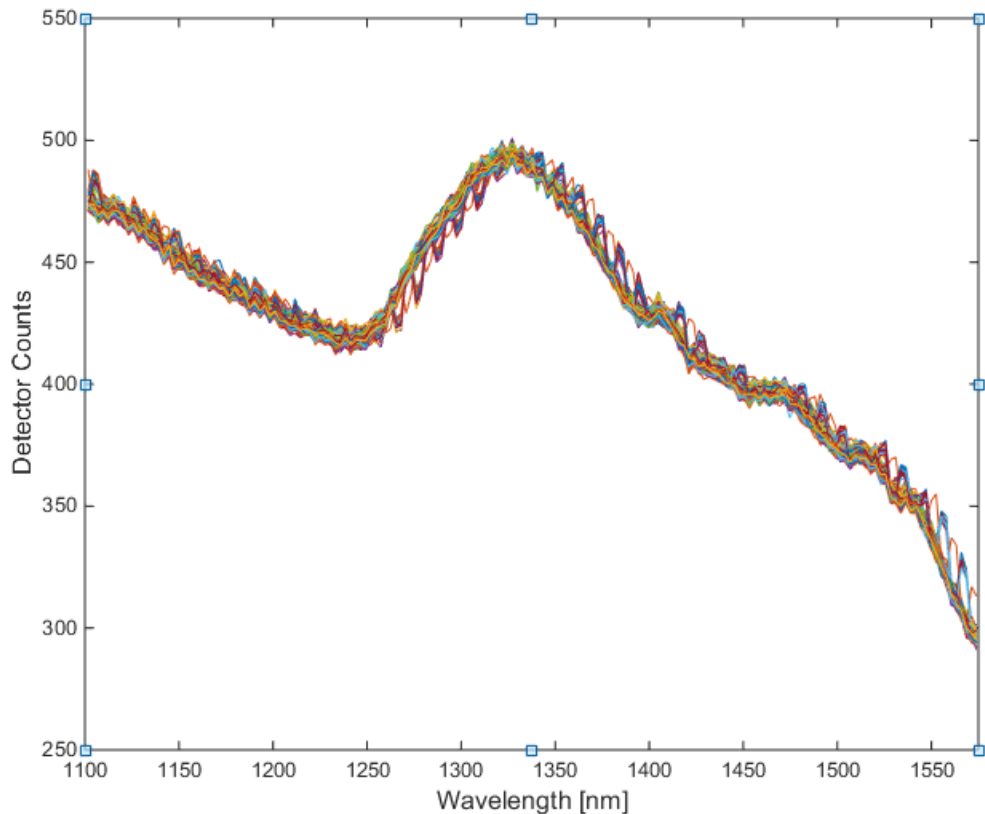


Figure 5-12 Detector counts vs wavelength for $\Delta t = 0.002$ s, $C = 0.4$ pF, $NS = 1$, and $SPP = 1$ for Argus 1000 with each packet identified by colour

As shown in Figure 5-12, the same trend in detector counts vs wavelength is present with the capacitor set to 0.4 pF. The detector counts generally decrease with wavelength, however an increase occurs from about 1250 nm to 1325 nm at all packets. The periodic variation of the detector counts present in some packets in Figure 5-11 is absent at a capacitor setting of 0.4 pF, however. Additionally, a large drop in detector counts to 25 counts occurs at the 0.4 pF capacitor setting at about 1120 nm at all packets. This drop is always present at 1120 nm with the capacitor set to 0.4 pF and is likely due to an issue with the detector electronics at this pixel at 0.4 pF. In all subsequent analyses of the data sets at 0.4 pF, this feature is removed from the data and linear interpolation of the detector counts is performed at this wavelength. The variation of the detector counts over time can be analyzed by studying the number of detector counts at a particular pixel, as shown in Figure 5-13.

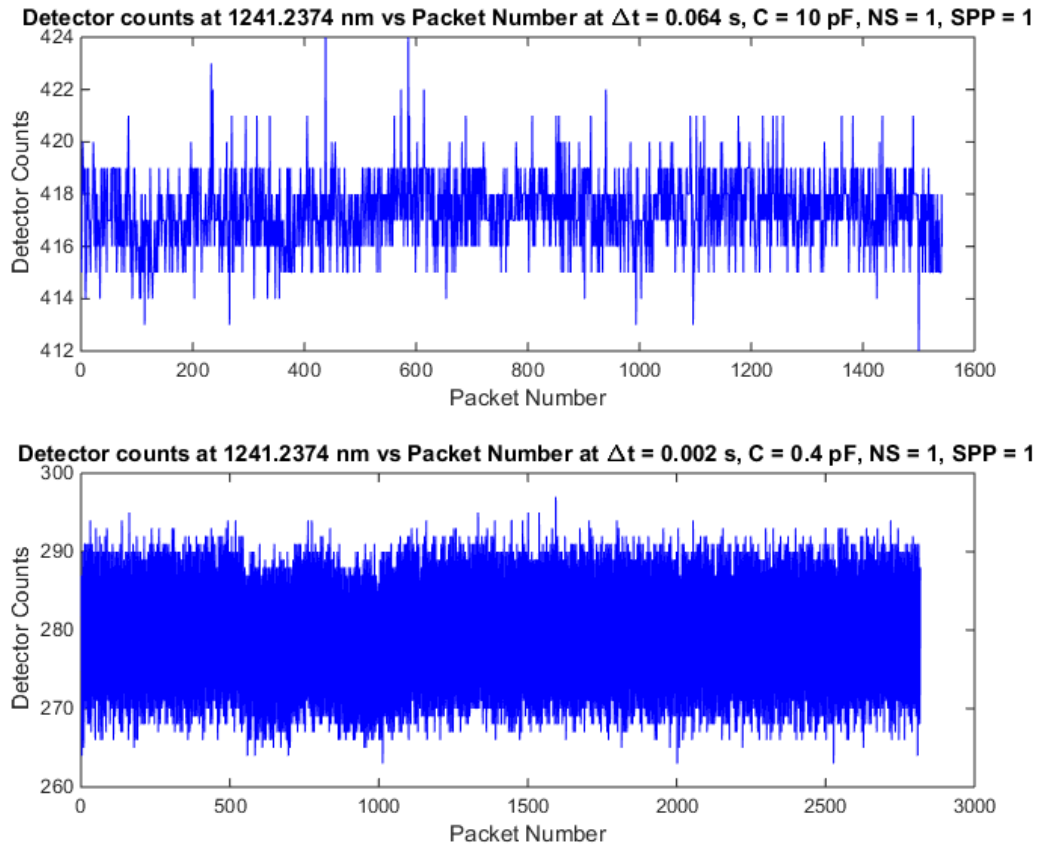


Figure 5-13 Detector counts vs packet number at pixel 125 (1241.2374 nm) for Argus 1000

As shown in Figure 5-13, the detector counts at 0.4 pF, located on the bottom curve, show variation consistent with the presence of white noise. The detector counts at 10 pF, however, contain occasional drops and increases, likely the cause of the periodic behaviour present in some packets in Figure 5-11. In the other packets, however, the detector counts vary by a small number of counts only, a variation also consistent with the presence of white noise.

The background signal shown in Figure 5-10 is not subtracted from the detector counts shown in Figure 5-11, as its removal affects the results at lower exposure times more than those at higher exposure times due to its constant nature. Instead, the detector counts at each packet are converted to spectral exposure per count using the equation described previously. The mean value of the spectral exposure per count at each wavelength of all the packets is then determined, along with its associated uncertainty. For the case of an exposure time setting of 0.064 s and a capacitor setting of 10 pF, the resulting spectral exposure per count vs wavelength curve is shown in Figure 5-14, with 1σ error bars plotted at each wavelength value.

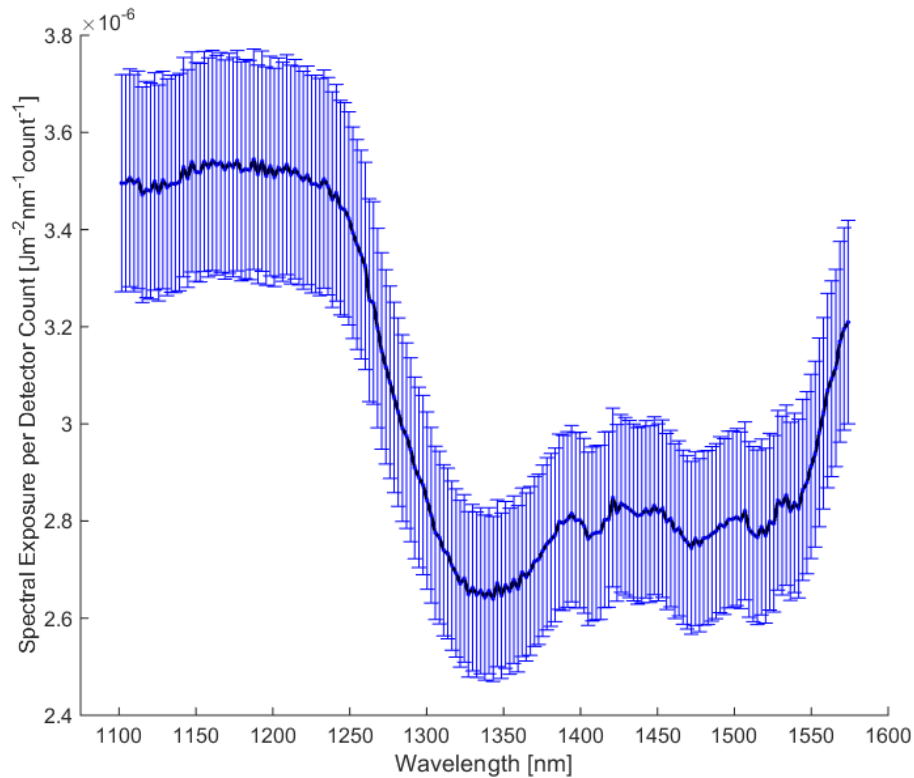


Figure 5-14 Spectral exposure per detector count (JPC) vs wavelength for $\Delta t = 0.064$ s, $C = 10$ pF, $NS = 1$, and $SPP = 1$ for Argus 1000

As shown in Figure 5-14, the spectral exposure per detector count (JPC) decreases with wavelength at an exposure time setting of 0.064 s and a capacitor setting of 10 pF, with a large decrease occurring between 1250 nm and 1325 nm. The overall trend in JPC is consistent with theoretical results, as photons at higher wavelengths have less energy so each detector count at higher wavelengths is expected to consist of more photons. The drop near the centre of the JPC curve corresponds to the peak present in the data shown in Figure 5-11. The uncertainty in JPC is also shown and is less than 10% of the JPC value at each wavelength. The same conversion from detector counts to JPC is performed for the data in Figure 5-12 and is shown in Figure 5-15.

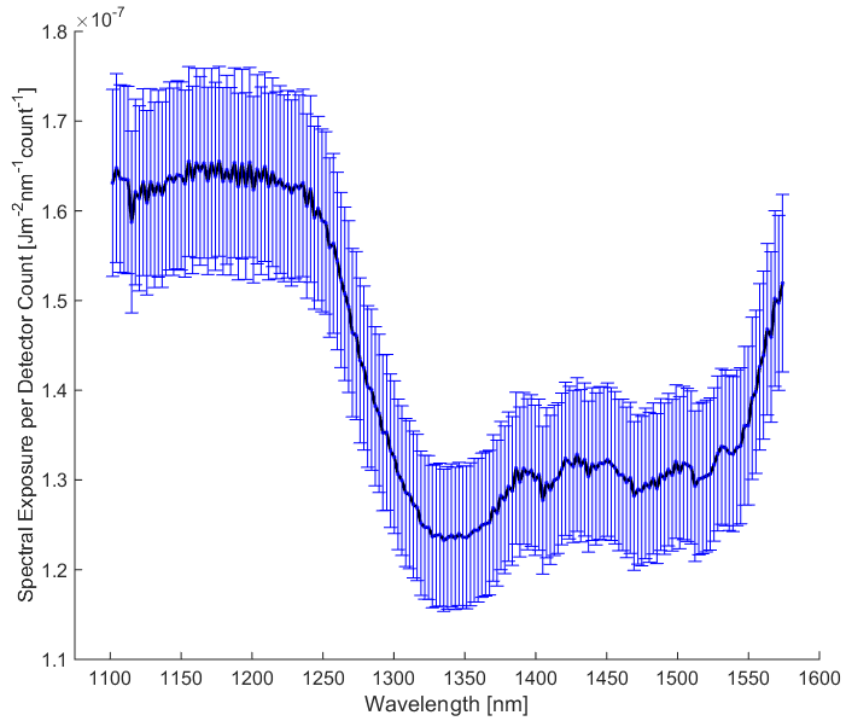


Figure 5-15 Spectral exposure per detector count (JPC) vs wavelength for $\Delta t = 0.002$ s, $C = 0.4$ pF, $NS = 1$, and $SPP = 1$ for Argus 1000

Figure 5-15 shows a similarly shaped trend for JPC vs wavelength for the 0.4 pF and 0.002 s exposure time case. The JPC values, however, have a magnitude of 4.40% on average of the 0.064 s and 10 pF case. Additionally, the uncertainty bars are of the same order of magnitude as in the 0.064 s and 10 pF case.

In addition to the individual mean JPC curves calculated for each data set, a comparison between the mean JPC values of all the data sets taken at a particular exposure time setting allows the effect of the scan count and samples per pixel setting on the JPC to be

determined. For the data sets taken at 10 pF, the mean JPC curves at each exposure time setting are shown in Figure 5-16.

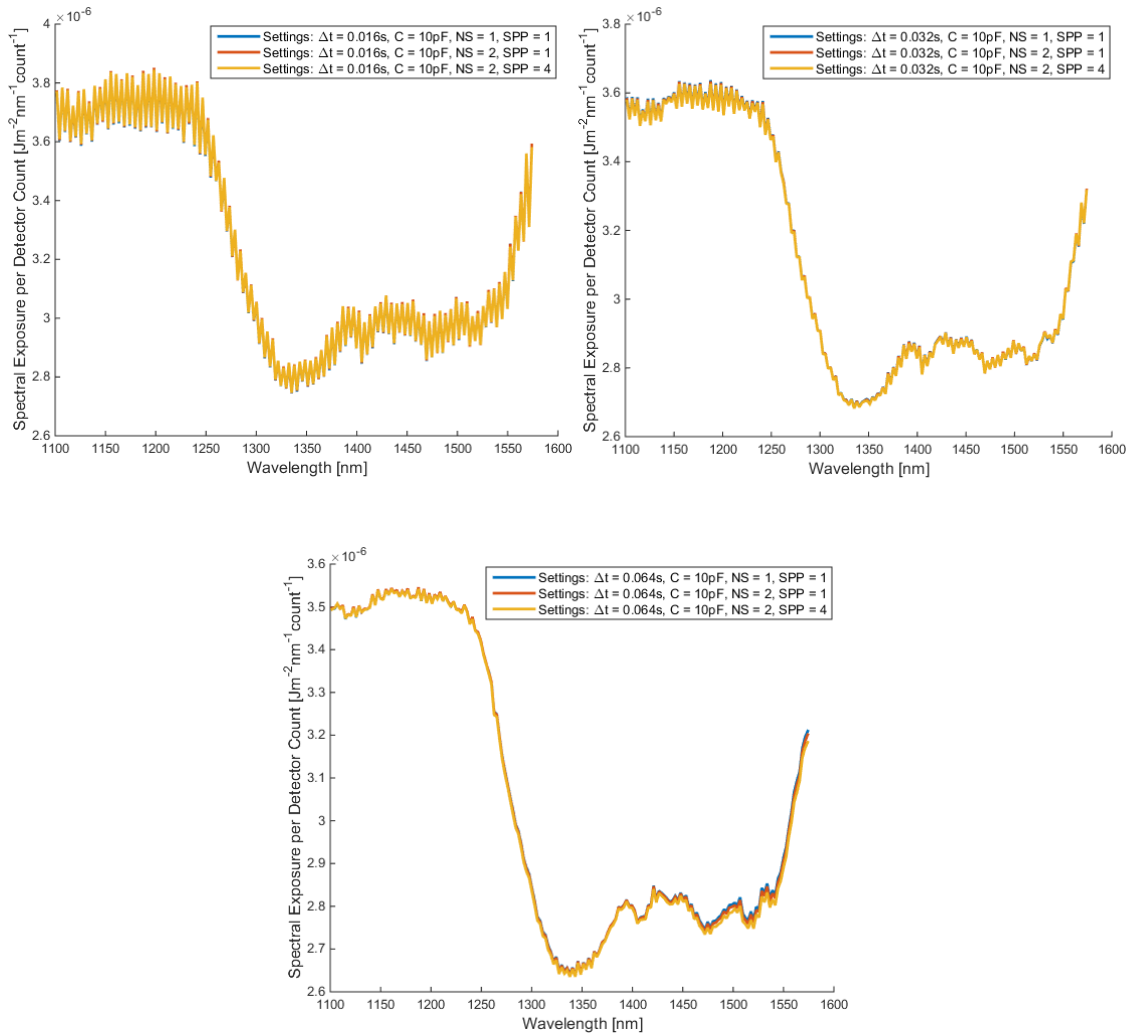


Figure 5-16 Spectral exposure per detector count vs wavelength at $C = 10$ pF for Argus 1000. (Top left: $t = 0.016$ s, Top right: $t = 0.032$ s, Bottom: $t = 0.064$ s)

As shown in Figure 5-16, the JPC values are close at all three exposure time settings, regardless of the number of scans and samples per pixel settings. At an exposure time

setting of 0.016 s, however, the JPC curve has higher variability than the 0.032 s and 0.064 s cases. At this exposure time setting, the detector counts are closest to the noise.

The same analysis is conducted for the data sets taken with the capacitor set to 0.4 pF, as shown in Figure 5-17.

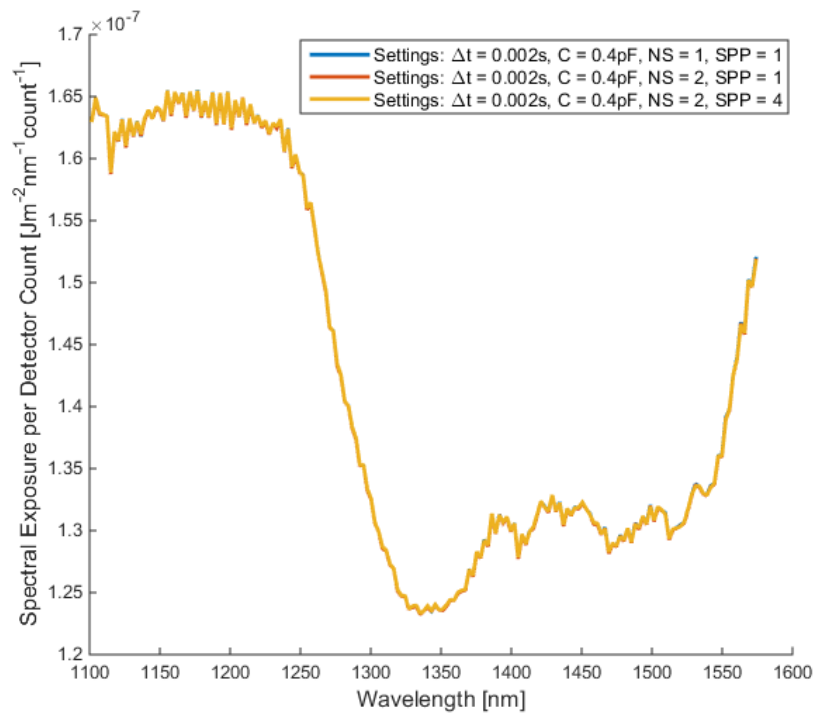
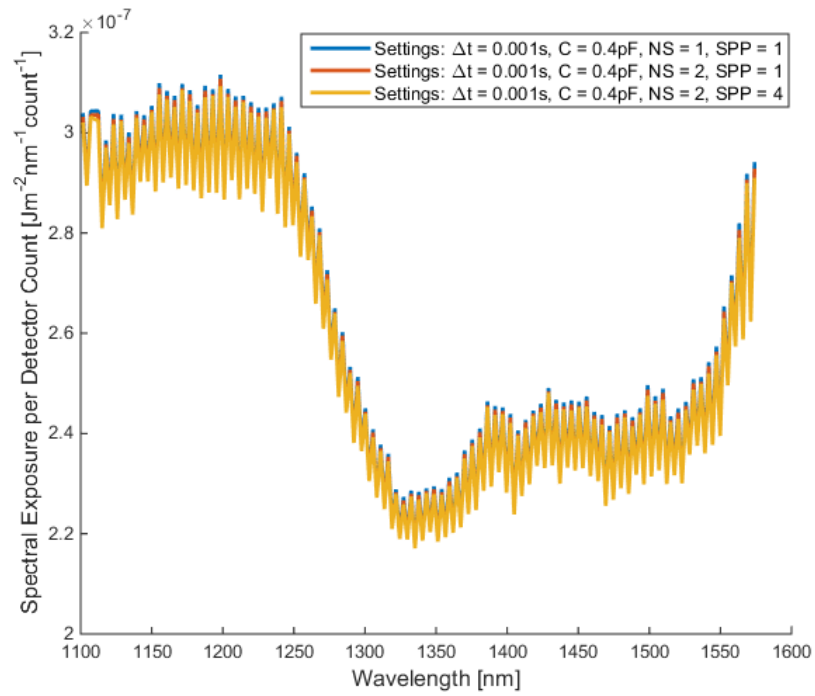


Figure 5-17 Spectral exposure per detector count vs wavelength at $C = 0.4$ pF for Argus 1000. (Top: $t = 0.001$ s, Bottom: $t = 0.002$ s)

The same trends are visible in the 0.4 pF data sets with the same exposure time as for the 10 pF case. The number of scans and samples per pixel setting do not affect the JPC values at both the 0.001 s and 0.002 s exposure time settings. However, a large variation in JPC from wavelength to wavelength is present in the exposure time setting of 0.001 s as at this setting, the number of detector counts is most affected by the background signal.

The full variation of the mean JPC values for the 10 pF capacitor data sets are shown in Figure 5-18.

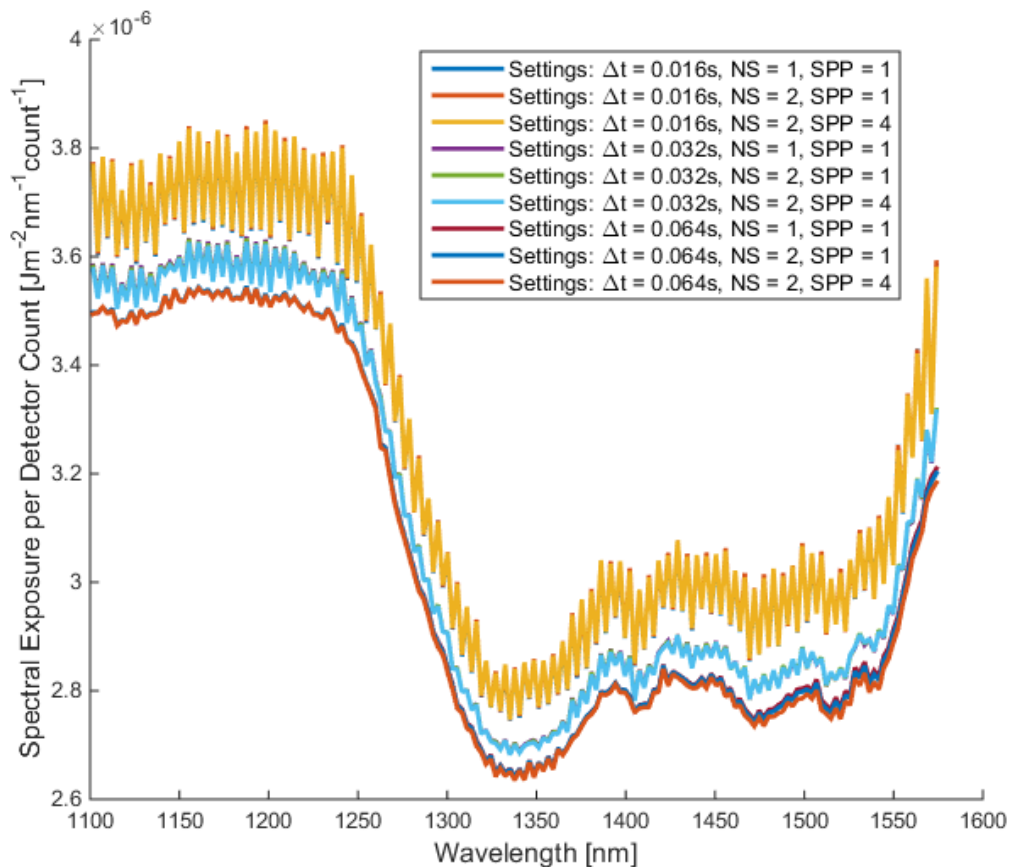


Figure 5-18 Spectral exposure per detector count vs wavelength of all data sets at 10 pF for Argus 1000

Figure 5-18 shows that all the data sets taken at a capacitor setting of 10 pF have the same shape, consisting of an increase in JPC as wavelength increases. Six of the JPC curves at 10 pF are clustered together, with values around $3.5 \times 10^{-6} \text{ Jm}^{-2}\text{nm}^{-2}\text{count}^{-1}$ at 1100 nm and around $3.2 \times 10^{-5} \text{ Jm}^{-2}\text{nm}^{-2}\text{count}^{-1}$ at 1574 nm. These JPC curves are the ones at the highest exposure time setting, i.e. the ones with the largest number of detector counts, and are therefore least affected by the background signal. The remaining three JPC curves are slightly higher and noisier than the other six and correspond to the data sets with the lowest detector counts and exposure time setting.

A similar spread of results is found in the data sets at 0.4 pF, as shown in Figure 5-19.

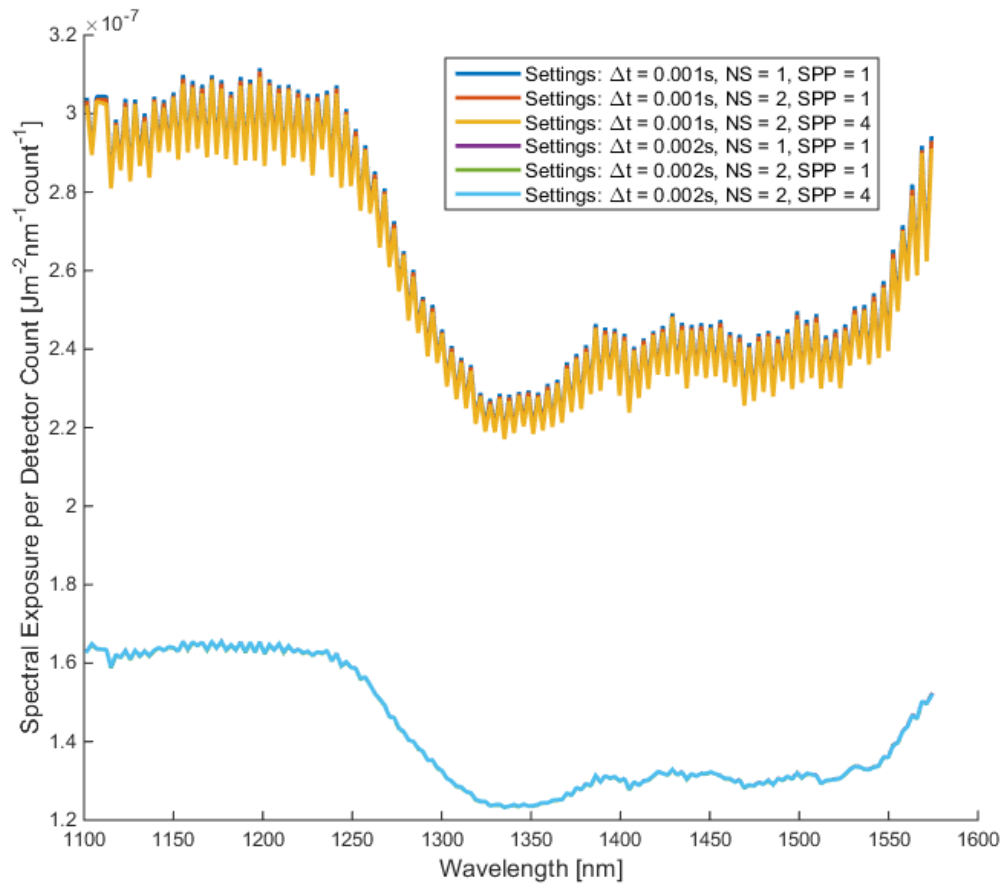


Figure 5-19 Spectral exposure per detector count vs wavelength of all data sets at 0.4 pF for Argus 1000

All of the JPC curves in Figure 5-19 have the same shape, with the JPC increasing as wavelength increases. Three of the six data sets taken at 0.4 pF have JPC curves close to one another at values starting around $1.6 \times 10^{-7} \text{Jm}^{-2}\text{nm}^{-2}\text{count}^{-1}$ at 1100 nm and changing to $1.5 \times 10^{-7} \text{Jm}^{-2}\text{nm}^{-2}\text{count}^{-1}$ at 1574 nm. These data sets are the ones taken at an exposure time setting of 0.002 s and therefore have higher numbers of detector counts in their raw data, lowering the effect of the background signal. The remaining three data sets, taken at an exposure time setting of 0.001 s, show JPC curves of almost double the magnitude as the

ones at an exposure time setting of 0.002 s, with larger variations from wavelength to wavelength.

For each JPC curve calculated, a 7th order polynomial function was fitted to the curve. The fitted polynomial is an optional method to be used as a function to convert detector counts to JPC in the field data taken with Argus 8 instead of the curves shown in Figure 5-18 and Figure 5-19 in order to remove the oscillations present in the JPC curves from wavelength to wavelength. Fitted polynomial functions for the JPC curves shown in Figure 5-14 and Figure 5-15 are shown in Figure 5-20.

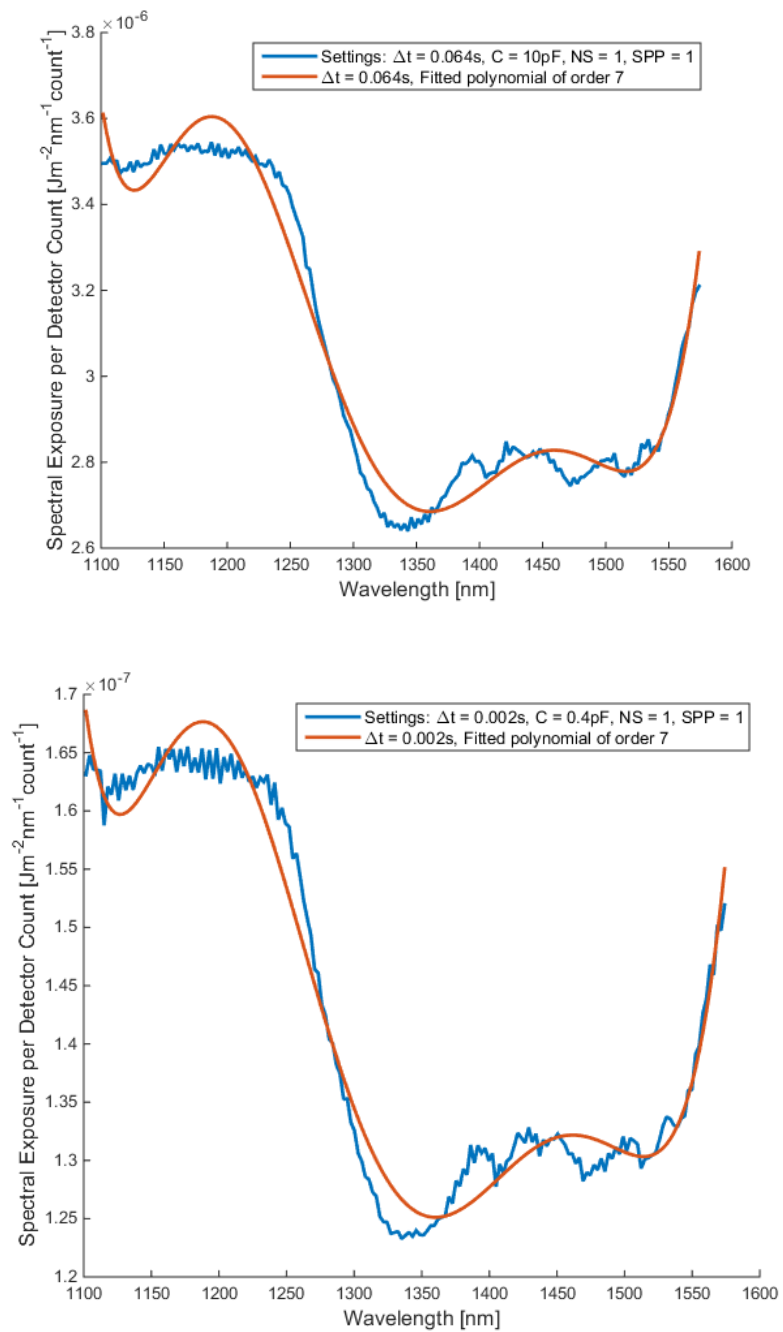


Figure 5-20 JPC curve and fitted polynomial function vs wavelength for 1 scan and 1 sample per pixel for Argus 1000. (Top: $t = 0.064\text{ s}$ and $C = 10\text{ pF}$, Bottom: $t = 0.002\text{ s}$ and $C = 0.4\text{ pF}$)

Figure 5-20 shows that in both data sets, the fitted polynomial reproduces the overall trend of the JPC curve, with some deviations from the curve itself. Increasing the order polynomial improves the fit to the JPC curve, but at the expense of adding more of the wavelength to wavelength variations seen in some data sets. The full set of fitted polynomial functions for all the data sets at each capacitor setting are shown in Figure 5-21.

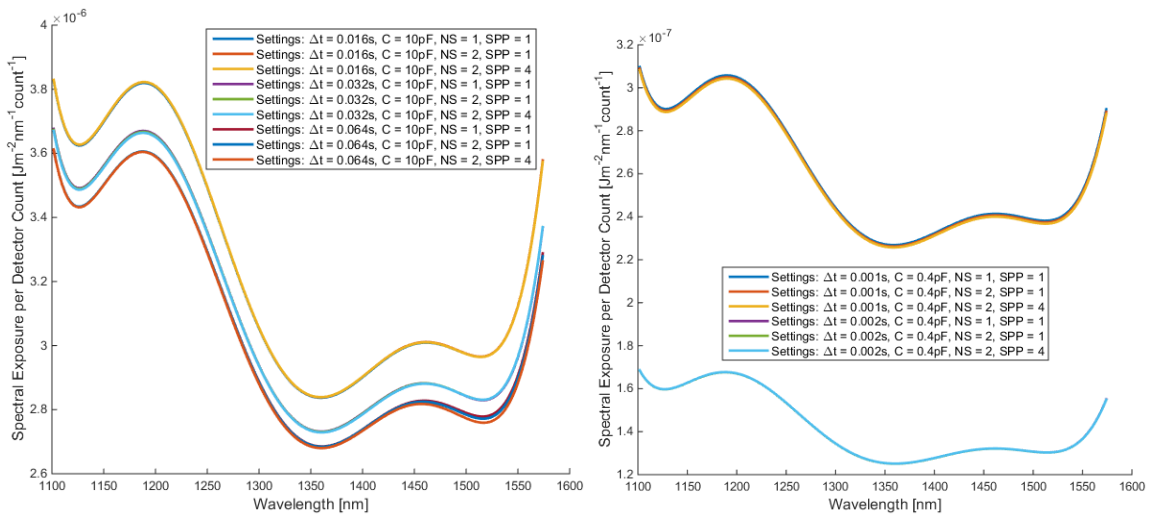


Figure 5-21 Fitted polynomial functions vs wavelength for Argus 1000. (Left: C = 10 pF, Right: C = 0.4 pF)

The polynomial functions in Figure 5-21 are similar to the JPC curves in Figure 5-18 and Figure 5-19. The functions fitted to the JPC curves at lower exposure time settings, which are most affected by the background signal, deviate furthest from the remaining polynomial functions.

The fractional uncertainties of all the data sets at each capacitor setting are shown in Figure 5-22.

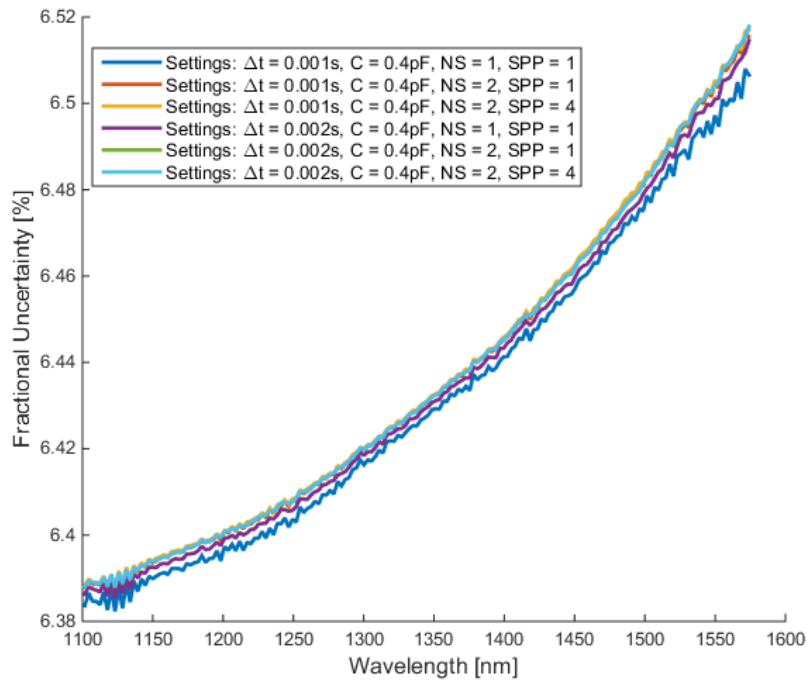
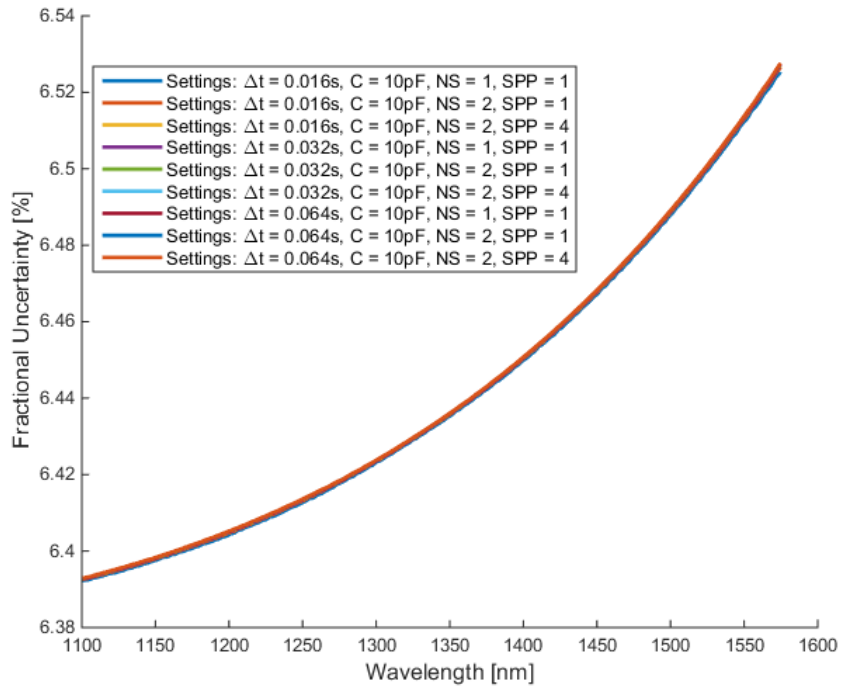


Figure 5-22 Fractional uncertainty of spectral exposure per detector count vs wavelength for Argus 1000 (Top: $C = 10 pF$, Bottom: $C = 0.4 pF$)

Figure 5-22 shows that the fractional uncertainty in the 10 pF data sets increases with wavelength and is about 6.45% for all data sets. The data sets at the 0.4 pF capacitor setting, however, have larger variations in their fractional uncertainties, especially in the region of the dead pixel shown in Figure 5-12. The magnitude of the fraction uncertainties at the 0.4 pF capacitor setting range from about 6.38% at lower wavelengths to 6.52% at higher wavelengths.

Lastly, a JPC conversion function for Argus 1000 Unit 8 was determined at both the 10 pF and 0.4 pF capacitor settings. For the 10pF setting, this was accomplished by taking the mean of all the computed JPC values at the exposure time settings of 0.032 s and 0.064 s, shown in Figure 5-18. For the 0.4 pF setting, the mean of all the computed JPC values at an exposure time setting of 0.002 s. The resulting counts to energy JPC conversion functions are shown in Figure 5-23.

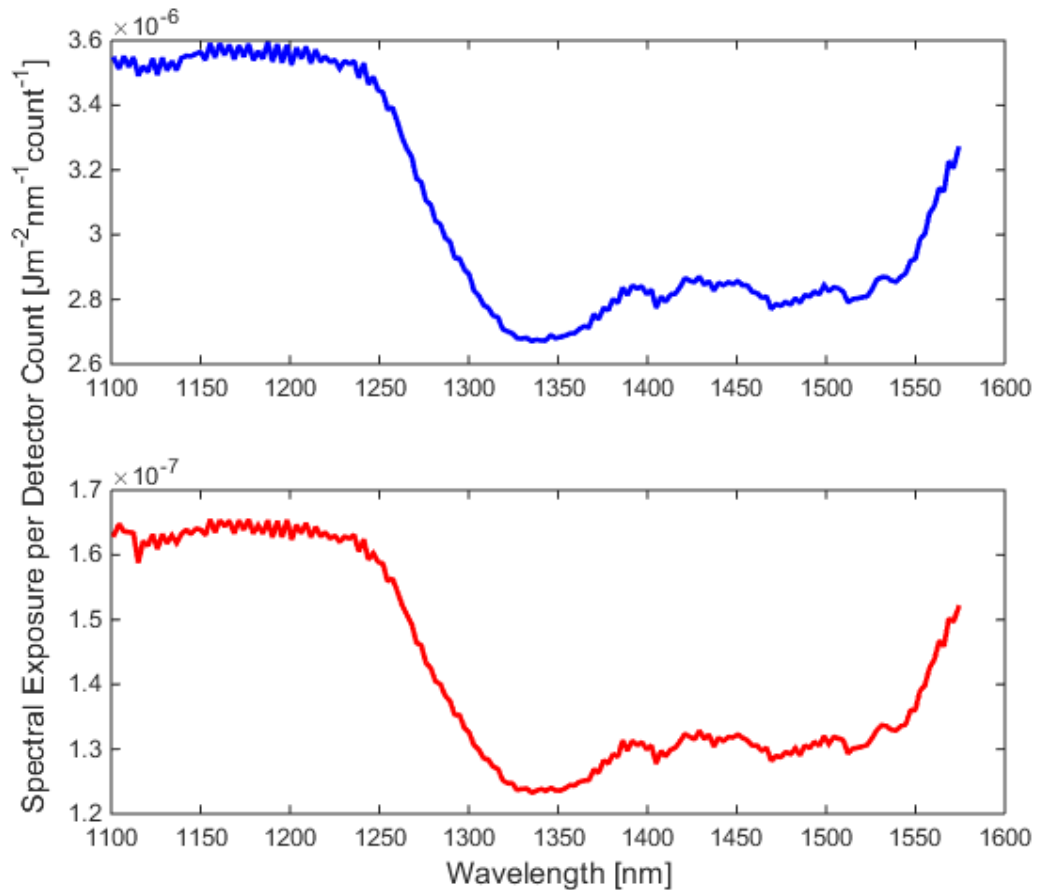


Figure 5-23 JPC conversion functions for Argus 1000 Unit 8 spectrometer at capacitor settings of 10 pF (top) and 0.4 pF (bottom)

As shown in Figure 5-23, the JPC conversion functions for both the 10 pF and 0.4 pF cases have the same shape, but differ in magnitude. The JPC conversion function at 10 pF is greater than the JPC conversion function at 0.4 pF by a factor of 21.6 on average.

5.4 FLAME-NIR Radiometric Calibration Results

Radiometric calibration of the FLAME-NIR spectrometer followed the same procedure as the radiometric calibration of Argus 1000, with some changes. Unlike Argus 1000, the FLAME-NIR spectrometer would saturate at any exposure time setting when receiving

1000 W of power from the calibrated lamp. In order to perform radiometric calibration, the power from the lamp was reduced to 250 W, 500 W, and 750 W in order to be able to acquire sufficient quantities of data at different exposure time settings. The irradiance of the lamp was assumed to scale linearly with reduced power, i.e. the irradiance curve of the lamp was scaled by the ratio of output power over 1000 W. For each data set, 1000 spectral measurements were made with the FLAME-NIR, resulting in a total of 8 data sets. 6 data sets were acquired at varying exposure times but with a lamp output power of 250 W, while the remaining data sets were acquired with a lamp output power of 500 W and 750 W respectively.

As in the radiometric calibration of Argus 1000, the background detector counts of the FLAME-NIR data were measured with the lamp turned off at a series of exposure time settings, as shown in Figure 5-24.

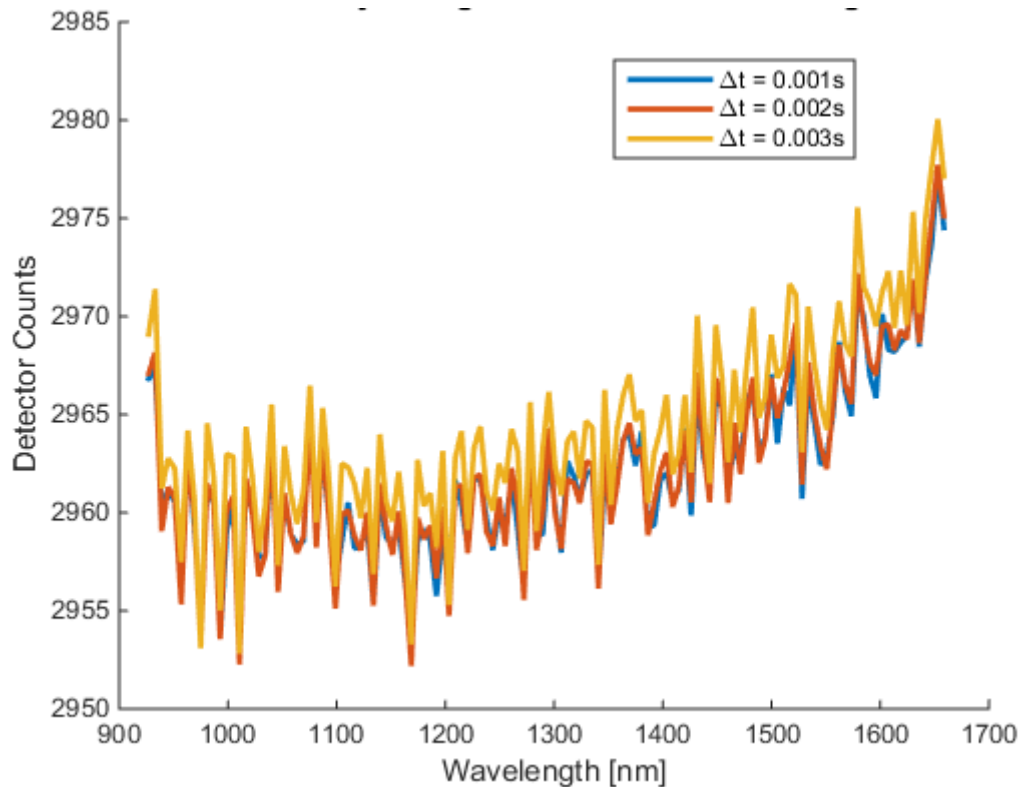
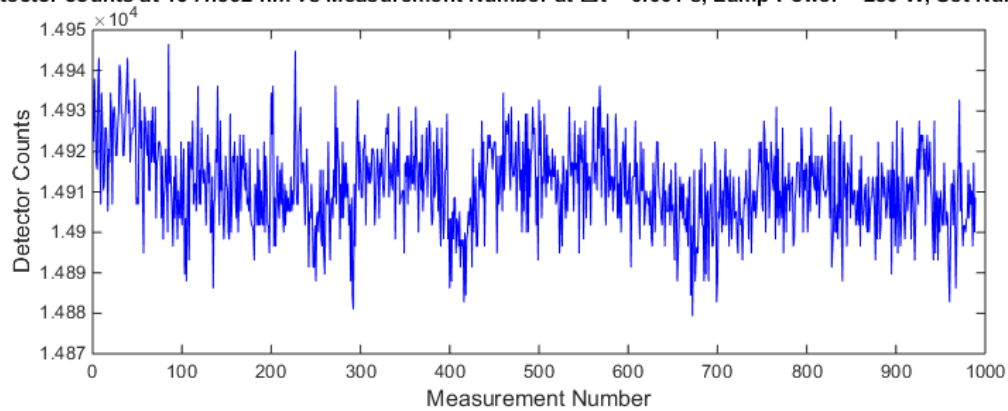


Figure 5-24 Laboratory background counts vs wavelength at three exposure time settings for FLAME-NIR radiometric calibration

The background counts in Figure 5-24 show a similar pattern to those of Argus 1000 in Figure 5-10. In both cases, changes in exposure time have little effect on the number of background counts. For the FLAME-NIR, however, the background counts appear to increase slightly as wavelength increases. Additionally, the detector counts scale of the FLAME-NIR is larger than that of Argus 1000, with the background counts being close to 3000 in the FLAME-NIR, as opposed to 50 in Argus 1000.

Additionally, variations in the number of detector counts over time at a particular wavelength in a data set were measured for the FLAME-NIR, as shown in Figure 5-25.

Detector counts at 1641.592 nm vs Measurement Number at $\Delta t = 0.001$ s, Lamp Power = 250 W, Set Number = 2



Detector counts at 1641.592 nm vs Measurement Number at $\Delta t = 0.003$ s, Lamp Power = 250 W, Set Number = 2

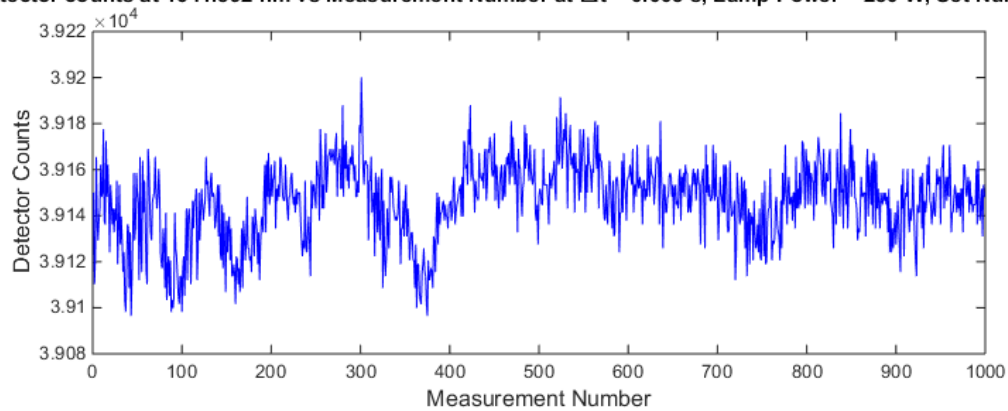
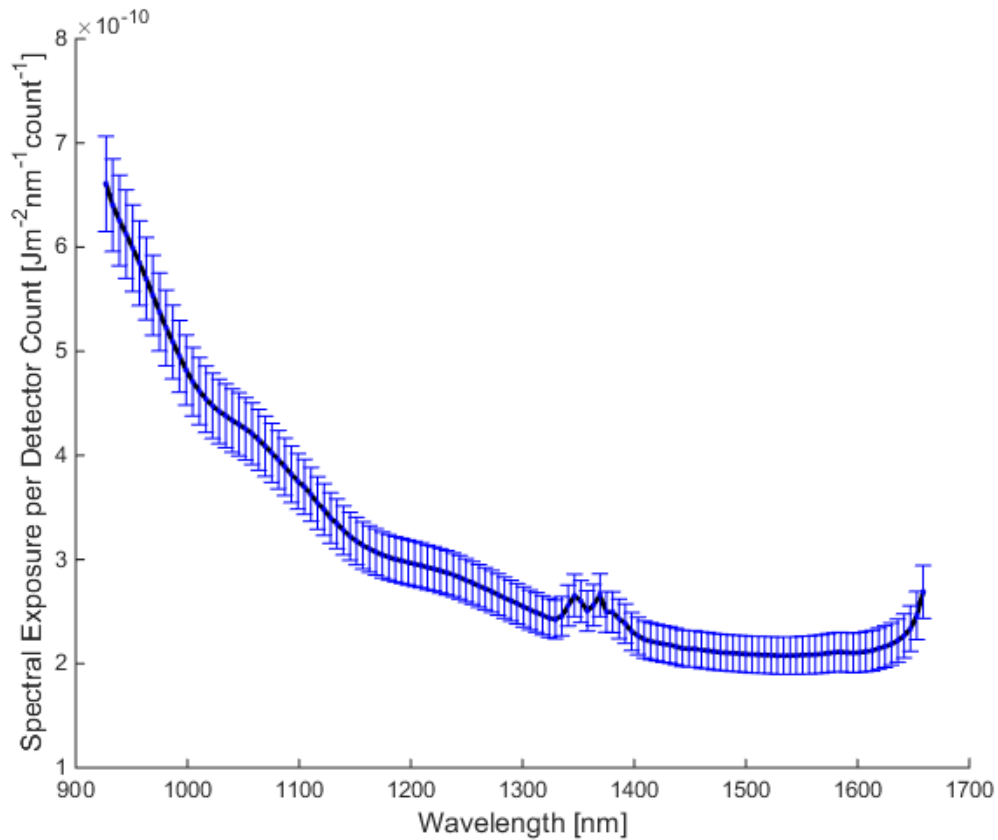


Figure 5-25 Detector counts vs measurement number for FLAME-NIR at pixel 125 (1641.592 nm)

Figure 5-25 shows that the variations of the detector counts are small and have no structure from measurement to measurement, regardless of exposure time. The deviations present in the number of detector counts from the mean are therefore likely due to random noise.

Applying the radiometric calibration equations to the detector counts allows the spectral exposure to be calculated for each data set for the FLAME-NIR, as shown in Figure 5-26 for a data set acquired at an exposure time of 1 ms with the lamp output power set to 250 W.



**Figure 5-26 Spectral exposure per counts (JPC) vs wavelength for FLAME-NIR
with $\Delta t = 0.001$ s and $P = 250$ W**

Figure 5-26 shows that the spectral exposure received by the FLAME-NIR decreases as wavelength increases, with two small peaks present in between 1300 nm and 1400 nm and a slight increase in at the edge of the spectrum. The overall trend is consistent with theoretical expectations. Uncertainties were calculated at each wavelength and are under 10% for all wavelengths.

The effect of changing the lamp output power on the mean JPC curves was determined by plotting the calculated JPC curves vs wavelength for all the data sets at a particular exposure time, as shown in Figure 5-27.

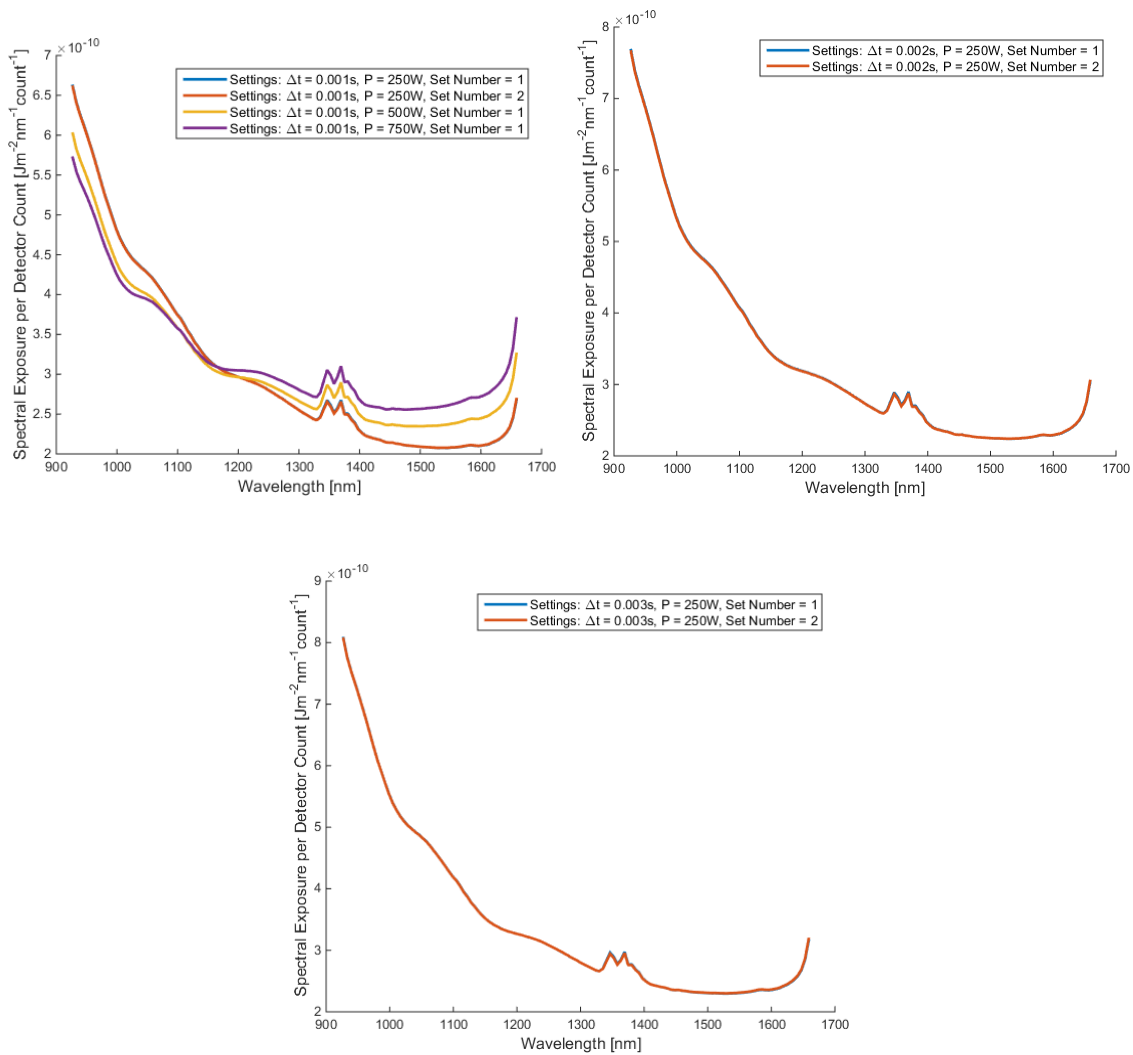


Figure 5-27 Spectral exposure per count vs wavelength for FLAME-NIR. (Top left: $t = 0.001$ s, Top right: $t = 0.002$ s, Bottom: $t = 0.003$ s)

Figure 5-27 shows that the JPC curve is almost identical for all data sets at exposure time settings of 2 ms and 3 ms. At an exposure time setting of 1 ms, variations are present across data sets acquired using different lamp output power values. The JPC curve has greater magnitude for lower lamp output power at wavelengths ranging from 927 nm to about 1160 nm and lower magnitude for lower lamp output power at wavelengths greater than 1160

nm. The largest difference in JPC value occurs between the data sets acquired with lamp output powers of 250 W and 750 W at a wavelength of 1658.7 nm and is equal to 38.4%.

Grouping the mean JPC curves by output lamp power allows the effect of the instrument exposure time setting to be observed, as shown in Figure 5-28 for an output power of 250 W.

W.

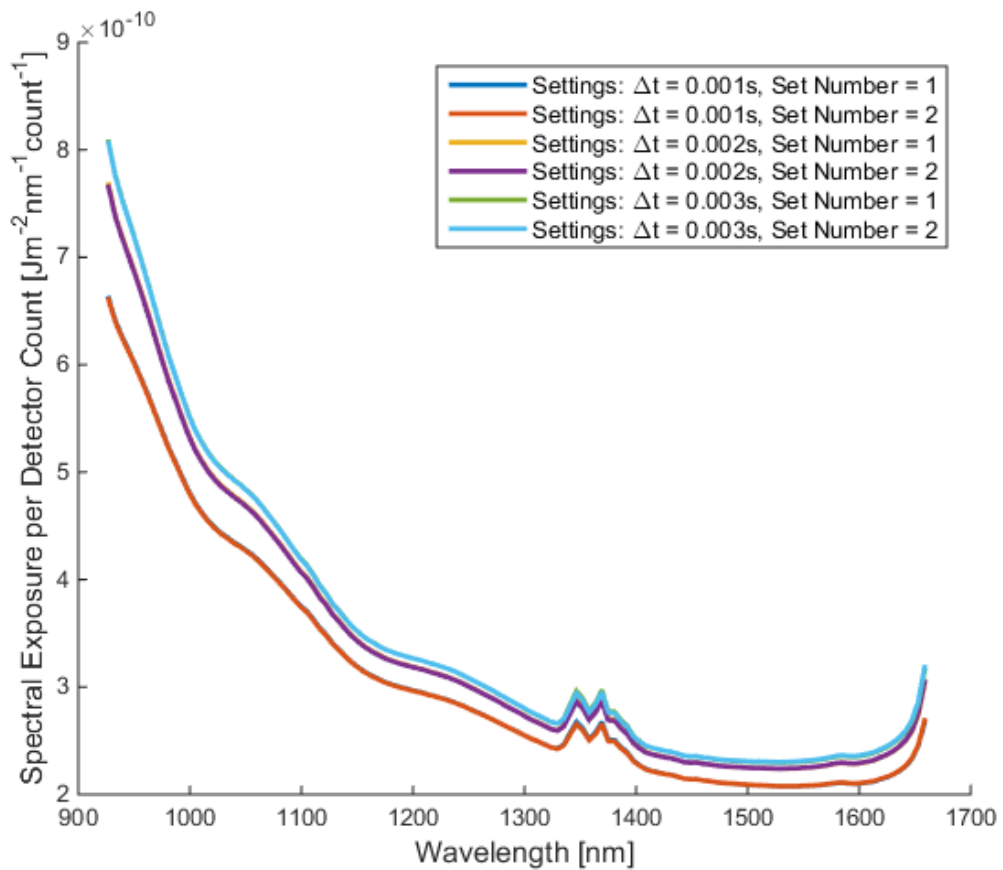


Figure 5-28 Spectral exposure per count vs wavelength for FLAME-NIR for P = 250 W

The mean JPC curves shown in Figure 5-28 increase slightly as the exposure time value increase, with the largest difference present at lower wavelengths. Additionally, all four

data sets acquired at exposure time settings of 2 ms and 3 ms are very close to one another.

All JPC curves, however, have the same shape regardless of exposure time setting.

The full range of computed JPC values can be visualized by plotting the mean JPC curve of each data set as a function of wavelength, as shown in Figure 5-29.

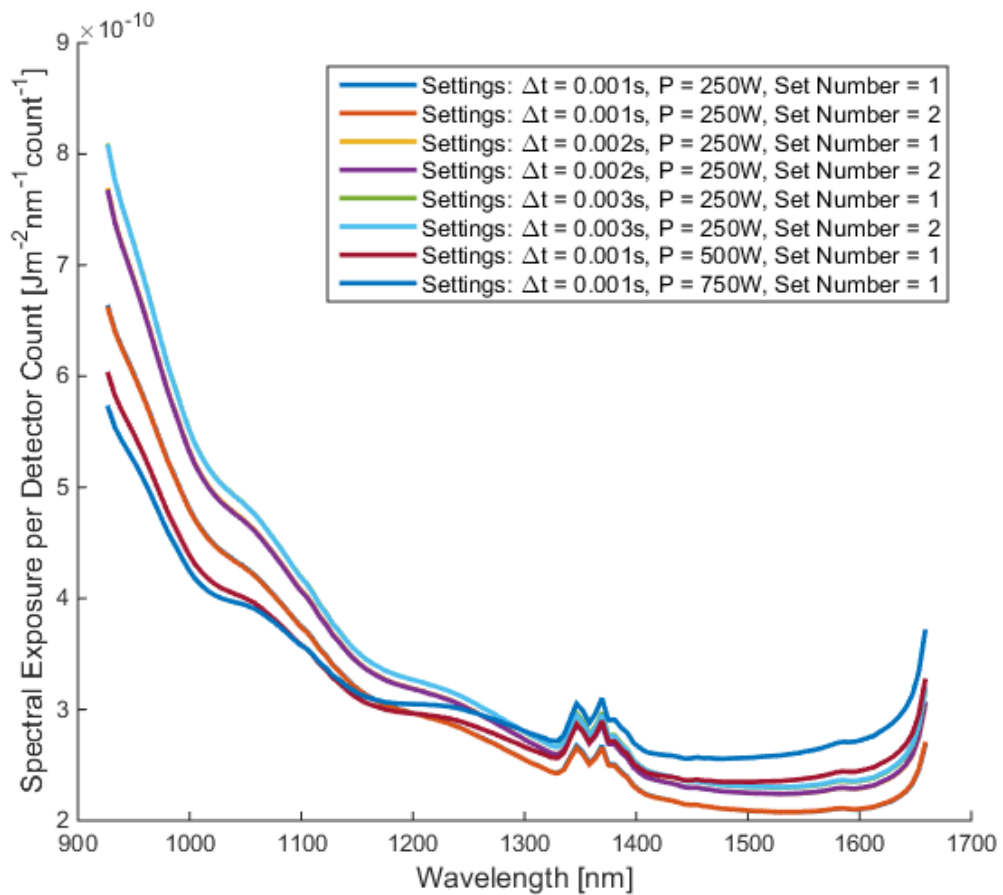


Figure 5-29 Spectral exposure per count vs wavelength for FLAME-NIR for all data sets

Figure 5-29 is similar to Figure 5-28, but with the two data sets acquired at lamp output power values of 500 W and 750 W added. At these power levels, the FLAME-NIR would saturate at any exposure time settings greater than 1 ms, so the effect of changing exposure

time at these power levels could not be observed. All the JPC curves in Figure 5-29 have the same shape, but differ in magnitude, with the largest differences occurring at the edges of the spectra.

The fractional uncertainties of all the mean JPC curves were calculated and are shown in Figure 5-30.

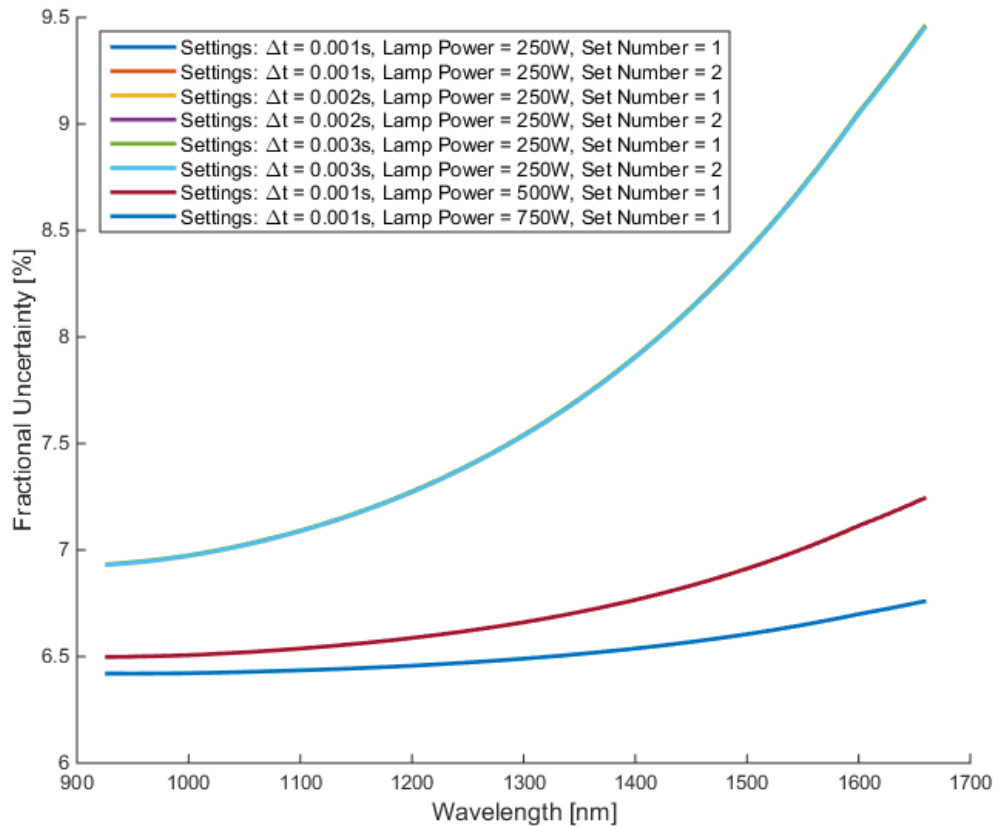


Figure 5-30 Fractional uncertainty of spectral exposure per detector count vs wavelength for FLAME-NIR

The fractional uncertainties for the JPC curves shown in Figure 5-29 are shown in Figure 5-30 and in all cases increase as the wavelength increases. The fractional uncertainties of

all the data sets acquired with a lamp output power of 250 W range from just under 7% at lower wavelengths to 9.5% at higher wavelengths. The fractional uncertainties of data sets acquired at lamp output power values of 500 W and 750 W are lower than those acquired at 250 W.

Lastly, a JPC conversion function was computed for the FLAME-NIR using the same approach as for Argus 1000. The resulting JPC conversion function is shown in Figure 5-31.

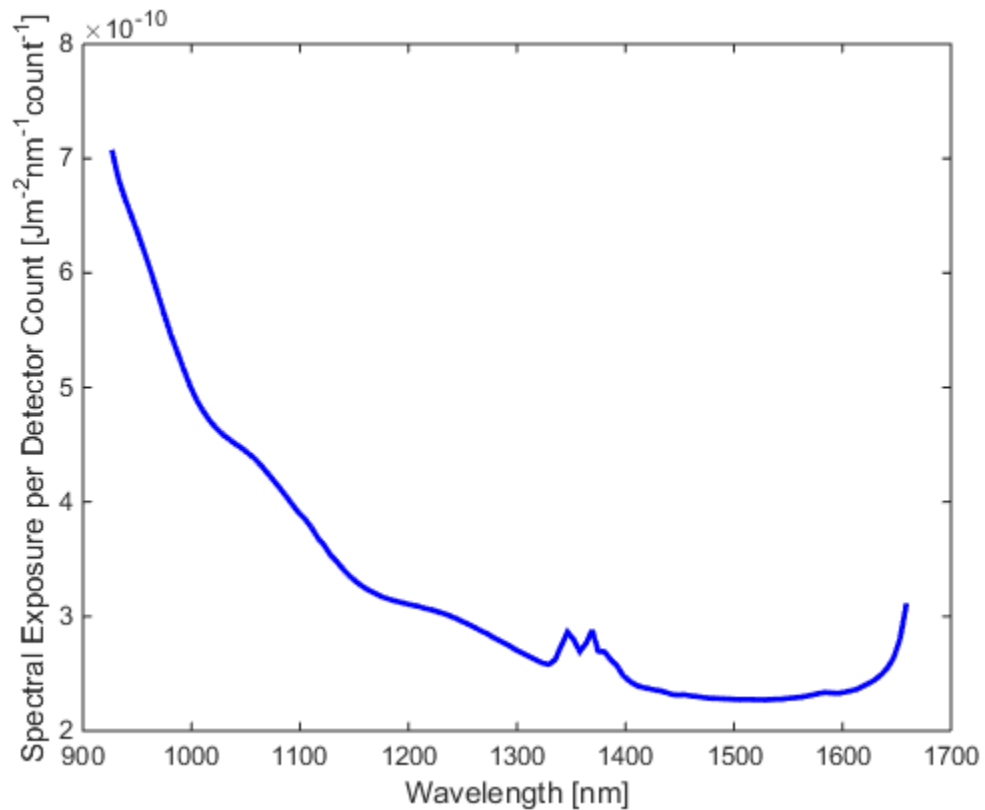


Figure 5-31 JPC conversion functions for FLAME-NIR spectrometer

The JPC conversion function shown in Figure 5-31 is the mean of all the JPC functions computed for each measurement of each data set.

5.5 Radiometric Calibration Conclusion

The radiometric calibration of Argus 1000 Unit 8 and FLAME-NIR spectrometers was conducted using a calibrated lamp, off-axis parabolic mirror for collimation, and the NIR spectrometers themselves. Data sets were acquired at a series of instrument settings, organized by exposure time setting and capacitor setting in the case of Argus 1000 and by exposure time setting and lamp output power in the case of the FLAME-NIR.

For Argus 1000, spectral exposure per detector count vs wavelength curves were determined for each data set and found to match closely with one another for all data sets at the 10 pF capacitor setting. For the 0.4 pF capacitor setting, the spectral exposure per detector count vs wavelength curves were clustered into two regions based on the exposure time setting. The uncertainty in all data sets was around 6.45%. Two detector count to energy conversion functions were determined for Argus 8, one for data sets taken at a capacitor setting of 10 pF and another for data sets taken at a capacitor setting of 0.4 pF.

For the FLAME-NIR, spectral exposure per detector count versus wavelength curves were determined for each data set and found to closely match in shape, but differ in magnitude, particularly at higher lamp output power levels. A detector count to energy conversion function was determined for the FLAME-NIR to be used for all data sets.

6 Validation of the Coastline Detection Algorithm Using a UAV Campaign

Validation of the coastline detection algorithm for NIR spectral data required a method of data acquisition comparable to the spaceborne Argus spectral data used, but with greater experimental control and additional validation sources. An air campaign provided a low cost method of acquiring this data in a controlled experiment in order to validate the geolocation assessment algorithm. In order to conduct coastline detection validation, an airborne campaign was undertaken in early November 2016 to acquire NIR spectral data over coastal areas. The purpose of the airborne validation campaign was to determine that the coastline detection algorithm provided results, i.e. the goal was to determine whether the inflection point method would detect the same number of coastlines as expected from the geolocation of the instrument.

6.1.1 Airborne Validation Campaign Platform

The November 2016 airborne validation campaign was the second airborne validation campaign conducted for validation of the coastline detection algorithm. The payload system consisted of an Ocean Optics FLAME-NIR spectrometer, a Raspberry Pi camera module system, a Global Positioning System module (GPS), and attitude sensors, integrated into a UAV.

The aircraft flown was a DJI Flamewheel F550, with the FLAME-NIR spectrometer and camera mounted pointing in the nadir direction as payloads. The Flamewheel F550 was a battery powered vertical take-off and landing (VTOL) UAV with 6 coaxial motors with a total mass of 2300g, including the payloads and landing gear. The GPS, spectrometer, and camera module were all integrated into a single mount and linked together to a Raspberry Pi 3 computer, which served to run each system and store the data for post processing, as shown in Figure 6-1.

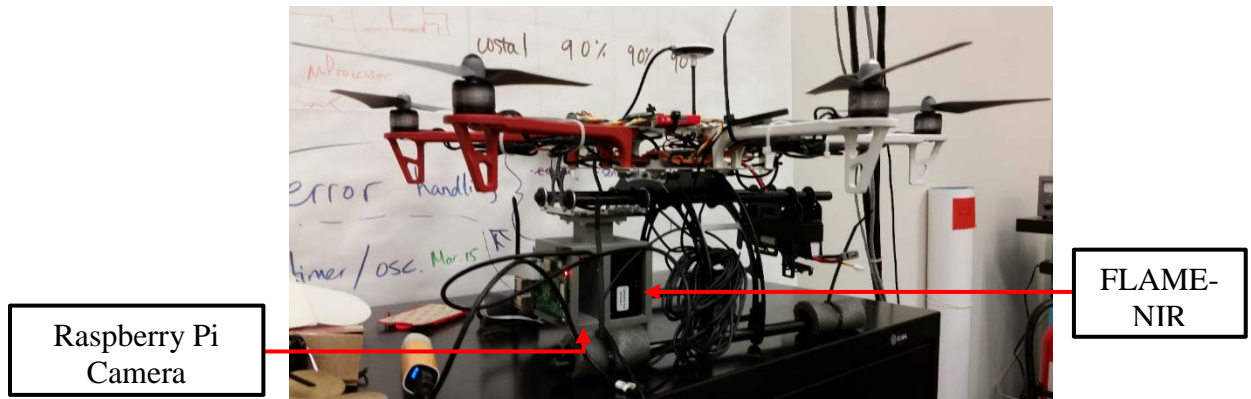


Figure 6-1 UAV system consisting of DJI Flamewheel F550 with mounted FLAME-NIR spectrometer and Raspberry Pi board and camera module payload

The forward direction of the UAV was defined as the direction between the red UAV arms, as shown in Figure 6-1. Additionally, the camera and spectrometer were mounted below these arms on the landing gear and on the forward side of the UAV. The system was balanced by mounting the battery for the UAV flight on the gear and on the opposite side from the payload and mount. Sliding the battery mount along the rails of the landing gear allowed the UAV to be properly balanced prior to flight.

The FLAME-NIR spectrometer was fitted with an Ocean Optics 74-DA collimating lens at the entrance slit for gathering incident light. This lens had a focal length of 5 mm and a diameter of 10 mm, corresponding to a field of view of $5^\circ \times 2.5^\circ$ due to the slit size of 1 mm \times 25 μm . Optical imagery was gathered using the Raspberry Pi camera module version 2.1, which consisted of a sensor with a rectangular $62.2^\circ \times 48.8^\circ$ field of view with a focal length of 3.04 mm.

In order to use the camera and spectrometer data for coastline detection analysis, the location of the spectrometer FOV relative to the camera FOV needed to be determined. This was accomplished by analyzing the geometry of the camera and spectrometer in the mounting system, as shown in Figure 6-2.

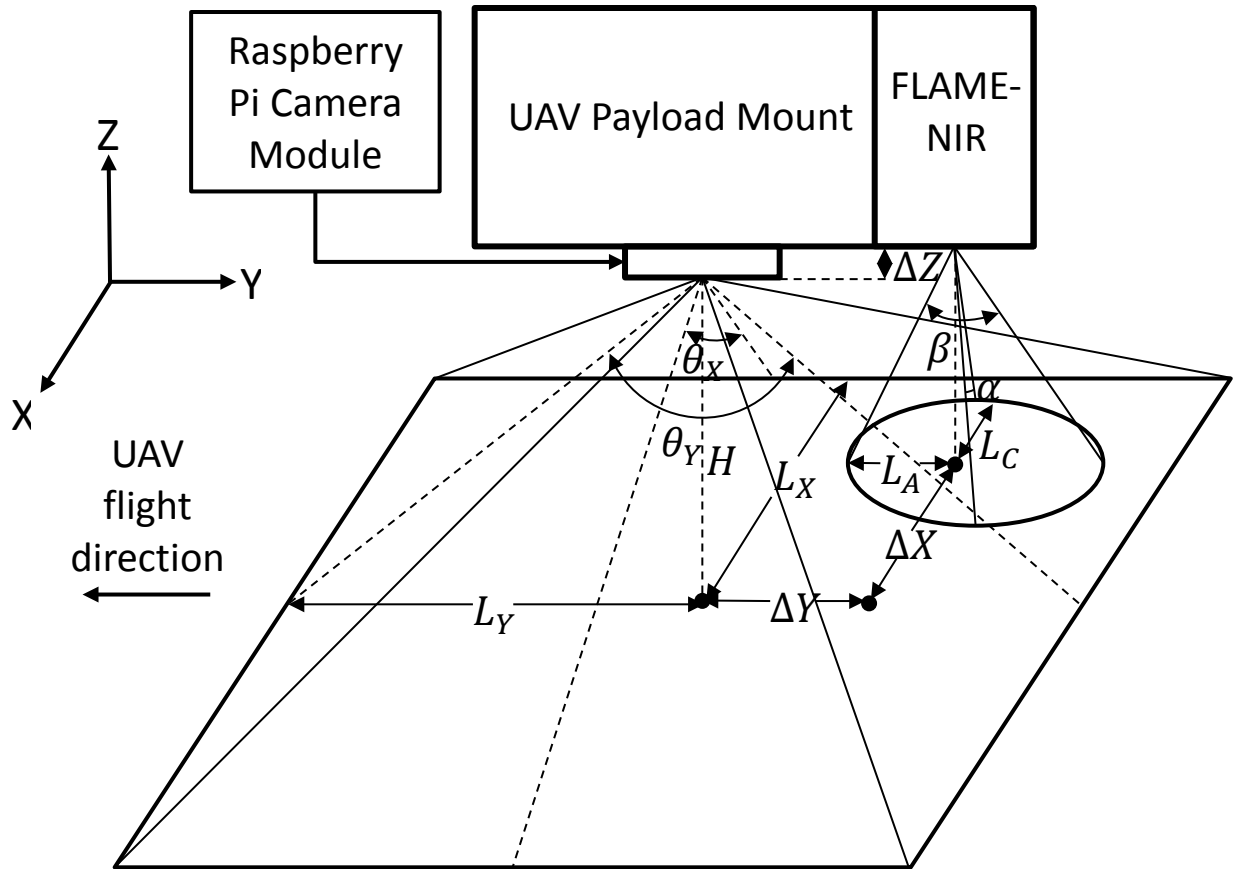


Figure 6-2 Side view of FLAME-NIR spectrometer and Raspberry Pi camera payload geometry

Figure 6-2 shows the Raspberry Pi camera module and FLAME-NIR spectrometer along with their respective rectangular and elliptical fields of view. The centre of the field of view of the FLAME-NIR is offset from the centre of the camera image by offsets ΔX , ΔY , and ΔZ , which are measured values from the design of the mounting system. Angles θ_X and θ_Y are the Raspberry Pi field of view angles of 62.2° and 48.8° respectively, while α and β are the spectrometer field of view angles of 2.5° and 5° respectively due to the 74-DA lens. The height H of the camera above the ground is used to determine the lengths on the ground imaged by both the camera and spectrometer lenses in each direction due to the non-

uniform fields of view. The lengths L_Y and L_X on the ground imaged by the camera in the along-flight and cross-flight directions respectively are given by

$$\begin{aligned}L_Y &= H \tan\left(\frac{\theta_Y}{2}\right) \\L_X &= H \tan\left(\frac{\theta_X}{2}\right)\end{aligned}\tag{12}$$

Similarly, the lengths L_A and L_C on the ground observed by the spectrometer in the along-flight and cross-flight directions respectively are given by

$$\begin{aligned}L_A &= (H + \Delta Z) \tan\left(\frac{\beta}{2}\right) \\L_C &= (H + \Delta Z) \tan\left(\frac{\alpha}{2}\right)\end{aligned}\tag{13}$$

The number of pixels present in the camera is different in the horizontal and vertical directions of each image, which along with the non-uniform field of view of the camera results in rectangular pixels, as shown in Figure 6-3.

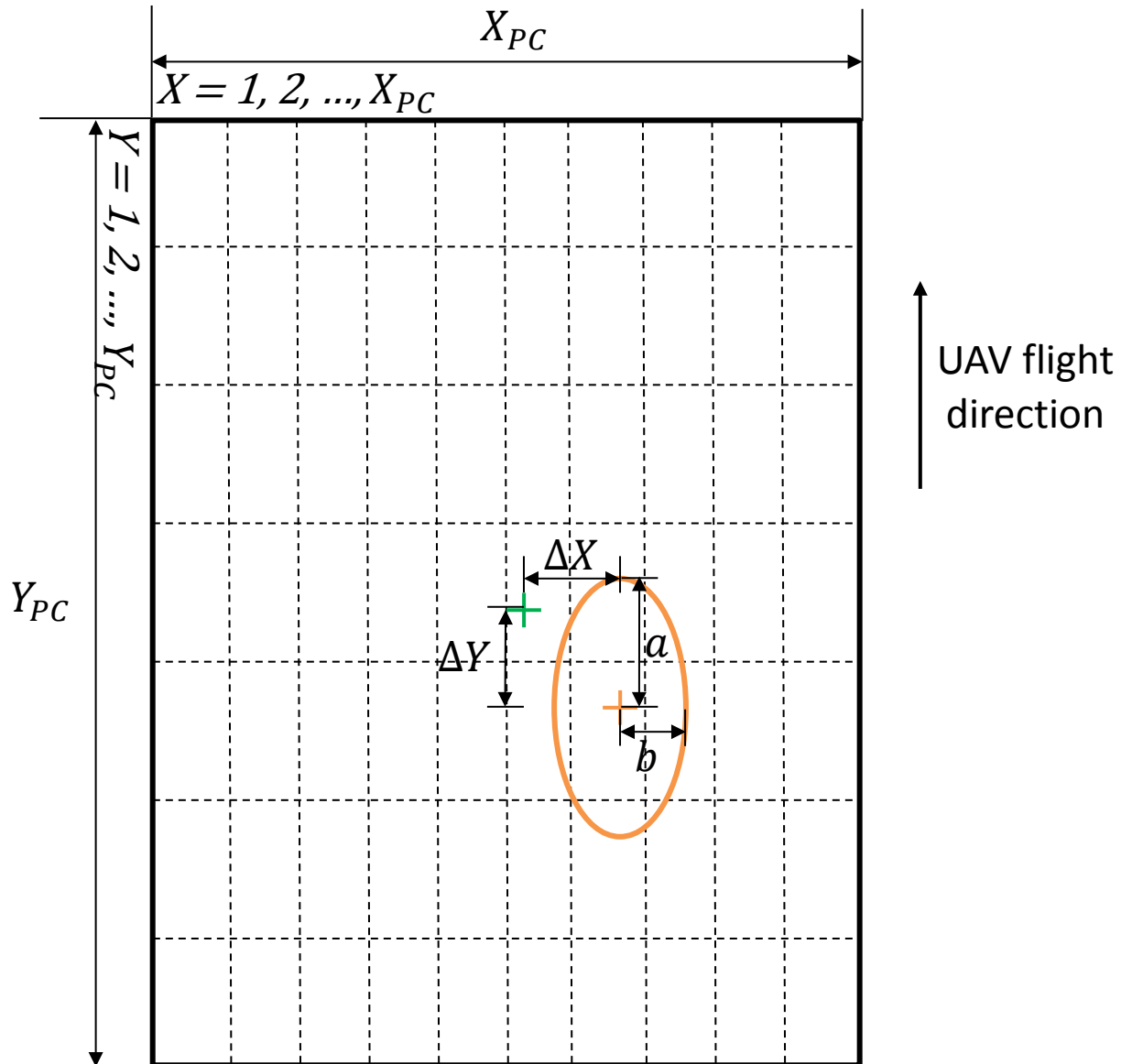


Figure 6-3 Top view of FLAME-NIR spectrometer (orange) and Raspberry Pi camera payload geometry (not all pixels are shown)

X_{PC} and Y_{PC} , shown in Figure 6-3, are the number of pixels in the image in the horizontal (x) and vertical (y) directions respectively. The pixels themselves are indexed from the top

left of the image. Lengths L_Y and L_X are used to determine the mean distance imaged by each pixel of the camera. These distances are given by

$$\begin{aligned} D_{PY} &= \frac{2L_Y}{Y_{PC}} \\ D_{PX} &= \frac{2L_X}{X_{PC}} \end{aligned} \tag{14}$$

D_{PX} and D_{PY} are the mean distances imaged by each pixel in the camera image. The coordinates (X_B, Y_B) of the boresight of the FLAME-NIR field of view in the image frame are offset from the centre of the image and are given by

$$\begin{aligned} X_B &= \frac{X_{PC}}{2} + \frac{\Delta X}{D_{PX}} \\ Y_B &= \frac{Y_{PC}}{2} + \frac{\Delta Y}{D_{PY}} \end{aligned} \tag{15}$$

The instantaneous field of view of the FLAME-NIR is in the shape of an ellipse with semi-major axis a and semi-minor axis b . These parameters are given by

$$\begin{aligned} a &= \frac{\Delta Y}{D_{PY}} \\ b &= \frac{\Delta X}{D_{PX}} \end{aligned} \tag{16}$$

In the image frame, the field of view itself is described by an ellipse to centre coordinates (X_B, Y_B) and rotated by $\frac{\pi}{2}$ so that the semi-major axis is aligned with the y-axis of the image.

Mathematically it is modelled by the equation

$$\frac{(Y - Y_B)^2}{a^2} + \frac{(X - X_B)^2}{b^2} = 1 \quad (17)$$

Values of X ranging from $X - a$ to $X + a$ are used to determine corresponding values of Y and generate the instantaneous field of view of the FLAME-NIR in the image frame.

6.1.2 Airborne Validation Campaign Procedure

The data acquisition process consisted of flying the UAV back and forth over coastal areas, with FLAME-NIR spectral measurements and optical images acquired at regular intervals. Spectral measurements were acquired at an exposure time setting of 750 ms in order to provide a clear signal difference between measurements made over land and water, while being as close to the spaceborne data exposure time setting of 1024 ms as possible. Further increases of the exposure time setting of the airborne experiment would make it difficult to acquire sufficient measurements for applying the coastline detection algorithm. A white panel was used to test suitable spectrometer exposure time settings prior to the airborne campaign. This process involved setting the white panel on the ground and moving the spectrometer over it multiple times at differing exposure time settings in order to determine which settings provided strong signals without saturating the instrument detector.

The sites selected for data acquisition were Chaffeys Locks, Ontario, and the northern shore of Little Skunk Lake, located near Bancroft, Ontario, as shown in Figure 6-4 [70], [71].

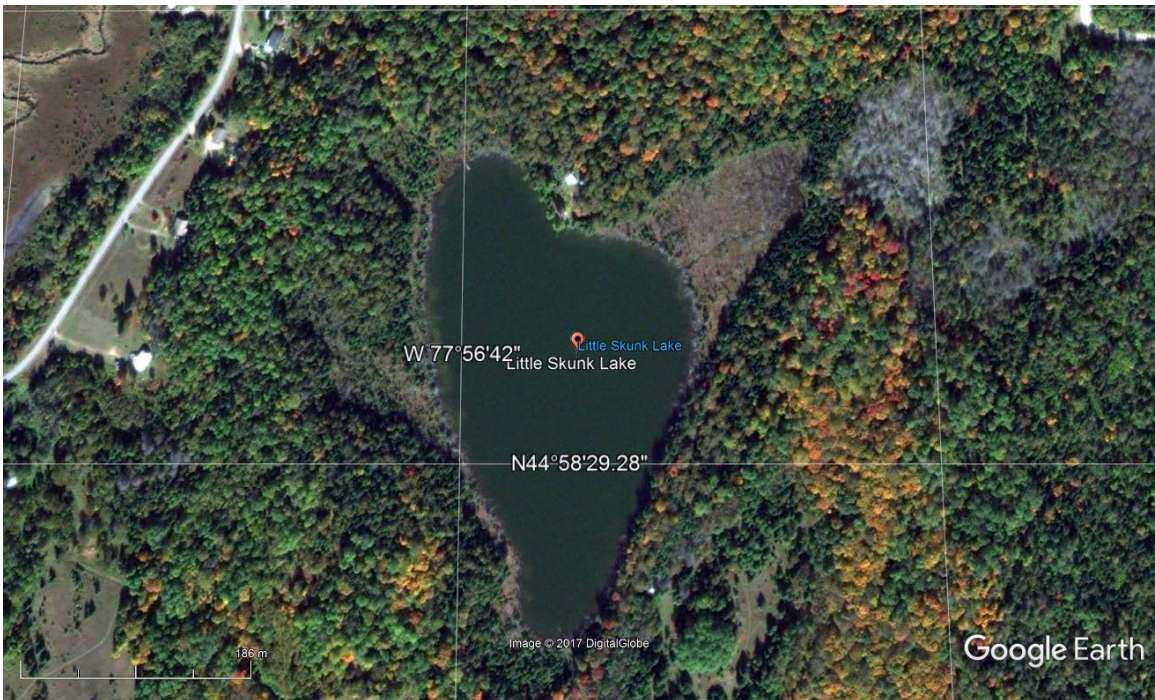


Figure 6-4 Airborne validation campaign data collection sites: Chaffeys Locks, ON (Top, [70]) and Little Skunk Lake, ON (bottom, [71])

Multiple data sets were acquired at each data collection site, with one spectrometer measurement being made followed by a corresponding camera image being taken. At the start of acquisition of each data set, the UAV needed to acquire GPS satellite signals before it would begin its flight. However, acquisition of spectral data and camera images would begin the moment the UAV was activated, resulting in a series of images and spectra that would not be suitable for processing. In order to identify these data sets, the UAV was initially stationed on the white panel used to set instrument settings as a launch pad. Camera images whose entire field of view showed the white panel only were therefore used to identify the actual start and end of data acquisition during the flight.

For each data collection site, all the images acquired using the Raspberry Pi camera module were post-processed to form orthoimages, which are images that are based on an orthogonal projection rather than the perspective projection with which they were taken [72]. The process of forming an orthoimage is called orthorectification and requires a camera model and a digital terrain model. The orthoimages are then stitched together to form an orthomosaic, which adjusts the orthoimages into one large map with a common scale, thereby allowing relative distances to be measured between any points. Orthomosaics were generated using Agisoft software, which searched the images for features that were present in multiple images. The size and orientation of these features was used to calculate the positions of the camera in a common reference frame. Images were then rotated and scaled prior to being stitched together.

In order to generate an orthomosaic with the correct absolute scale, features of known size need to be present in multiple images. In order to accomplish this, at each site a series of 5m stadia rods were set up for ground control, as shown in Figure 6-5.



Figure 6-5 Raspberry Pi camera image containing four stadia rods acquired over Chaffeys Locks, ON

Figure 6-5 shows the placement of four stadia rods at the Chaffeys Locks site. Since the length of the stadia rods was known, the orthomosaic was generated with the appropriate scale so that lengths of the stadia rods on it were correct. The point of intersection of three of the stadia rods in Figure 6-5 was also used to define the coordinate system of the orthomosaic. Lastly, a log file was generated that provided the coordinates of the centre of

each image in the orthomosaic coordinate system and the rotation angles applied to the image to stitch it into the orthomosaic.

6.1.3 Airborne Validation Campaign Results

A total of eight data sets were collected during the airborne validation campaign, six at Chaffeys Locks and two at Little Skunk Lake. The total number of spectral measurements and camera images taken for each data set, along with the number of measurements and images used in the coastline detection analysis are shown in Table 6-1.

Table 6-1 Airborne validation campaign data set properties

Data Collection Site	Data Set Number	Total Number of Spectra/Images	Spectra/Images Used for Coastline Detection
Chaffeys Locks	0	94	None
	1	142	39
	2	88	51
	3	114	59
	4	107	63
	5	130	74
Little Skunk Lake	6	273	197
	7	398	143

While many individual images and their related spectra are not used, as shown in Table 6-1, due to their acquisition prior to the start or end of the flight, sufficient overlap between the images remains in order to form the orthomosaics. Figure 6-6 shows the orthomosaics formed using data sets 1 through 5 acquired over Chaffeys Locks and data sets 6 and 7 acquired over Little Skunk Lake.

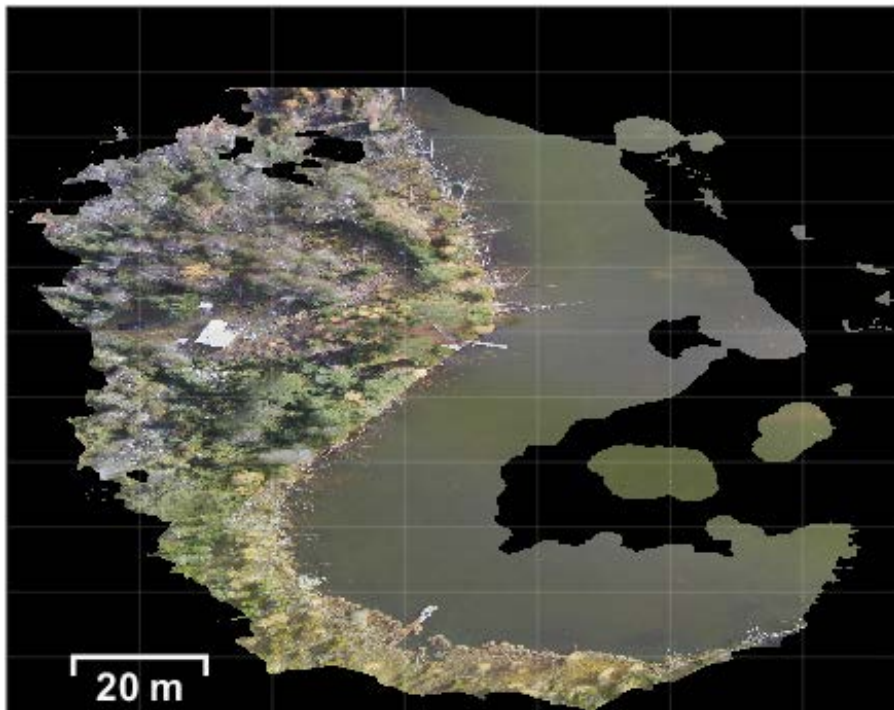
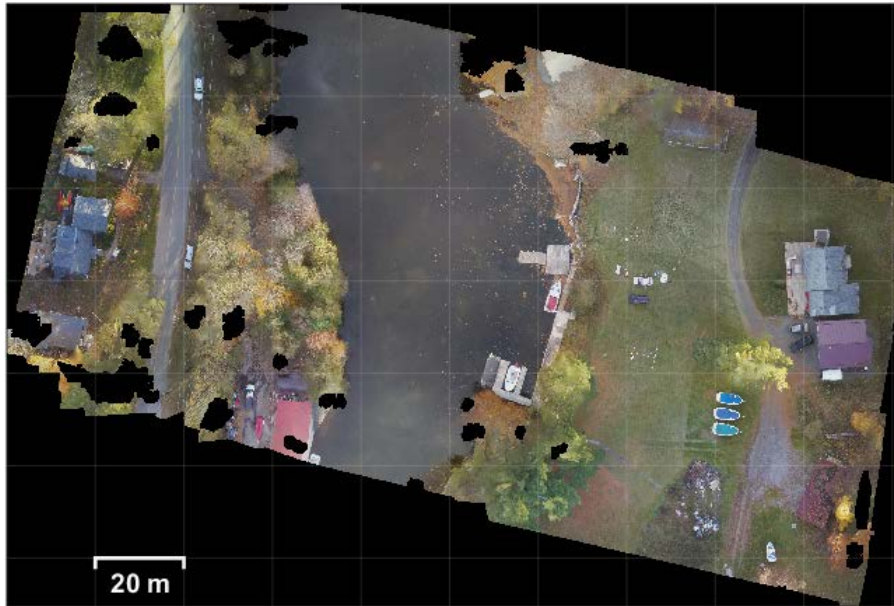


Figure 6-6 Orthomosaic composed of Raspberry Pi images taken over Chaffeys Locks, ON (top) and Little Skunk Lake, ON (bottom)

As shown in Figure 6-6, the orthomosaic formed using the Chaffeys Locks data sets contains two clearly visible coastlines and the one formed using the Little Skunk Lake data set shows one continuous coastline. Additionally, the stadia rods are visible in two locations on the right portion of the Chaffeys Locks orthomosaic and to the right of the white structure in the Little Skunk Lake orthomosaic. The rods are present in two locations in the Chaffeys Locks orthomosaic since the starting location of the aircraft was changed as data sets were acquired over Chaffeys Locks and the rods were therefore moved to a spot near the take-off location for checking purposes. The orthomosaic is also free of gaps in its central locations, where the coastline crossings occurred. This can be visualized by plotting the spectrometer fields of view and image boundaries for each data set, as shown for Chaffeys Locks data set 1 in Figure 6-7.



Figure 6-7 Orthomosaic for data sets acquired over Chaffeys Locks, ON, with spectrometer field of view ellipses (red) and corresponding Raspberry Pi image boundaries (blue) overlaid for data set 1

As shown in Figure 6-7, the FLAME-NIR field of view ellipses are all located in the central portions of the orthomosaic. The size of each field of view ellipse depends on the height of the aircraft, i.e. as the aircraft increases in height, so does the size of the ellipse. Additionally, the size of the Raspberry Pi camera image also increases with height, as expected. The flight began and ended on the top bank of the orthomosaic, near the stadia rods, where the ellipses are smallest. By visual inspection, four coastline crossings are expected to be detected in the coastline detection analysis of this data set. Closed coastline polygons, in the orthomosaic coordinate system, are extracted from each orthomosaic and used to find the expected coastline crossing coordinates, using the same approach as in the spaceborne data analysis.

The coastline detection algorithm was tested on all the data sets acquired over Chaffeys Locks and Little Skunk Lake. The distances between the expected coastline crossing locations from the geolocation process and the detected coastline locations in the spectrometer data were used to determine the effectiveness of the algorithm. The results of the coastline detection algorithm are shown in Table 6-2.

Table 6-2 Coastline detection results for FLAME-NIR airborne campaign with $1 \times 10^{-5} \text{ Wm}^{-2}$ irradiance detection threshold

Data Set ID	Crossing ID	Expected Crossing Coordinates [m]	Detected Crossing Coordinates [m]	Distance to Coastline [m]	UAV Height [m]	Angular Error [°]	Crossing Angle [°]
CL1	1A	(927.42, 1008.08)	(923.78, 1009.00)	3.75	49.57	4.33	57.88
	1B	(928.61, 1004.74)	(914.20, 1003.10)	14.50	44.07	18.21	53.47
	1C	(982.02, 1000.69)	(996.09, 999.38)	14.14	11.35	51.25	35.98
	1D	(982.32, 1000.97)	(981.98, 1001.01)	0.34	18.27	1.06	77.89
CL2	2A	(981.62, 999.98)	(980.23, 999.90)	1.39	16.93	4.69	7.65
	2B	(981.96, 1002.08)	(988.29, 1002.65)	6.35	22.13	16.01	43.35
CL3	3A	(928.16, 1006.66)	(928.43, 1006.69)	0.27	60.49	0.26	82.85
	3B	(931.25, 1001.26)	(917.04, 1001.74)	14.22	40.11	19.51	82.73
	3C	(978.65, 1008.69)	(989.18, 1006.90)	10.68	58.31	10.38	87.03
	3D	(979.87, 997.77)	(980.60, 997.71)	0.73	25.77	1.63	84.27
CL4	4A	(931.39, 1000.32)	(929.54, 1000.71)	1.90	62.48	1.74	13.85
	4B	(934.80, 990.49)	(951.29, 986.28)	17.01	62.15	15.31	45.98
	4C	(980.00, 988.06)	(966.75, 991.93)	13.80	61.46	12.66	84.38
	4D	(980.52, 980.20)	(995.21, 976.04)	15.27	56.93	15.01	85.74
CL5	5A	(928.27, 1005.97)	(927.03, 1005.52)	1.32	50.04	1.51	60.97

Data Set ID	Crossing ID	Expected Crossing Coordinates [m]	Detected Crossing Coordinates [m]	Distance to Coastline [m]	UAV Height [m]	Angular Error [°]	Crossing Angle [°]
	5B	(933.92, 992.25)	(948.00, 987.64)	14.82	49.38	16.71	46.13
	5C	(934.54, 988.14)	(928.62, 987.84)	5.93	49.64	6.81	71.07
	5D	(934.75, 989.42)	(945.56, 990.97)	10.92	48.99	12.57	83.02
	5E	(973.43, 994.46)	(990.06, 995.69)	16.67	47.74	19.25	76.48
	5F	(978.75, 979.01)	(987.61, 977.23)	9.03	48.64	10.52	79.87
	5G	(979.75, 996.98)	(987.12, 995.32)	7.56	48.18	8.92	47.69
	5H	(980.82, 980.68)	(996.12, 978.62)	15.44	47.69	17.94	86.39
LSL6	6A	(1010.80, -1037.85)	(1000.82, -1014.66)	25.25	56.48	24.08	77.83
	6B	(1013.98, -1029.65)	(1011.11, -1025.32)	5.20	57.62	5.15	56.54
	6C	(1026.34, -1008.48)	(1025.62, -1008.24)	0.75	50.30	0.86	72.03
	6D	(1032.29, -980.39)	(1030.01, -980.84)	2.32	60.29	2.20	82.73
	6E	(1032.69, -1000.45)	(1015.45, -997.63)	17.47	52.76	18.32	75.74
	6F	(1033.79, -1007.50)	(1040.68, -1009.50)	7.18	61.61	6.65	72.07
	6G	(1034.59, -1003.52)	(1020.29, -1001.79)	14.40	56.03	14.41	71.30
	6H	(1035.09, -984.28)	(1017.32, -987.19)	18.00	58.48	17.11	75.13
LSL7	7A	(1015.19, -1027.82)	(1014.28, -1019.35)	8.52	85.50	5.69	68.00

Data Set ID	Crossing ID	Expected Crossing Coordinates [m]	Detected Crossing Coordinates [m]	Distance to Coastline [m]	UAV Height [m]	Angular Error [°]	Crossing Angle [°]
	7B	(1016.94, -1027.24)	(1014.00, -1025.44)	3.44	83.47	2.36	58.55
	7C	(1017.64, -1024.64)	(1004.64, -1023.82)	13.02	68.57	10.75	89.78
	7D	(1018.19, -1023.63)	(1010.97, -1022.86)	7.26	60.79	6.81	84.99
	7E	(1022.29, -1018.14)	(1016.23, -1014.53)	7.05	60.14	6.69	56.58
	7F	(1022.60, -1016.60)	(1025.67, -1018.86)	3.81	55.65	3.92	39.60

The results shown in Table 6-2 were processed using a minimum irradiance change threshold of $1 \times 10^{-5} \text{ Wm}^{-2}$ between the first and last irradiance values of a cubic polynomial fitted to every set of four consecutive spectra in a data set. A total of 36 coastline crossings were expected due to the geolocation of the spectrometer FOV and 36 coastlines crossings were detected using the inflection point method. Compared to Table 4-1, distances to the coastline crossings are reported in Table 6-2 along with angular error because height variations during the UAV flight can have a large effect on the angular error. Table 6-2 shows that the distances between the expected and detected coastline crossing coordinates varied from 0.27 m in the third flight over Chaffeys Locks to 25.25 m in the first flight over Little Skunk Lake. The mean distance between the expected and detected coastline crossings for the data sets was 9.16 m and the standard deviation was 6.38 m. The angular error to the coastline also shows a variation from a minimum of 0.26° to a maximum of 51.25° . The mean angular error was 10.87° and the standard deviation was 9.71° . The

largest angular error of 51.25° is a significant outlier in the data that occurs due to the low height of 11 m of the UAV at the time of the data acquisition of the spectral measurement corresponding to the detection of coastline 1C. Removing this outlier from the coastline detection results causes the mean angular error to reduce to 9.71° and the standard deviation to 6.78° .

The final column in Table 6-2, similar to that of Table 4-1, is the crossing angle at which the spectrometer crosses the coastline. While no relationship was observed between the angular error and the crossing angle in the spaceborne data analysis, a similar analysis was performed for the airborne data as shown in Figure 6-8.

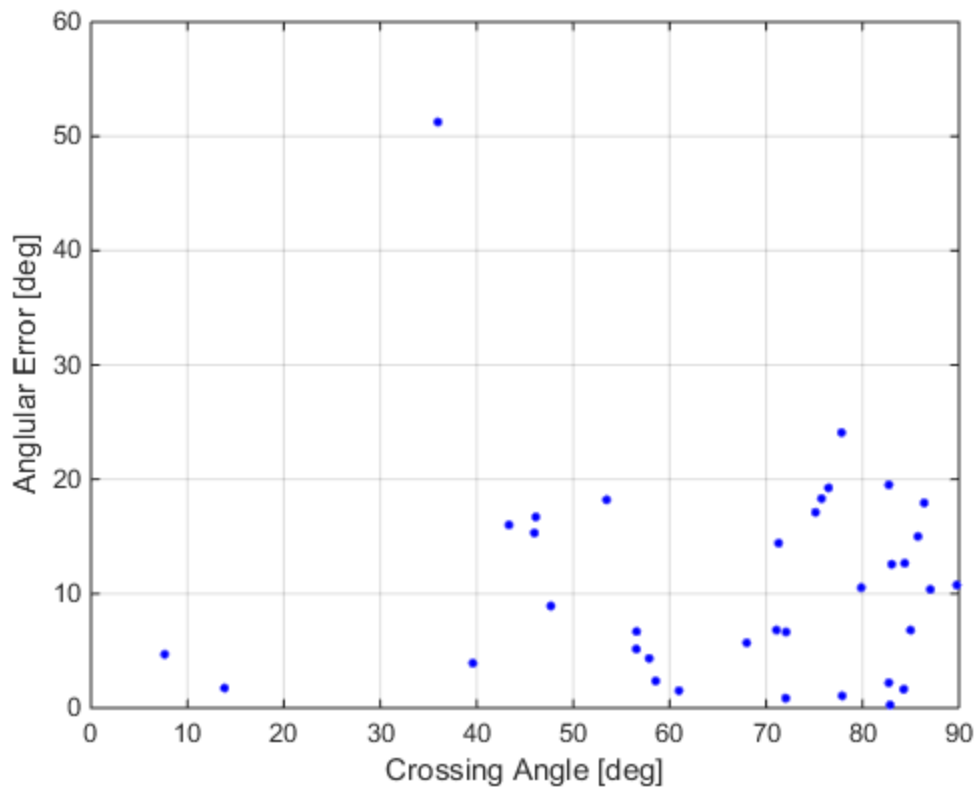


Figure 6-8 Angular error vs coastline crossing angle for FLAME-NIR airborne campaign coastline detection results

Just as in the space data analysis, Figure 6-8 shows that no relationship exists between the crossing angle of the spectrometer and the angular error to the coastline.

Since the observation period of the airborne validation campaign was two days, no significant trend in the angular errors to the coastline are expected. The angular error to the coastline over the duration of the airborne campaign is shown in Figure 6-9.

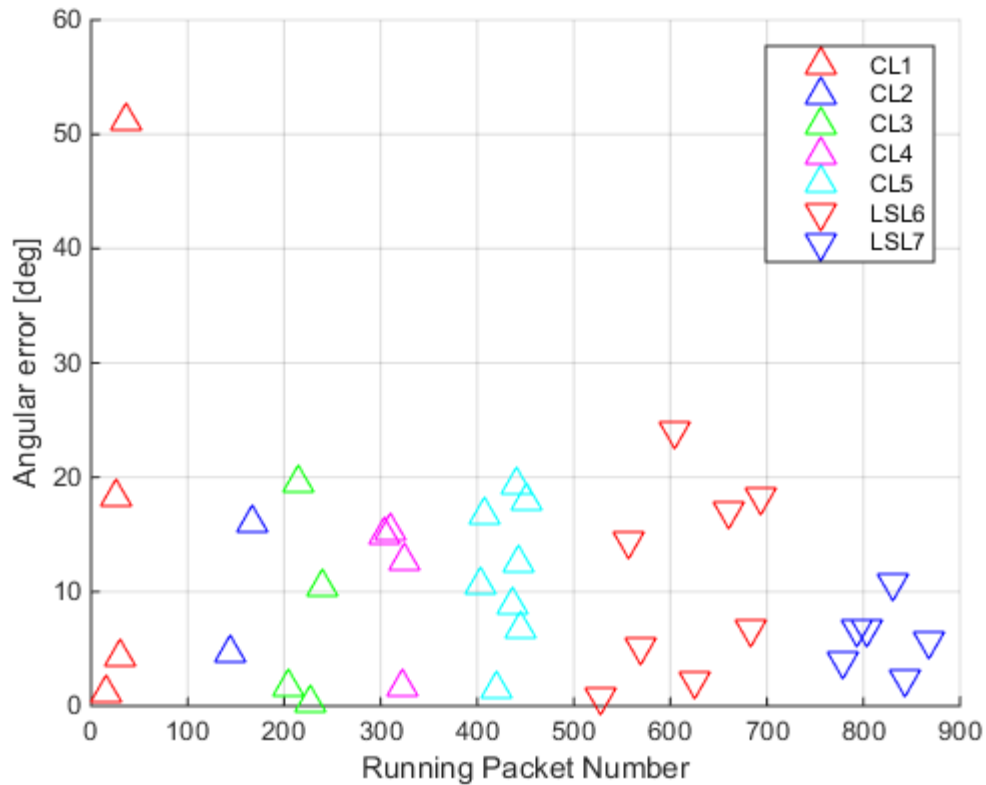


Figure 6-9 Angular error from expected coordinates to detected coordinates of coastlines versus packet number for Chaffeys Locks and Little Skunk Lake campaigns

The angular errors shown in Figure 6-9 are organized into one large data set, running from the first spectral measurement of the first flight, CL1, and ending at the last spectral measurement of the last flight, LSL7. Setup durations between data set acquisitions are omitted to prevent clustering of the results. As expected, no trend is observed in the computed angular error to the coastline over the duration of the airborne campaign.

Lastly, all the expected coastline crossings, detected coastline crossings, and the coastline polygons themselves are mapped onto the Chaffeys Locks and Little Skunk Lake orthomosaics for visualization, as shown in Figure 6-10.

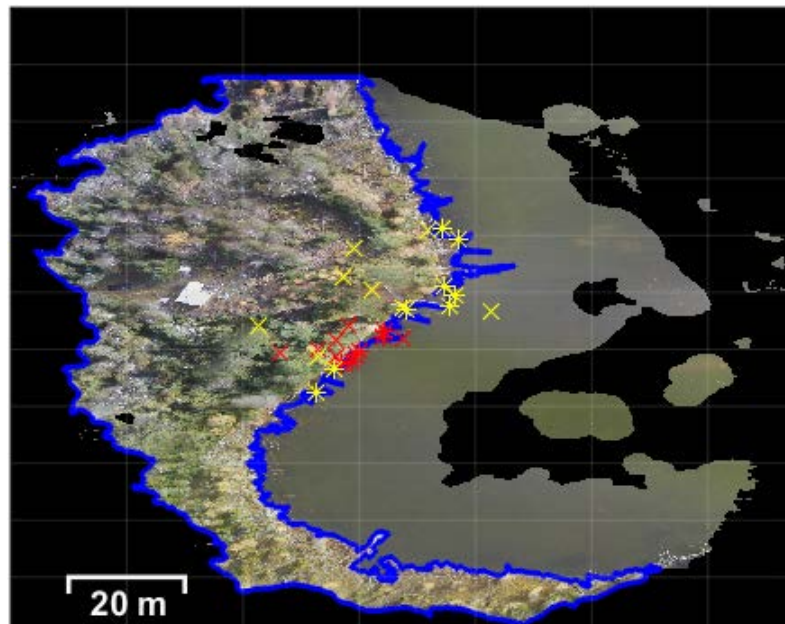
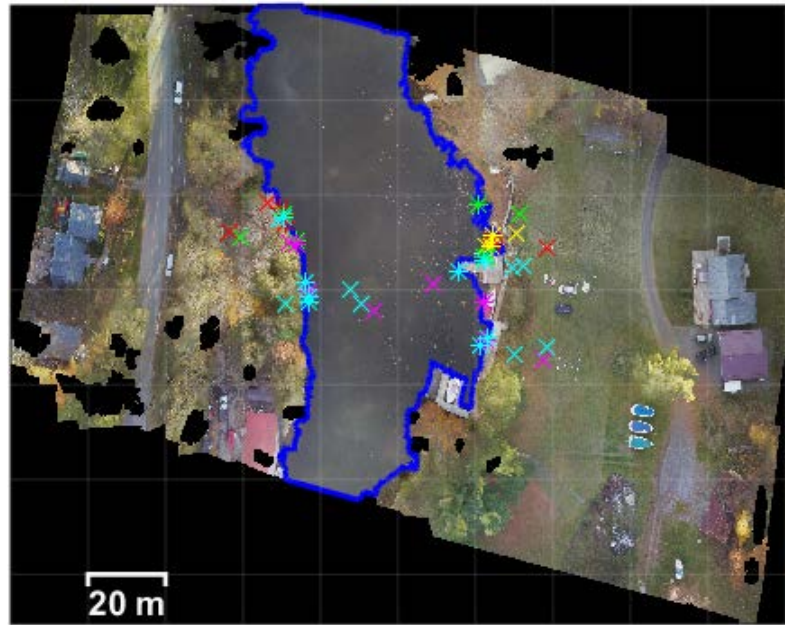


Figure 6-10 Orthomosaics of Chaffeys Locks (top) and Little Skunk Lake (bottom) with coastline polygons (blue), expected coastline locations (stars) and detected coastline locations (crosses) overlaid for each data set

The coastline detection results in Figure 6-10 are grouped by colour, with each colour indicating the coastline detections of a particular data set. Flights 1-5 over Chaffeys Locks are coloured in red, yellow, green, magenta, and cyan respectively, while flights 6 and 7 over Little Skunk Lake are coloured in yellow and red respectively. The results in Figure 6-10 show that most of the coastline detection locations are found over land, rather than water. This could be due to the low threshold value, which could cause variations in reflectance over different land surfaces to be mistaken for coastline detections more readily than the more uniform water surfaces.

In summary, from two independent airborne validation campaigns 7 data sets were successfully collected using the FLAME-NIR spectrometer. By applying the same coastline detection algorithm as for the spaceborne Argus 1000 data, 36 coastline crossings were detected and analyzed. Angular errors to the coastline were determined, as in the space data analysis, but were found to be greater in the airborne campaign due to the low height of the UAV as compared to the spacecraft. As in the spaceborne data, no significant relationship was observed between coastline error and crossing angle. The result from this analysis is consistent with that from the spaceborne data.

7 Conclusion and Recommendations for Future Work

Validation of geolocation accuracy of EO missions with low resolution spectrometers is a challenging problem. While various techniques are proposed for large space missions, limited techniques are available for CubeSat-class, resource constrained, low resolution spectrometer payloads. In this dissertation, a novel approach for automated geolocation accuracy assessment using coastline detection was developed and implemented. The algorithm was demonstrated using Argus 1000 NIR spectrometer data aboard the CanX-2 nanosatellite. The same algorithm was also applied to airborne data using the Ocean Optics FLAME-NIR spectrometer for validation purposes, with the results of both campaigns shown in Table 7-1.

Table 7-1 Summary of coastline detection results for spaceborne and airborne data

Data Set and Coastline Detection Metrics	Space Data	UAV Data
Number of Data Sets Analyzed	270	7
Data Sets with Coastline Detections	26	7
Number of Coastline Detection Candidates	128	36
Number of Detections Post Data Quality Check	55	35
Nominal Altitude	625 km	52.5 m
Mean Angular Error	0.44° +/- 0.5°	9.7° +/- 6.8°
Exposure Time	1.024 s	0.750 s
Equivalent Distance Error	5.0 km	9.0 m
Field of View	7.7 km	4.6 m

As shown in Table 7-1, the automated coastline detection algorithm was successfully applied to both the spaceborne spectrometer data and the airborne validation data. From the spaceborne data analysis, 270 data sets were analyzed, from which 55 coastlines were detected. The mean angular error in the data sets was 0.44° and the standard deviation was 0.57°, which was consistent with the CanX-2 mission requirements of 1°. Additionally, data integrity analysis was performed for the Argus 1000 data sets, with the percentage timing errors found to be 16.9% and 8.10% respectively using the RMSE and MAE methods. The airborne data analysis yielded similar results using the same coastline detection algorithm as the spaceborne data analysis. A total of 7 data sets were acquired over two days at two data collection sites. 36 coastline crossings were expected due to the

geolocation and 35 were detected. For the detected coastlines crossings, a mean angular error of 9.7° was observed, with a standard deviation of 6.8° . Compared to the spaceborne data, higher error was observed due to the lower speed and altitude of the UAV compared to the satellite. Nevertheless, the coastline detection method is proven to be a useful tool in assessing the geolocation accuracy in both space and airborne campaigns using a low resolution spectrometer such as Argus 1000 or the FLAME-NIR.

The key contributions of this research is the development of an automated approach for geolocation of CubeSat-class nanosatellite missions with low-resolution single-pixel spectrometers, which were demonstrated using spaceborne Argus 1000 NIR spectrometer data. Additionally, data quality metrics were developed and applied to the Argus 1000 data for future use in further analysis. A coastline detection algorithm for assessing geolocation accuracy was also developed and used on the Argus 1000 data, with a coastline search algorithm designed as a key step in the coastline detection process. Validation of the coastline detection method using an airborne campaign was proposed and demonstrated. Radiometric calibration was also performed for both Argus 1000 and FLAME-NIR spectrometers prior to airborne flights and spectral exposure per detector count conversion functions were developed for both instruments.

To further develop the geolocation algorithm, there are several areas that can be further explored. The results of the coastline detection algorithm could be used as an input for autonomous spacecraft mission operations. This would involve running the algorithm on

board a spacecraft in real time as part of post-launch calibration or at particular mission time periods as a means of validating geolocation and attitude knowledge accuracy.

Another area for further improvement of the geolocation algorithm is the use of known terrestrial features other than coastlines in the spectral data to conduct the geolocation accuracy assessment. The ability to distinguish different land surfaces within sections of the spectral window could be an additional source of data for assessing geolocation accuracy, provided some locations of such surfaces are well known or established using ground control points.

Additionally, a more detailed analysis of the effectiveness of the coastline detection algorithm could be achieved using simultaneous measurements from spaceborne and airborne instruments and cameras. This would provide additional spectral measurements to be used for screening out false detections.

Furthermore, the coastline detection analysis could be applied to other spectral windows outside the 900 nm to 1700 nm range, thereby providing a source of geolocation accuracy assessment for a greater range of EO instruments. The effect of clouds on the coastline detection analysis should also be studied in further detail in order to improve outlier detection criteria.

In the long run, more airborne validation data sets could be analyzed from a large range of areas and external conditions to provide greater understanding of the limitations of the algorithm and more generally, provide an understanding of the limitations of using an airborne campaign for space data validation.

Lastly, applying the algorithm to an EO mission with more stringent attitude knowledge and control requirements would also enhance understanding the validity of the algorithm, as would applying the algorithm to a series of other sensor types.

8 References

- [1] D. Selva and D. Krejci, "A survey and assessment of the capabilities of Cubesats for Earth observation," *Acta Astronautica*, vol. 74, pp. 50-68, May-June 2012.
- [2] Delft University of Technology, "DELFI-C3 Project," [Online]. Available: <http://www.delfispace.nl/delfi-c3>. [Accessed 21 April 2017].
- [3] B. Bruninga, "MARScom Satellite," 21 July 2008. [Online]. Available: <http://wa8lmf.net/bruninga/marscom.html>. [Accessed 24 April 2017].
- [4] G. Dirk, "RAFT1 (NO 60, Navy-OSCAR 60) / MARScom (NMARS)," 7 April 2017. [Online]. Available: http://space.skyrocket.de/doc_sdat/raft1_marscom.htm. [Accessed 24 April 2017].
- [5] C. R. Boshuizen, J. Mason, P. Klupar and S. Spanhake, "Results from the Planet Labs Flock Constellation," in *Proceedings of the AIAA/USU Conference on Small Satellites, Private Endeavors*, 2014.
- [6] Planet Labs, "Planet Labs Specifications: Spacecraft Operations & Ground Systems," June 2015. [Online]. Available: <http://www.rsgis.ait.ac.th/main/wp-content/uploads/Planet-Labs-Spacecraft-Ops.pdf>. [Accessed 2 May 2017].

- [7] National Aeronautics and Space Administration, "PharmaSat Nanosatellite Fact Sheet," [Online]. Available: https://www.nasa.gov/pdf/331108main_pharmasat_Fact%20Sheet_FINAL.pdf. [Accessed 2 May 2017].
- [8] M. Swartwout, "CubeSat Database," Saint Louis University, 17 April 2017. [Online]. Available: <https://sites.google.com/a/slu.edu/swartwout/home/cubesat-database>. [Accessed 1 May 2017].
- [9] M. Swartwout, "CubeSats and Mission Success: A Look at the Numbers," in *13th Annual CubeSat Developers Workshop*, San Luis Obispo, 2016.
- [10] H. C. Polat, J. Virgili-Llop and M. Romano, "Survey, Statistical Analysis and Classification of Launched CubeSat Missions with Emphasis on the Attitude Control Method," *Journal of Small Satellites*, vol. 5, no. 3, pp. 513-530, October 2016.
- [11] B. Doncaster, C. Williams and J. Shulman, "2017 Nano/Microsatellite Market Forecast," SpaceWorks Enterprises, Inc., 1 February 2017. [Online]. Available: http://spaceworksforecast.com/docs/SpaceWorks_Nano_Microsatellite_Market_Forecast_2017.pdf. [Accessed 2 May 2017].

- [12] A. Poghosyan and A. Golkar, "CubeSat evolution: Analyzing CubeSat capabilities for conducting science missions," *Progress in Aerospace Sciences*, vol. 88, pp. 59-83, January 2017.
- [13] E. Agasid, R. Burton, R. Carlino, G. Defouw, A. Dono Perez, A. Goktug Karacalioglu, B. Klamm, A. Rademacher, J. Schalkwyck, R. Shimmin, J. Tilles and S. Weston, "Small Spacecraft Technology State of the Art," Moffett Field, 2015.
- [14] J. P. Mason, T. N. Woods, A. Caspi, P. C. Chamberlin, C. Moore, A. Jones, R. Kohnert, X. Li, S. Palo and S. C. Solomon, "Miniature X-Ray Solar Spectrometer: A Science-Oriented, University 3U CubeSat," *Journal of Spacecraft and Rockets*, vol. 53, no. 2, pp. 328-339, 2016.
- [15] J. Bouwmeester and J. Guo, "Survey of worldwide pico- and nanosatellite missions, distributions and subsystem technology," *Acta Astronautica*, vol. 67, no. 7, pp. 854-862, 2010.
- [16] B. Smiley, "The absolute and relative geolocation accuracies of QB02 and WV01," in *Proceedings of the ASPRS Annual Conference*, Baltimore, 2009.
- [17] K. Sarda, S. Eagleson, E. Caillibot, C. Grant, D. Kekez, F. Pranajaya and R. E. Zee, "Canadian advanced nanospace experiment 2: Scientific and technological innovation on a three-kilogram satellite," *Acta Astronautica*, vol. 59, no. 1, pp. 236-245, June 2006.

- [18] R. Aked and E. Pylyser, "An Operational Concept for a Small Autonomous Satellite," in *Space Mission Operations and Ground Data Systems - SpaceOps '96, Proceedings of the Fourth International Symposium*, Munich, 1996.
- [19] A. S. Fukunaga, G. Rabideau, S. Chien and D. Yan, "ASPEN: A Framework for Automated Planning and Scheduling of Spacecraft Control and Operations," in *Proceedings of the International Symposium on AI, Robotics and Automation in Space*, Tokyo, 1997.
- [20] European Cooperation for Space Standardization, "Space engineering space segment operability ECSS-E-70-11A," European Space Agency, 2005.
- [21] L. M. G. Fonseca and M. H. M. Costa, "Automatic registration of satellite images," in *Proceedings of the X Brazilian Symposium on Computer Graphics and Image Processing*, 1997.
- [22] T. Kim and Y.-J. Im, "Automatic satellite image registration by combination of matching and random sample consensus," *IEEE Transactions on Geoscience and Remote Sensing*, vol. 41, no. 5, pp. 1111-1117, May 2003.
- [23] P. P. Singh and R. D. Garg, "Automatic road extraction from high resolution satellite image using adaptive global thresholding and morphological operations," *Journal of the Indian Society of Remote Sensing*, vol. 41, no. 3, pp. 631-640, September 2013.

- [24] I. Keramitsoglou, C. Cartalis and C. T. Kiranoudis, "Automatic identification of oil spills on satellite images," *Environmental Modelling and Software*, vol. 21, no. 5, pp. 640-652, May 2006.
- [25] A. K. Shackelford, C. H. Davis and X. Wang, "Automated 2-D building footprint extraction from high-resolution satellite multispectral imagery," in *IEEE International Geoscience and Remote Sensing Symposium*, 2004.
- [26] J. A. Leese, C. S. Novak and B. B. Clark, "An Automated Technique for Obtaining Cloud Motion from Geosynchronous Satellite Data Using Cross Correlation," *Journal of Applied Meteorology*, vol. 10, no. 1, pp. 118-132, 24 June 1970.
- [27] A. J. L. Harris, E. Pilger, L. P. Flynn, H. Garbeil, P. J. Mougini-Mark, J. Kauahikaua and C. Thornber, "Automated, high temporal resolution, thermal analysis of Kilauea volcano, Hawai'i, using GOES satellite data," *International Journal of Remote Sensing*, vol. 22, no. 6, pp. 945-967, 2001.
- [28] G. Benari, "Geolocation Algorithms for Nanosatellite Applications. M.Sc. Thesis," York University, Toronto, 2011.
- [29] L. H. Hoffman, W. L. Weaver and J. F. Kibler, "Calculation and Accuracy of ERBE Scanner Measurement Locations," 1987.

- [30] J. C. Currey, G. L. Smith and B. Neely, "Evaluation of Clouds and the Earth's Radiant Energy System (CERES) scanner pointing accuracy using a coastline detection system," in *Earth Observing Systems III*, 1998.
- [31] P. L. Spence, P. C. Hess and K. J. Priestley, "Geolocation validation of CERES measurements using radiance measurements," in *Earth Observing Systems VIII*, 2003.
- [32] C. J. Currey, "Geolocation Assessment Algorithm for CALIPSO Using Coastline Detection," 2002.
- [33] G. A. Poe and R. W. Conway, "A Study of the Geolocation Errors of the Special Sensor Microwave/Imager (SSM/I)," *IEEE Transactions on Geoscience and Remote Sensing*, vol. 28, no. 5, pp. 791-799, September 1990.
- [34] W. E. Purdy, P. W. Gaiser, G. A. Poe, E. A. Uliana, M. Thomas and F. J. Wentz, "Geolocation and Pointing Accuracy Analysis for the WindSat Sensor," *IEEE Transactions on Geoscience and Remote Sensing*, vol. 44, no. 3, pp. 496-505, March 2006.
- [35] G. A. Poe, E. A. Uliana, B. A. Gardiner, T. E. vonRenzell and D. B. Kunkee, "Geolocation Error Analysis of the Special Sensor Microwave Imager/Sounder," *IEEE Transactions on Geoscience and Remote Sensing*, vol. 46, no. 4, pp. 913-922, April 2008.

- [36] H. Wiebe, G. Heygster and L. Meyer-Lerbs, "Geolocation of AMSR-E Data," *IEEE Transactions on Geoscience and Remote Sensing*, vol. 46, no. 10, pp. 3098-3103, 19 September 2008.
- [37] M. Kroon, M. R. Dobber, R. Dirksen, J. P. Veefkind, G. H. J. van den Oord and P. F. Levelt, "Ozone Monitoring Instrument geolocation verification," *Journal of Geophysical Research: Atmospheres*, vol. 113, no. D15, 16 August 2008.
- [38] D. T. Gregoritch and H. H. Aumann, "Verification of AIRS Boresight Accuracy Using Coastline Detection," *IEEE Transactions on Geoscience and Remote Sensing*, vol. 41, no. 2, pp. 298-302, February 2003.
- [39] I. Moradi, H. Meng, R. R. Ferraro and S. Bilanow, "Correcting Geolocation Errors for Microwave Instruments Aboard NOAA Satellites," *IEEE Transactions on Geoscience and Remote Sensing*, vol. 51, no. 6, pp. 3625-3637, June 2013.
- [40] F. Tang, X. Zhu, H. Yang and F. Weng, "Estimation and Correction of Geolocation Errors in FengYun-3C Microwave Radiation Imager Data," *IEEE Transactions on Geoscience and Remote Sensing*, vol. 54, no. 1, pp. 407-420, January 2016.
- [41] C. S. May, "Engineering Evaluation of of Multi-Beam Satellite Antenna Boresight Pointing Using Land/Water Crossings," Orlando, 2012.

- [42] G. De Amici, J. Piepmeier and J. Peng, "Geolocation results of the SMAP passive instrument," in *2016 14th Specialist Meeting on Microwave Radiometry and Remote Sensing of the Environment (MicroRad)*, 2016.
- [43] Goddard Earth Sciences Data and Information Services Center, "Atmospheric Infrared Sounder (AIRS) Instrument Guide," National Aeronautics and Space Administration, 28 April 2003. [Online]. Available: http://disc.sci.gsfc.nasa.gov/AIRS/documentation/airs_instrument_guide.shtml. [Accessed 22 June 2016].
- [44] The Science Directorate at NASA's Langley Research Center, "The ERBE Scanner Instrument," National Aeronautics and Space Administration, 28 January 2014. [Online]. Available: <http://science.larc.nasa.gov/erbe/erbescanner.html>. [Accessed 22 June 2016].
- [45] J. P. Bobak, D. J. Dowgiallo, N. R. McGlothlin and T. E. vonRenzell, "Calibration and Validation Activities of the Airborne Polarimetric Microwave Imaging Radiometer," in *International Geoscience and Remote Sensing Symposium*, Anchorage, 2004.
- [46] W. Smith, A. Larar, J. Taylor, H. Revercomb, S. Kireev, D. Zhou, X. Liu, D. Tobin, S. Newman, P. Schluessel, A. Clough, S. Mango and K. St. Germain, "Joint

- Airborne IASI Validation Experiment (JAIVEx) - An Overview," in *Proceedings of the Sixteenth International TOVS Study Conference*, Angora dos Reis, 2008.
- [47] J. P. Hollinger, J. L. Peirce and G. A. Poe, "SSM/I Instrument Evaluation," *IEEE Transactions on Geoscience and Remote Sensing*, vol. 28, no. 5, pp. 781-790, September 1990.
- [48] M. Berger, J. Moreno, A. Muller, M. Schaepman, P. Wursteisen, M. Rast and E. Attema, "The Digital Airborne Imaging Spectrometer Experiment - DAISEX'99," in *International Geoscience and Remote Sensing Symposium*, Honolulu, 2000.
- [49] H. Saari, I. Pellikka, L. Pesonen, S. Tuominen, J. Heikkila, C. Holmlund, J. Makynen, K. Ojala and T. Antila, "Unmanned Aerial Vehicle (UAV) operated spectral camera system for forest and agriculture applications," in *SPIE Remote Sensing for Agriculture, Ecosystems, and Hydrology XIII*, 2011.
- [50] T. Hakala, E. Honkavaara, H. Saari, J. Makynen, J. Kaivosoja, L. Pesonen and I. Polonen, "Spectral imaging from UAVs under varying illumination conditions," in *Unmanned Aerial Vehicles in Geomatics (UAV-g)*, Rostock, 2013.
- [51] C. Clerbaux, M. George, S. Turquety, K. A. Walker, B. Barret, P. Bernath, C. Boone, T. Borsdorff, J. P. Cammas, V. Catoire, M. Coffey, P.-F. Coheur, M. Deeter, M. De Maziere, J. Drummond, P. Duchatelet, E. Dupuy, R. de Zafra, F. Eddounia, D. P. Edwards, L. Emmons, B. Funke, J. Gille, D. W. T. Griffith, J. Hannigan, F. Hase,

- M. Hopfner, N. Jones, A. Kagawa, Y. Kasai, I. Kramer, E. Le Flochmoen, L. J. Livesey, M. Lopez-Puertas, M. Luo, E. Mahieu, D. Murtagh, P. Nedelec, A. Pazmino, H. Pumphrey, P. Ricaud, C. P. Rinsland, C. Robert, M. Schneider, C. Senten, G. Stiller, A. Strandberg, K. Strong, R. Sussmann, V. Thouret, J. Urban and A. Wiacek, "CO measurements from the ACE-FTS satellite instrument: data analysis and validation using ground-based, airborne and spaceborne observations," *Atmospheric Chemistry and Physics*, vol. 8, no. 9, pp. 2569-2594, 2008.
- [52] M. J. McGill, M. A. Vaughan, C. R. Trepte, W. D. Hart, D. L. Hlavka, D. M. Winker and R. Kuehn, "Airborne validation of spatial properties measured by the CALIPSO lidar," *Journal of Geophysical Research: Atmospheres*, vol. 112, no. D20, 17 October 2007.
- [53] O. Reitebuch, C. Lemmerz, E. Nagel, U. Paffrath, Y. Durand, M. Endemann, F. Fabre and M. Chaloupy, "The Airborne Demonstrator for the Direct-Detection Doppler Wind Lidar ALADIN on ADM-Aeolus. Part I: Instrument Design and Comparison to Satellite Instrument," *Journal of Atmospheric and Oceanic Technology*, vol. 26, no. 12, pp. 2501-2515, 1 December 2009.
- [54] U. Marksteiner, O. Reitebuch, S. Rahm, I. Nikolaus, C. Lemmerz and B. Witschas, "Airborne Direct-Detection and coherent wind lidar measurements along the east coast of Greenland in 2009 supporting ESA's Aeolus mission," in *Proceedings of*

SPIE 8182, Lidar Technologies, Techniques, and Measurements for Atmospheric Remote Sensing VII, Prague, 2011.

- [55] RADARSAT International, "RADARSAT-1 Data Products Specifications," Richmond, 2004.
- [56] National Aeronautics and Space Administration, "Data Processing Levels," [Online]. Available: <https://science.nasa.gov/earth-science/earth-science-data/data-processing-levels-for-eosdis-data-products>. [Accessed 18 April 2017].
- [57] K. Riesing, "Orbit determination from two line element sets of ISS-deployed cubesats," in *29th Annual AIAA/USU Conference on Small Satellites*, Logan, UT, 2015.
- [58] J. R. Wertz, *Orbit & Constellation Design & Management*, 2nd ed., Hawthorne, California: Microcosm Press, 2009, pp. 251-254.
- [59] H. Chesser, R. Lee, G. Benari, R. Jagpal, K. Lam and B. Quine, "Geolocation of Argus Flight Data," *IEEE Transactions on Geoscience and Remote Sensing*, vol. 50, no. 2, pp. 357-361, 19 January 2012.
- [60] Thoth Technology Inc., "Argus 1000 IR Spectrometer Owner's Manual," October 2010. [Online]. Available:

http://www.thothx.com/manuals/Argus%20Owner's%20Manual,%20Thoth%20Technology,%20Oct%202010,%20rel%201_03.pdf. [Accessed 2 December 2015].

- [61] P. Wessel and W. H. F. Smith, "A global, self-consistent, heirarchical, high-resolution shoreline database," *Journal of Geophysical Research*, vol. 101, no. B4, pp. 8741-8743, 10 April 1996.
- [62] K. Hormann and A. Agathos, "The point in polygon problem for arbitrary polygons," *Computational Geometry*, vol. 20, no. 3, pp. 131-144, November 2001.
- [63] Ocean Optics, Inc., "FLAME-NIR Miniature Spectrometer User Manual," 2016. [Online]. Available: www.oceanoptics.com. [Accessed 8 September 2016].
- [64] G. C. Holst, *Testing and Evaluation of Infrared Imaging Systems*, 3rd ed., WinterPark, Florida: JCD Publishing, 2008.
- [65] Newport Corporation, "Report of Calibration of One Standard of Spectral Irradiance (250 - 2400 nm)," Irvine, 2015.
- [66] J. R. Taylor, *An Introduction to Error Analysis*, E. D. Commins, Ed., Mill Valley, California: University Science Books, 1982.
- [67] Edmund Optics, *Private Communications*, 2015.
- [68] Thoth Technologies, Inc., *Private Communications*, 2016.

- [69] Goodrich Sensors Unlimited, "LX-Series Linear Indium Gallium Arsenide Photodiode Arrays," 2006.
- [70] Google Earth Pro V 2.3.0.3830, "Chaffeys Locks, ON, 44° 34' 52.51"N, 76° 19' 4.92"W, Eye alt 757 m," 2015.
- [71] Google Earth Pro V 2.3.0.3830, "Little Skunk Lake, ON 44° 58' 32.22"N, 77° 56' 37.53"W, Eye alt 1.18 km," 2013.
- [72] E. M. Mikhail, J. S. Bethel and J. C. McGlone, Introduction to Modern Photogrammetry, New York, New York: John Wiley & Sons, Inc., 2001, pp. 234-235.

Appendix A Argus Timing Duration

Difference Experiment Data Tables

Below are the raw data tables for the analysis of the timing duration differences for spaceborne Argus 1000 data sets, discussed in Section 3.2. The flight spare model of the Argus 1000 spectrometer was used to acquire data at each exposure time setting for a duration of one minute. The total number of bytes acquired at each integration time setting and the total length of time for each set of measurements for a scan count setting of one is shown in A-1.

.

A-1 Size and duration of flight spare Argus data sets at varying exposure time settings for a scan count setting of 1

Exposure Time Setting (s)	Trial #1			Trial #2			Trial #3		
	Number of Start Bytes	Number of Stop Bytes	Stop Watch Time (s)	Number of Start Bytes	Number of Stop Bytes	Stop Watch Time (s)	Number of Start Bytes	Number of Stop Bytes	Stop Watch Time (s)
1.00E-04	18225	584855	59.87	12355	581915	60.2	581915	1151461	60.33
2.00E-04	6326	562964	60.06	1140089	1696829	59.84	1708970	2268549	60.09
4.00E-04	5924	536523	60.13	536523	1067317	60.03	1067317	1600444	60.27
8.00E-04	8313	514729	60.41	514729	1018471	60.02	1018471	1524831	60.08
1.60E-03	11703	459386	60.08	459386	909381	60.22	1381977	1829724	60.2
3.20E-03	5875	372422	60.09	372422	738969	60.2	738969	1105517	60.36
6.40E-03	2961	271382	60.08	271382	539509	60.22	539509	806550	60.13
1.28E-02	2846	177341	60.15	355248	528679	59.96	533999	707431	60.09
2.56E-02	2021	104697	60.23	211097	313773	60.09	313773	416449	60.16
5.12E-02	1064	56924	60.04	56924	112784	60.07	112784	168644	60.39
1.02E-01	1596	31388	60.12	31388	60648	59.98	60648	90440	60.01
2.05E-01	1596	16492	59.83	16492	31388	59.89	31388	46284	59.92
4.10E-01	1064	8512	60.22	8512	15960	60.23	15960	23940	59.99

The data acquired in A-1 was analyzed, along with the number of packets acquired during data acquisition to determine the average time per packet for each exposure time setting of the instrument. The calculated average packet times per exposure times, along with the number of packets for each trial are shown in A-2.

A-2 Comparison of the actual time per packet and the exposure time setting of flight spare Argus data sets for a scan count setting of 1

Exposure Time Setting (s)	Total Number of Bytes Sent			Number of Packets Present			Time per Packet (s)			Average Time per Packet (s)	Average Packet Time / Exposure Time
	Trial #1	Trial #2	Trial #3	Trial #1	Trial #2	Trial #3	Trial #1	Trial #2	Trial #3		
1.00E-04	566630	569560	569546	1065.09	1070.6	1070.58	0.06	0.06	0.06	0.06	562.65
2.00E-04	556638	556740	559579	1046.31	1046.5	1051.84	0.06	0.06	0.06	0.06	286.18
4.00E-04	530599	530794	533127	997.37	997.73	1002.12	0.06	0.06	0.06	0.06	150.5
8.00E-04	506416	503742	506360	951.91	946.88	951.8	0.06	0.06	0.06	0.06	79.15
1.60E-03	447683	449995	447747	841.51	845.86	841.63	0.07	0.07	0.07	0.07	44.61
3.20E-03	366547	366547	366548	689	689	689	0.09	0.09	0.09	0.09	27.31
6.40E-03	268421	268127	267041	504.55	504	501.96	0.12	0.12	0.12	0.12	18.66
1.28E-02	174495	173431	173432	328	326	326	0.18	0.18	0.18	0.18	14.37
2.56E-02	102676	102676	102676	193	193	193	0.31	0.31	0.31	0.31	12.18
5.12E-02	55860	55860	55860	105	105	105	0.57	0.57	0.58	0.57	11.19
1.02E-01	29792	29260	29792	56	55	56	1.07	1.09	1.07	1.08	10.53
2.05E-01	14896	14896	14896	28	28	28	2.14	2.14	2.14	2.14	10.44
4.10E-01	7448	7448	7980	14	14	15	4.3	4.3	4	4.2	10.26

The experiment was repeated for a scan count setting of two, with the raw data shown in A-3.

A-3 Size and duration of flight spare Argus data sets at varying exposure time settings for a scan count setting of 2

Exposure Time Setting	Trial #1			Trial #2			Trial #3		
	Number of Start Bytes	Number of Stop Bytes	Stop Watch Time (s)	Number of Start Bytes	Number of Stop Bytes	Stop Watch Time (s)	Number of Start Bytes	Number of Stop Bytes	Stop Watch Time (s)
1.00E-04	6416	291567	60.26	291567	574971	59.97	574971	857565	59.94
2.00E-04	3609	279046	59.19	296661	575429	59.88	575429	853740	60.06
4.00E-04	4255	269670	60.07	269670	534897	59.91	276527	541734	60.09
8.00E-04	5334	258695	60.16	258695	510329	60.07	510329	763560	60.14
1.60E-03	4256	228228	60.02	228228	451668	60.02	451668	675493	59.89
3.20E-03	4001	187009	60.02	187009	369788	59.95	558647	741122	60.08
6.40E-03	2127	135659	59.99	135659	269722	60.11	269722	403254	60.07
1.28E-02	2127	88311	59.95	88311	175027	60.16	175027	261743	60.09
2.56E-02	1596	52668	59.96	52668	103740	59.99	103740	154875	60.12
5.12E-02	1596	29791	60.01	59051	86715	59.96	86715	114379	59.95
1.02E-01	1064	15960	60.11	15960	30856	60.3	30856	45752	59.91
2.05E-01	4788	12236	60.09	12236	19684	60.03	19684	27132	60.12
4.10E-01	532	4787	60.06	4787	8511	60.13	8511	12767	60.05

Once again, the data acquired in A-3 was analyzed, along with the number of packets acquired during data acquisition to determine the average time per packet for each exposure time setting of the instrument. The calculated average packet times per exposure times, along with the number of packets for each trial are shown for a scant count setting of two in A-4.

A-4 Comparison of the actual time per packet and the exposure time setting of flight spare Argus data sets for a scan count setting of 2

Exposure Time Setting (s)	Total Number of Bytes Sent			Number of Packets Present			Time per Packet (s)			Average Time per Packet (s)	Average Packet Time / Exposure Time
	Trial #1	Trial #2	Trial #3	Trial #1	Trial #2	Trial #3	Trial #1	Trial #2	Trial #3		
1.00E-04	285151	283404	282594	536	532.71	531.19	0.11	0.11	0.11	0.11	1126.14
2.00E-04	275437	278768	278311	517.74	524	523.14	0.11	0.11	0.11	0.11	572.34
4.00E-04	265415	265227	265207	498.9	498.55	498.51	0.12	0.12	0.12	0.12	300.93
8.00E-04	253361	251634	253231	476.24	473	476	0.13	0.13	0.13	0.13	158.19
1.60E-03	223972	223440	223825	421	420	420.72	0.14	0.14	0.14	0.14	89.13
3.20E-03	183008	182779	182475	344	343.57	343	0.17	0.17	0.18	0.17	54.6
6.40E-03	133532	134063	133532	251	252	251	0.24	0.24	0.24	0.24	37.34
1.28E-02	86184	86716	86716	162	163	163	0.37	0.37	0.37	0.37	28.85
2.56E-02	51072	51072	51135	96	96	96.12	0.62	0.62	0.63	0.62	24.41
5.12E-02	28195	27664	27664	53	52	52	1.13	1.15	1.15	1.15	22.38
1.02E-01	14896	14896	14896	28	28	28	2.15	2.15	2.14	2.15	20.96
2.05E-01	7448	7448	7448	14	14	14	4.29	4.29	4.29	4.29	20.95
4.10E-01	4255	3724	4256	8	7	8	7.51	8.59	7.51	7.87	19.21

Appendix B Argus Timing Duration Difference Least Squares Fitting Table

Section 3.2 discusses an approach to analyzing the duration differences in spaceborne Argus data sets using least squares fitting for six cases. The cases were selected in order to determine whether any one of three settings was causing the timing issues in the data sets. The results of the least squares fitting to the data sets analyzed for timing accuracy is shown in B-1.

B-1 Least squares fitting of scaling factors to Argus data set exposure time and duration calculations

Case 1			Case 2			Case 3	Case 4	Case 5	Case 6
$\Delta t_{e,i}$ Calculation	Δt_p Calculation	LSQ Residuals	$\Delta t_{e,i}$ Coefficient	Δt_p Coefficient	LSQ Residuals	LSQ Residuals	LSQ Residuals	LSQ Residuals	LSQ Residuals
250.43	15.80	13.99	250.43	31.60	5.40	4.61	230.94	13.07	
15.79	196.10	8.11	15.79	197.40	110.47	312.20	-168.20	7.93	
15.79	196.10	8.11	15.79	197.40	110.47	312.20	-168.20	7.93	
307.39	31.20	0.09	307.39	62.40	-16.40	7.03	254.89	-1.03	
161.98	17.00	-4.83	161.98	34.00	-13.80	-0.30	128.90	-5.42	
299.20	30.40	1.94	299.20	60.80	-14.12	8.74	249.92	0.84	
141.31	6.90	11.12	141.31	13.80	7.29	2.69	135.51	10.61	
129.22	7.50	5.41	129.22	15.00	1.30	-0.45	117.98	4.94	
31.39	196.20	-8.52	31.39	392.40	-107.40	293.61	-170.46	-8.76	
315.58	16.60	16.29	315.58	33.20	7.14	-0.69	292.91	15.15	
315.58	16.60	10.29	315.58	33.20	1.14	-6.69	286.91	9.15	
307.38	16.10	17.69	307.38	32.20	8.80	1.04	287.18	16.57	
157.89	8.90	-21.38	157.89	17.80	-26.26	-28.95	116.43	-21.95	
313.54	16.50	14.35	313.54	33.00	5.25	-2.51	289.16	13.21	
131.39	5.20	6.98	131.39	10.40	4.03	-2.76	123.82	6.50	
319.68	9.00	21.36	319.68	18.00	16.02	-8.05	309.18	20.20	-0.30
320.70	31.80	-10.19	320.70	33.70	3.86	-4.13	256.37	-11.37	3.08
155.84	15.70	-35.10	155.84	17.60	-29.15	-31.77	94.19		-28.27
312.51	31.00	-8.34	312.51	32.90	5.30	-2.42	251.40	-9.49	4.61
139.46	14.10	-6.40	139.46	16.00	-1.26	-3.34	109.25	-6.91	-0.21
123.07	12.50	-3.70	123.07	14.40	0.64	-0.91	98.31	-4.15	1.85
314.69	32.00	-13.92	314.69	34.70	-0.58	-6.74	246.87	-15.08	0.33
313.54	31.10	-13.45	313.54	33.00	0.25	-7.51	247.15	-14.60	-0.45

120.00	12.20	-7.38	120.00	14.10	-3.19	-4.64	92.07	-7.82	-1.95
311.49	30.90	-8.24	311.49	32.80	5.36	-2.33	250.65	-9.38	4.68
319.68	31.70	-11.09	319.68	33.60	2.91	-5.05	254.63	-12.26	2.15
LSQ $\Delta t_{e,i}$ Coefficient			LSQ $\Delta t_{e,i}$ Coefficient			LSQ $\Delta t_{e,i}$ Coefficient		LSQ $\Delta t_{e,i}$ Coefficient	LSQ $\Delta t_{e,i}$ Coefficient
0.93			0.93			1.06		0.93	1.04
LSQ Δt_p Coefficient			LSQ Δt_p Coefficient				LSQ Δt_p Coefficient	LSQ Δt_p Coefficient	LSQ Δt_p Coefficient
1.56			1.03				2.54	1.56	0.02
LSQ Norm of Residual			LSQ Norm of Residual			LSQ Norm of Residual	LSQ Norm of Residual	LSQ Norm of Residual	LSQ Norm of Residual
2.58			7.57			20.48	41.98	2.28	2.67